UC Berkeley
UC Berkeley Electronic Theses and Dissertations

Title
Semiconductor Nanowires for Photoelectrochemical Water Splitting

Permalink
https://escholarship.org/uc/item/0xh2x55w

Author
HWANG, YUN JEONG

Publication Date
2012

Peer reviewed|Thesis/dissertation

eScholarship.org Powered by the California Digital Library
University of California

Semiconductor Nanowires for Photoelectrochemical Water Splitting

By

Yun Jeong Hwang

A dissertation submitted in partial satisfaction of the

requirements for the degree of

Doctor of Philosophy

in

Chemistry

in the

Graduate Division

of the

University of California, Berkeley

Committee in charge:

Professor Peidong Yang, Chair
Professor A. Paul Alivisatos
Professor Eugene E. Haller

Spring 2012

Semiconductor Nanowires for Photoelectrochemical Water Splitting

Copyright © 2012

by

Yun Jeong Hwang

Abstract

Semiconductor Nanowires for Photoelectrochemical Water Splitting

by

Yun Jeong Hwang

Doctor of Philosophy in Chemistry

University of California, Berkeley

Professor Peidong Yang, Chair

Photolysis of water with semiconductor materials has been investigated intensely as a clean and renewable energy resource by storing solar energy in chemical bonds such as hydrogen. One-dimensional (1D) nanostructures such as nanowires can provide several advantages for photoelectrochemical (PEC) water splitting due to their high surface areas and excellent charge transport and collection efficiency. This dissertation discusses various nanowire photoelectrodes for single or dual semiconductor systems, and their linked PEC cells for self-driven water splitting. After an introduction of solar water splitting in the first chapter, the second chapter demonstrates water oxidative activities of hydrothermally grown TiO_2 nanowire arrays depending on their length and surface properties. The photocurrents with TiO_2 nanowire arrays approach saturation due to their poor charge collection efficiency with longer nanowires despite increased photon absorption efficiency. Epitaxial grains of rutile atomic layer deposition (ALD) shell on TiO_2 nanowire increase the photocurrent density by 1.5 times due to improved charge collection efficiency especially in the short wavelength region. Chapter three compares the photocurrent density of the planar Si and Si nanowire arrays coated by anatase ALD TiO_2 thin film as a model system of a dual bandgap system. The electroless etched Si nanowire coated by ALD TiO_2 (Si EENW/TiO_2) shows 2.5 times higher photocurrent density due to lower reflectance and higher surface area. Also, this chapter illustrates that n-Si/n-TiO_2 heterojunction is a promising structure for the photoanode application of a dual semiconductor system, since it can enhance the photocurrent density compared to p-Si/n-TiO_2 junction with the assistance of bend banding at the interface. Chapter four demonstrates the charge separation and transport of photogenerated electrons and holes within a single asymmetric Si/TiO_2 nanowire. Kelvin probe force microscopy measurements show the higher surface potential on the n-TiO_2 (photoanode) side relative to the p-Si (photocathode) side under UV illumination as the result of hole accumulation on the TiO_2 side and electron accumulation on the Si side which are desirable charge separation for solar water splitting. In chapter five, TiO_2 is replaced with single phase InGaN nanowire in a dual bandgap photoanode to show

the potential for solar water splitting with high surface area Si/InGaN hierarchical nanowire arrays and InGaN as a possible candidate for visible light absorber. An enhancement of 5 times in photocurrent was observed when the surface area increased from InGaN nanowires on planar Si to InGaN nanowires on Si wires. Chapter six demonstrates a self-driven water splitting device with the p/n PEC cell which consists of a photocathode and a photoanode. The operating photocurrent (I_{op}) with the p/n PEC cell is enhanced when n-Si/p-Si photovoltage cell was embedded under an n-TiO_2 photoanode by utilizing the photovoltage generated by a Si PV cell. Also, the Si nanowire photocathode surface is modified with Pt and TiO_2 to increase hydrogen reducing activity and stability which enhances I_{op} of the p/n PEC cell as well. When Si/TiO_2 nanowire photocathode is linked with n-Si/p-Si photovoltage cell embedded TiO_2 nanowire photoanode, the p/n PEC cell shows water splitting without bias voltage confirmed with 2:1 ratio of hydrogen:oxygen gas evolution and a 92 % Faradic efficiency. These studies represent a significant step towards realizing the benefit of the advanced 1D nanowire configuration for efficient solar to energy conversion.

To my parents for their unbounded love and support,
to my sisters and brother for their sincere encouragement,
and to my husband for his devoted love.

Contents

Table of Contents

List of Figures

List of Tables

Acknowledgements

I cannot imagine making this achievement possible without the sincere help of countless people during my time at Berkeley. I would like to begin by appreciating all of their tremendous amounts of help.

I cannot write this page without expressing my deepest thanks to my academic advisor, Professor Peidong Yang, whose tireless enthusiasm, and scientific perspective, and inspiring drive for research guided me all the time. It has been great honor for me to have had the opportunity to work on a momentous and leading research field in an outstanding laboratory. There are much about his research attitudes that I would like to bring with me as I take the first step towards a scientist.

I am grateful for all the encouraging support and advice of Professor Paul Alivisatos, chairing my qualifying examination and serving as a member of my dissertation committee. I also thank Professor Eugene E. Haller for serving on both my qualifying examination committee and my dissertation committee, and thank Professor Garbor A. Somorjai and Professor Marcin Majda for serving my qualifying examination committee.

I must also thank my research group members, past and present. Erik Garnett gave invaluable guidance on research as my wonderful mentor from my first year at Berkeley, and Melissa Fardy, and Chris Hahn have been excellent colleagues who have provided kind assistance and helpful discussions while we had built water splitting measurement setup from the very first and grew challenging InGaN nanowires. Hoon Eui Jeong, Hung-Ta Wang, Elaine Lai Yang, Sarah Brittman, Cheng Hao Wu, Dan Gargas, Sean Andrews, Michael Moore, Chong Liu, Jongwoo Lim have been friendly, helpful, and intelligent group members, and I have spent great time with them. Allon Hochbaum, Akram Boukai, Alex Briseno, Lori Greene, Ben Yuhas, Harun Tueysuez, Sylvia HsiaoYun Lo, Jiaxing Huang, Woong Kim, Jinsub Park, Joe Park, Yusuke Yamada, Hyunjoo Lee, Heonjin Choi, Candace Chan, Frank Tsung, and Raul Diaz were also helpful.

This work was supported by Helios Solar Energy Research Center (SERC) program which provided great opportunities for me to network with graduate students and post doctoral fellows outside of my research group. It also provided valuable experiences that helped me improve my ability to present my researches and communicate science to other scientists.

In addition to the above, I want to thank my friends who stand by me and encourage me in happy and sad. Hyojin Kim, Hyerin Lee, Kanghoon Jeon, Eunsim Kwon, Hojai Lee,

Kyoohyun Noh, Franklin Kim, Christine Nam, Kihoon Kim, Yumi Um, Sanghoon Joo, and Mia Chang warmly helped me in times of need.

Finally, I would not be here today were it not for my family. I would like to thank my husband, Changhwan shin, for all of his love, and daily support. He is my light at the end of the dark and long tunnel, and I cannot imagine finishing my study at Berkeley without him. My parents (Rakhyun Hwang and Hyunsook Kim), my sisters, and brother support me with their unconditional love, and they are always a great comfort to me through all of hard time. Their love will hold a special place in my heart.

Chapter 1

Introduction: Solar Water Splitting

1.1 Hydrogen: Future Fuel

1.1.1 CO_2 Emission from Fossil Fuel

The supply of safe, clean, and renewable energy sources is one of the most challenging problems that we must solve due to environmental and political issues caused by energy crisis. In 2008, total worldwide energy consumption was 474×10^{18} J, which is an average energy consumption rate of 15 terawatt (TW).[1] Among various energy sources, 70% of the energy generation was obtained from fossil fuels such as coal, natural gas, and petroleum, while nuclear power occupied only 13%, and the rest of the energy generation came from renewable energy sources mostly from biomass. (Figure 1.1) CO_2 and other pollutant gases are emitted when fossil fuels are burning. Increasing concentration of those gases are considered to cause global warming and recent change of climate system.

According to Keeling curve,[2] CO_2 concentration are growing rapidly since 1960, and reaches 392 ppmv (part per million by volume) in 2011. Figure 1.2 shows that the atmospheric CO_2 levels over 400,000 years, and the Keeling curve is added to the right side showing dramatic increase of CO_2 levels.[3] The CO_2 concentrations maintained about 260-

280 ppmv over 10,000 years before the Industrial Revolution began showing that current high CO_2 levels are strongly related to the consumption of fossil fuels. Earth's average surface temperature has increased by about 0.8 °C since the early 20th century. The globally increased temperature can cause rising sea levels and expanding subtropical deserts. Nevertheless, the global energy consumption would increase and expect to be about 27 TW by 2050 due to population growth and economic growth in the world, particularly in China, India, and other developing countries.[4] Therefore, carbon-neutral energy sources as well as cost-effective mass-productive energy sources are required to be developed to satisfy global energy demand.

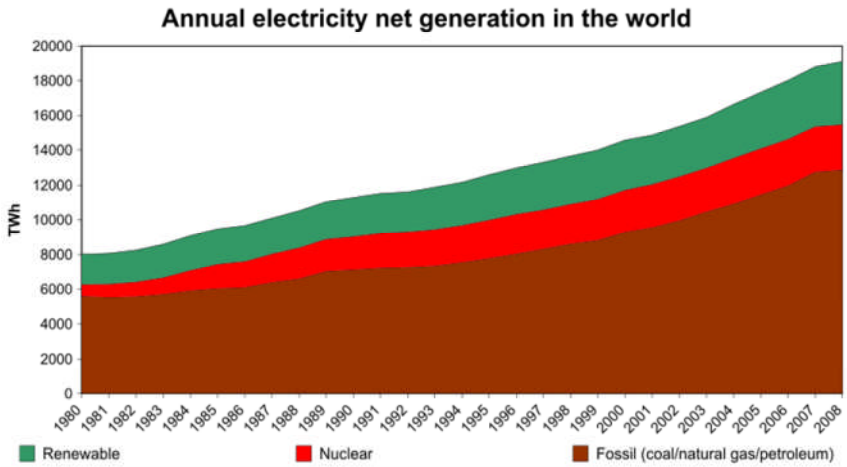

Figure 1.l. Annual electricity net generation in the world from 1980 to 2008.[5]

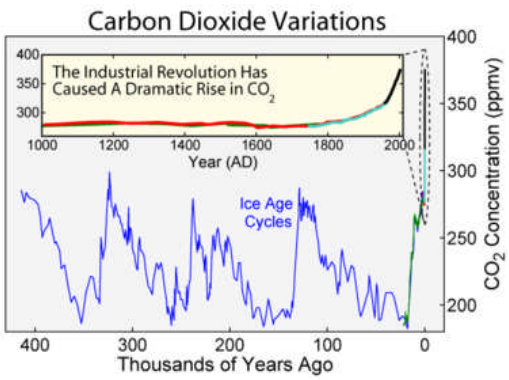

Figure 1.2. The atmospheric CO_2 concentration over the last 400,000 years.[3]

1.1.2 Hydrogen Economy

Hydrogen is suggested to overcome negative issues originated by using hydrocarbon fossil fuels since it can be an environmentally clean energy source. Hydrogen is expected to be used in transportation such as vehicles and in domestic heating applications since its combustion produces only water without release of pollutants or CO_2. These future applications of hydrogen expedite hydrogen production industry recently and need to develop a clean way of production. Globally, some 50 million tons of hydrogen were produced in 2004, with around 10% of the growth rate per year.[6]

Unfortunately, most of Hydrogen is present in a non-gaseous form in nature but is abundant in plants as well as in several chemical compounds such as methane, methanol, and higher hydrocarbons, and, most importantly, in water. Currently, 48 % of global hydrogen production is from natural gas, 30% from oil, and 18% from coal by using steaming reforming which causes CO_2 emission as a byproduct. Only 4% is produced by water electrolysis, although water can be an abundant and clean source of hydrogen if the electricity is generated by the environmentally clean pathway. To use hydrogen as a popular alternative energy resource in the future, both of its combustion and production should be CO_2 free and environmentally clean.

1.1.3 Photoelectrochemical (PEC) Hydrogen Production

Photolysis of water in a photoelectrochemical (PEC) cell by using sunlight is one of the clean ways to produce hydrogen since no polluting gases are emitted. In addition, among the various renewable energy sources such as wind, hydroelectric, tidal, and biomass, the sun has the potential to provide by far the largest amount of energy without the concern of shortage. The calculation shows that the amount of solar energy that arrives the earth only in 1 hr (4.3×10^{20} J/hr) [4] is comparable to the global energy consumption (4.74×10^{20} J/year in 2008) annually. Therefore, water splitting by using solar energy is a very promising approach to develop renewable energy resource.[8]

1.2 Semiconductor/Electrolyte Junction in PEC Cell

In 1972, Fujishima and Honda first reported photo-electrolysis of water with single crystalline n-TiO_2 in a PEC cell using light as the driving force.[9] In the PEC cell, semiconductor/electrolyte junction has a space charge layer on the semiconductor side adjacent to the interface with electrolyte, similarly to the semiconductor/metal junction.[10] This is because the concentrated electrolyte solution, which is used to minimize internal resistances in PEC cell, has ion concentrations in the order of $10^{21}/cm^3$ (in 1 M of

concentration)[11] comparable to electron concentrations in metal (10^{22} ~ 10^{23}/cm^3). When initial Fermi levels between two materials on the contact are different, a space charge region forms on the semiconductor side. Here, the Fermi level of liquid electrolyte is defined by the redox potentials of the chemical species in the electrolyte. If the initial Fermi level in an n-type semiconductor is above that in the electrolyte, electrons transfer from the semiconductor to the electrolyte to equalize the Fermi levels (or chemical potentials). As a result of the equilibration, electrons (majority carriers) are depleted in n-type semiconductor surface forming a positive space charge region (or depletion region). The electrical potential originated by the positive charges causes band bending downward on the semiconductor surface such that electron cannot transfer to the electrolyte further. (Figure 1.3) The analogous but the opposite charge transfers occur at p-type semiconductor/electrolyte interface when the initial Fermi level of p-type semiconductor is below that of the electrolyte. Holes (majority carriers) move from p-type semiconductor into the electrolyte, and a negative space charge region is formed in the semiconductor side with band bending upward due to a negative potential.

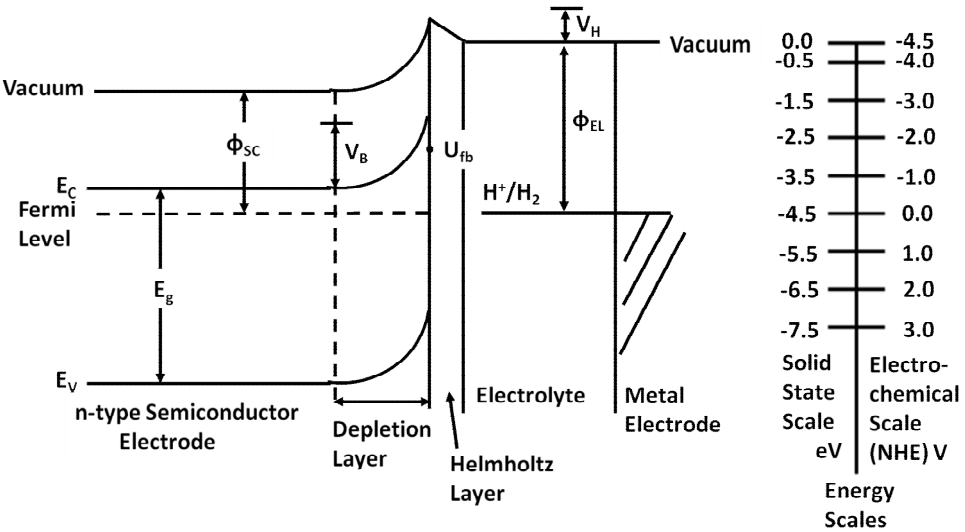

Figure 1.3. Energy level diagram for n-type semiconductor/electrolyte junction showing the relationships between the electrolyte redox couple (H^+/H_2), the Helmholtz layer potential drop (V_H), work function (φ_{sc}), and flat-band potential (U_{fb}).

The space charge region (W) is defined as the equation below.[12]

$$W = \sqrt{\frac{2\varepsilon_r^{'}\varepsilon_0\psi_{bi}}{qN}}$$

Equation 1.1

where ψ_{bi} is a built-in potential at the interface, N is a charge carrier density in semiconductor, $\varepsilon_r^{'}$ is the dielectric constant of the semiconductor, ε_0 is the permittivity of

free space, and q is the charge of electron. In typical cases, W varies from 100 Å to several μm in semiconductor surface.

Meanwhile, Helmholtz double layer is formed on the electrolyte side adjacent at the interface. The charged ions from the electrolyte are adsorbed on the semiconductor surface, whose charges are the opposite sign to the charge in the space charge region of the semiconductor. [11] For the abovementioned case, the positive charge are accumulated in the space charge region (or depletion region) of the n-type semiconductor, and negatively charged ions are absorbed on the semiconductor surface which attracts positively charged ions in the next layer forming double layer on the electrolyte side. Due to the high ionic concentration in the electrolyte, Helmholtz layer is only a few Å,[10] and V_H (Helmholtz layer potential drop) is constant with external bias potential due to the much higher capacity of the Helmholtz layer compared to depletion region capacity in the semiconductor. Then, all of the external bias potential appears across the depletion region in the semiconductor. Therefore, the band edge potentials of the semiconductor at the surface are fixed with respect to the Fermi level of the electrolyte, and constant despite the external bias potentials. Without the Helmholtz layer, the band bending can simply be determined by the difference in initial Fermi levels but V_H affects the band bending. This is similar to the fact that the potential barrier and band bending at semiconductor/metal Schottky barrier are affected by the surface states.

When the PEC cell consists of an n-type semiconductor photoanode and a metallic cathode,[13-15] the band energy diagram of both electrodes are shown in Figure 1.4. Figure 1.4a shows the initial energy diagram in open circuit (without contact) before the equilibrium. When two electrodes are connected in dark, the charge transfer happens between n-type semiconductor and electrolyte resulting band bending on the semiconductor side. (Figure 1.4b) Water splitting does not proceed thermodynamically without light since the Fermi level of the metal cathode is lower than hydrogen reduction potential (H^+/H_2), and the Fermi level of the semiconductor is higher than water oxidation potential (O_2/H_2O). Figure 1.4c illustrates the band energy diagram under illumination showing the bend banding and Fermi level of the semiconductor change due to the photovoltage (V_{ph}) gain. According to Gärtner's model, photogenerated electron-hole pairs by the semiconductor can separate due to the electric field (drift current) in the depletion region, and the electron-hole pairs generated beyond the depletion region can also separate if the minority carriers (holes in n-semiconductor) can diffuse to the depletion region before recombination (diffusion current). The charge separation of the electron-hole pairs in the depletion region reduces the band bending in the semiconductor which shifts the Fermi level of the semiconductor toward its U_{FB} (flat-band potential) as shown in Figure 1.4c and Figure 1.5.[16] The difference of the Fermi levels in the semiconductor between under illumination and in dark is equal to V_{ph} at semiconductor/electrolyte junction.

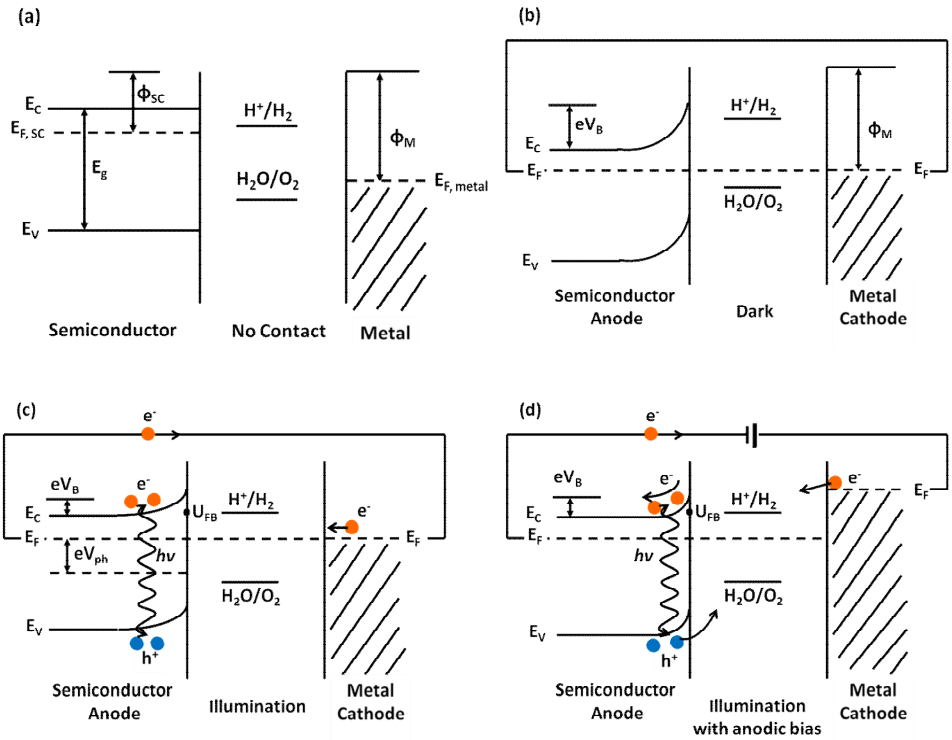

Figure 1.4. Energy diagram of PEC component.: (a) in open circuit (no contact), (b) after contact in dark, (c) under illumination showing the effect of light, and (d) under illumination with external bias potential.

In the steady state of illumination, the local concentration of electrons and holes differs from the equilibrium in dark by Δn and Δp respectively, and the quasi Fermi level (E_F^*) is defined as follows.[11]

$$_nE_F^* = E_F + kT\ln(1+\Delta n/n_0) \qquad \text{Equation 1.2}$$

$$_pE_F^* = E_F - kT\ln(1+\Delta p/p_0) \qquad \text{Equation 1.3}$$

The equation 1.2 and 1.3 show that only the quasi-Fermi level of the minority carrier can deviate from E_F because of relative concentration change ($\Delta n/n_0$ or $\Delta p/p_0$). The difference between the quasi-Fermi levels of the majority carrier and that of the minority carrier provides the driving forces of the PEC cell. The electrons (majority carriers in the n-semiconductor) move toward the semiconductor bulk, and then, the external circuit. Meanwhile, the holes (minority carriers in the n-semiconductor) move toward the semiconductor surface where oxidation reaction occurs through hole transfers to the electrolyte if the quasi-Fermi level of holes ($_pE_F^*$) is lower than oxidation potential. In the

case of Figure 1.4c, although ${}_pE_F^*$ is lower than water oxidation potential, the overall water splitting does not proceed since the Fermi level of electrons is still lower than hydrogen reduction potential which prevents electron transfers to the electrolyte on the counter metal electrode.

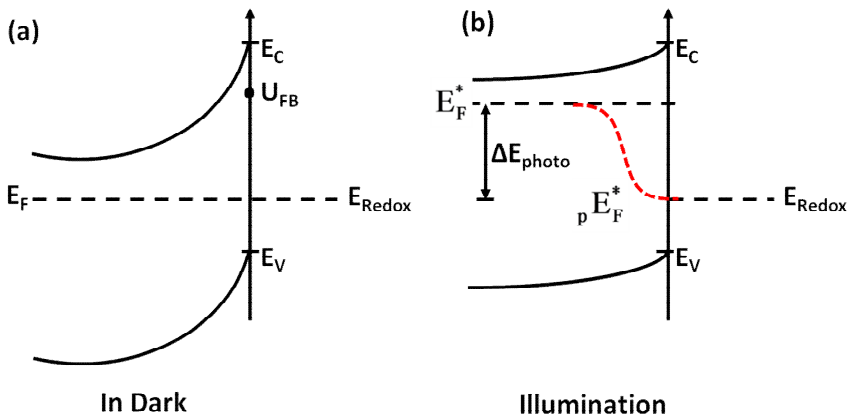

Figure 1.5. Energy diagram of semiconductor/electrolyte junction (a) in dark and (b) under illumination showing the qausi-Fermi levels and photovoltage.

When an anodic external bias potential is applied under illumination to elevate the Fermi level of electrons above hydrogen reduction potential, the PEC cell can finally accomplish water splitting on both of the photoanode and the cathode as shown in Figure 1.4d.

1.3 Semiconductor Material Requirements

1.3.1 Band Gaps of Semiconductors

The critical component of the PEC cell for solar water splitting is the semiconducting photoelectrode. To realize this technology commercially with greater than ~ 10% solar to hydrogen (STH) conversion efficiency, the semiconductor materials must satisfy several property requirements including electrical, optical, and chemical properties.[8,13,17]

First of all, the band gap (E_g) is one of the most important factors because the semiconductor can only absorb the photons that have greater energies than its E_g. Smaller E_g is expected to be more favorable considering absorption of the solar spectrum. However,

1.23 eV is a theoretical lower limit of E_g which is the equilibrium potential difference between the hydrogen reduction potential (H^+/H_2) and the water oxidation potential (O_2/H_2O). The lower limits of E_g get larger in the range of 1.6 ~ 1.9 eV if we consider the overpotentials (or activation energys) for both reactions along with the energy losses in the semiconductor.[18] On the other hand, for the 10% energy conversion efficiency, E_g should be smaller than about 2.3 eV [19] even assuming 100% quantum efficiency. (Figure 1.6)

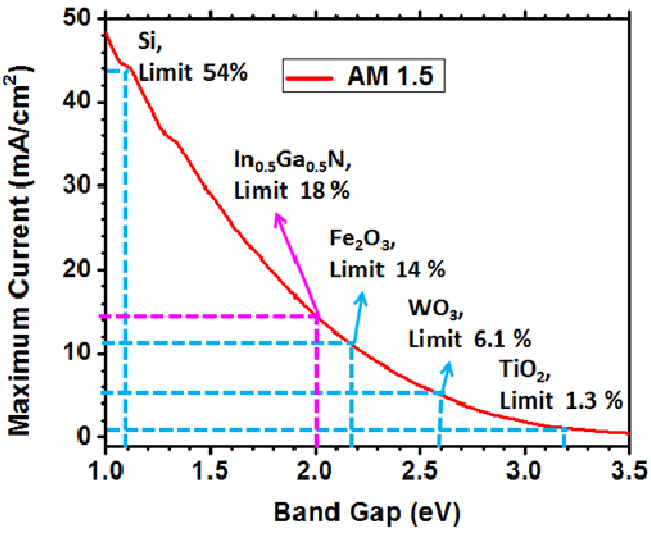

Figure 1.6. Calculated photocurrent density as a function of band gap with 100% of quantum efficiency. Solar irradiance used for the calculation is taken from AM 1.5 G data. Some of representative photoelectrode materials are indicated in the graph.

1.3.2 Bandedge Potentials

Second, the bandedge potentials of the semiconductor should sandwich the hydrogen reduction potential and water oxidation potential. In other words, for the n-type semiconductor, valence band maximum (VBM) should lower than the O_2/H_2O level, and the Fermi level should be higher than the H^+/H_2 level. As mentioned above (Figure 1.4), if the Fermi level of n-type semiconductor is lower than the H^+/H_2 level, an anodic external bias potential is required fulfill the water splitting which decrease the efficiency of PEC cell. For the p-type semiconductor, the analogous requirements should be satisfied: the Fermi level should be lower than the O_2/H_2O level, and conduction band minimum (CBM) should be higher than the H^+/H_2 level.

1.3.3 Stability of Materials

Third not least, the semiconductor should be stable in an aqueous solution during PEC water splitting reaction. Photodecomposition of the semiconductor material is one of the critical problems to realize the PEC cell device.[11, 20] To use the PEC cell commercially, the semiconductor wants to be stable for ~ 10 year according to U. S. Department of Energy (DOE) report.[21] In general, the holes of the valence band are involved in the oxidative decomposition of the semiconductor, while electrons of conduction band are involved in the reductive decomposition of the semiconductor under illumination. In the thermodynamic point of view, the semiconductor is expected to be stable if the decomposition reaction potentials are located outside the band gap of the semiconductor. [20] However, if one or both are positioned inside the gap, the semiconductor is unstable for decomposition, and its activity will degrade over time. Due to their stability, metal oxide materials such as TiO_2 (3.0~3.2 eV) has been studied intensely for the photoanode application.[22] Although some semiconductors such as CdS (2.4 eV),[23] and Cu_2O (2.1 eV) [24] have smaller E_g than TiO_2 with desirable bandedges levels for water splitting, their photodecomposition is serious obstacle for PEC application. Coating with a protective layer or using sacrifice regents has been applied to overcome their decomposition issues, but more researches are required to use those unstable materials for water splitting PEC devices.

Fourthly, for commercial viability, we want to develop semiconductor materials that are inexpensive, abundant, and non-toxic since this technology will be used for renewable energy sources.

1.3.4 Future Materials

To date, no such single semiconductor material has been discovered that satisfied all these requirements, although various semiconductor candidates have been investigated.[13, 25-27] The most stable and popular semiconductors for the PEC applications are oxide semiconductors, but they have several drawbacks. Their E_g are either too large to absorb the solar spectrum efficiently (ex TiO_2, $SrTiO_3$, $KNbO_3$) their bandedges do not match with the hydrogen reduction potential and water oxidation potential for the spontaneous reaction (ex WO_3, Fe_2O_3), or their electrical properties are too poor to have high internal quantum efficiency (ex Fe_2O_3). The application of metal oxides in the visible light region has been demonstrated but has not been successful due to the deep VBM position affected by O 2 p orbitals potential.[28] The low VBM position results that the CBM is located lower than hydrogen reduction potential when E_g is reduced to a visible light absorber. In the point of VBM potential, III-V semiconductors including metal nitrides[28-29] and phosphide are promising candidate. Especially, the VBM of nitride semiconductors are located higher than that of oxides since it is mainly determined by N 2P orbitals potential.

Since we want to use solar energy to store it in chemical bond, the material has to be a good absorber of sunlight at the first step. We can simply characterize E_g of the semiconductors by using a UV-Vis spectrometer. If the E_g of the semiconductors falls in the desirable range (1.5 eV < E_g < 2.5 eV), we can start to investigate PEC properties

including characterization of the bandedge potentials. Ultraviolet photoelectron spectroscopy (UPS) or Mott-Schottky measurement can be applied to know the bandedge potentials relative to the vacuum level or normal hydrogen reduction electrode (NHE). From Mott-Schottky measurement, we can also characterize the doping type (n-type or p-type) and carrier concentration as well as U_{FB}.[31] At the next step, cyclic-voltammetry (CV) measurement can measure the photocurrent density depending on the bias potential, and the obtained saturated photocurrent density will tell us the upper limit the rate of hydrogen production. If the rate of hydrogen production is high enough to achieve ideal STH efficiency, we can investigate the material properties further to understand how well the semiconductor can convert photons to electrons and how we can improve the quantum efficiency more. The incident photon to conversion efficiency (IPCE, will be discussed later in this chapter) measurement will provide the idea of material's external quantum efficiency and its internal quantum efficiency can be characterized by considering its absorption properties. We also need to measure the real hydrogen evolution speed with gas detection such as gas chromatography, and if the Faradic efficiency is close to 100%, the material would be tested for stability during PEC reaction.

1.4 Efficiency of PEC Cell

Definitions characterizing material properties or determining water splitting efficiency must be consistent in the solar to fuel conversion research field to compare various reported materials and to develop this technology in the more efficient fashion. Among various type of efficiency, photo-conversion efficiency is the most important figure of merit for the PEC water splitting, and the generally accepted benchmark efficiency is 10 % for a commercial implementation. We will discuss the four primary definitions of the water splitting efficiencies according to the U. S. Department of Energy (DOE) Energy Efficiency and Renewable Energy.[32] They are solar-to-hydrogen conversion efficiency (STH), applied bias photon-to-current efficiency (ABPE), incident photon-to-current efficiency (IPCE), and absorbed photon-to-current efficiency (APCE).

1.4.1 Solar-to-Chemical Conversion Efficiency: STH and ABPE Efficiency

Solar-to-chemical conversion efficiency is defined as the ratio of the chemical energy stored in the form of chemicals such as hydrogen molecules to the incident photon energy. For the PEC water splitting cell, the solar-to-chemical conversion efficiency is defined below (equation 1.4),[33] assuming 100% Faradic efficiency (η_F).

$$\eta = \frac{J_{ph}(mA/cm^2) \times (1.23 - V_{app})(V)}{P_{in}(mW/cm^2)} \qquad \text{Equation 1.4}$$

Where P_{in} is the power density of incident photon illumination, J_{ph} is the measured photocurrent density, 1.23 V (E^o) is the Gibbs free energy change (ΔG) per photon required to split water at standard condition, 25 ^oC, and V_{app} is the applied bias voltage measured between the working and counter electrodes in a two-electrode system. It is important to emphasize that the applied voltage is between the working and counter electrodes (in the two-electrode system) not between the working and reference electrodes (in the three-electrode system) since many reports often have used the latter value without correction. The real electrical power loss is the product of the photocurrent and voltage applied between the working and the counter electrode. If the applied voltage is used between the working and the reference electrode, the cell efficiency ends up calculating overestimated value. To make the equation 1.4 valid, both the working and the counter electrodes must be immersed in the same pH electrolyte in order to prevent a chemical potential between two electrolytes from Nernst bias of 59 mV/pH. In addition, the electrolyte should not have any sacrificial reagents because those redox potentials differ from the original water splitting potentials. [34]

Now, a STH efficiency can be calculated when the device is illuminated with solar Air Mass 1.5 Global (AM 1.5 G) spectrum under zero bias potential condition (V_{app} = 0 V) for the benchmarking report. [30]

$$STH = [\frac{J_{ph}(mA/cm^2) \times 1.23(V) \times \eta_F}{P_{in}(mW/cm^2)}]_{AM1.5G} \qquad \text{Equation 1.5}$$

If H_2 production rate is directly measured by the gas detection technique such as gas chromatography or mass spectrometry, the equation 1.5 can be modified to the equation 1.6 to calculate STH. Here, the Gibbs free energy per mole of H_2 is ΔG =237 kJ/mol.

$$STH = [\frac{mmol\ H_2/s \times 237 kJ/mol}{P_{in}(mW/cm^2) \times area(cm^2)}]_{AM1.5G} \qquad \text{Equation 1.6}$$

Applying a bias between the working and the counter electrodes can provide more information to understand the PEC performances of the semiconductors. The photocurrent density can increase under the applied bias voltage, and the saturated photocurrent density can be achieved with the external bias voltage depending on the materials. This is because the width of the space charge region in the semiconductor varies depending on the bias

potential which can affect the contribution of drift current and diffusion current to the total net photocurrent from the semiconductor electrode. The ABPE is defined as below.

$$ABPE = [\frac{J_{ph}(mA/cm^2) \times (1.23 - V_{app})(V)}{P_{in}(mW/cm^2)}]_{AM1.5G} \qquad \text{Equation 1.7}$$

1.4.2 Incident Photon-to-Current Efficiency (IPCE)

The IPCE is one of the most important diagnostic figures of merit for the PEC cell, and it also represents the external quantum efficiency (EQE) of the cell. IPCE is generally measured as a function of wavelength, λ (nm), under monochromatic light whose intensity is carefully measured with a calibrated photometer. The photocurrent is usually obtained from a chronoamperometry (potentiostatic) measurement, and an external bias potential can be applied during IPCE measurement. IPCE (or EQE) is defined as shown in equation 1.7. The integration of the IPCE values over the AM 1.5G solar spectrum can provide the estimated maximum STH efficiency when they are measured under zero bias potential between the working and the counter electrodes.

$$\begin{aligned} IPCE(\lambda) = EQE(\lambda) &= \eta_{e^-/h^+}\eta_{transport}\eta_{interface} \\ &= \frac{electrons(cm^2/s)}{photons(cm^2/s)} = \frac{J_{ph}(mA/cm^2) \times 1239.8(V \times nm)}{P_{mono}(mW/cm^2) \times \lambda(nm)} \end{aligned} \qquad \text{Equation 1.7}$$

Where $1239.8(V \times nm)$ represents a multiplication of $\hbar$ (Planck constant), and c (speed of light), and P_{mono} is the calibrated power intensity of monochromated light.

IPCE (or EQE) is also useful to understand PEC properties of the material since three fundamental PEC processes are involved. Figure 1.7 shows those processes which are photon absorptance (η_{e^-/h^+}), charge transport inside of the semiconductor to the semiconductor/electrolyte interface ($\eta_{transport}$), and interfacial charge transfer across the semiconductor/electrolyte ($\eta_{interface}$). η_{e^-/h^+} is defined as the ratio of photogenerated electron-hole pairs per incident photon flux, [30, 35] and it is strongly dependent on the absorption coefficient (α) and the thickness of the materials. The latter two processes ($\eta_{transport}$ and $\eta_{interface}$) are associated with the internal quantum efficiency (IQE) of the materials. Various material properties such as doping density, charge carrier mobility, minority carrier's diffusion length, surface states density, surface recombination velocities, etc. can affect them.

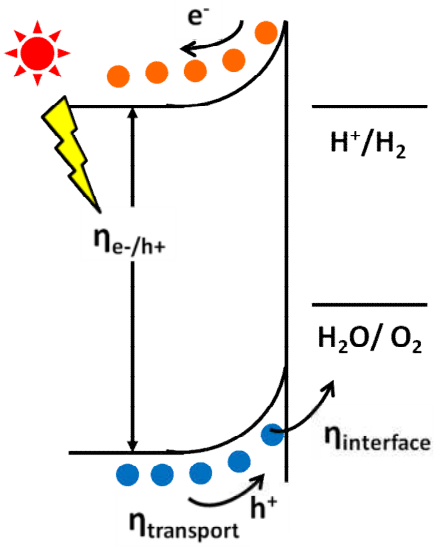

Figure 1.7. Band diagram of a photoelectrochemical water splitting cell illustrates three processes of photon absorption (electron-hole excitation), charge transport, and interfacial reactions.

1.4.3 Absorbed Photon-to-Current Efficiency (APCE)

To understand the inherent performances of the semiconductor materials, APCE is helpful since reflection or transmission of incident photons can be eliminated. APCE (or IQE) indicates the collected electrons per incident photon indeed absorbed by the semiconductor. This value is particularly useful when the sample electrode is too thin to absorb most of the incident photons since it can determine the balanced thickness between absorption versus effective charge transport within the material for the optimal photocurrent output.

Absorptance is estimated from Beer's Law.

$$\eta_{e^-/h^+} = \frac{I_o - I}{I_o} = 1 - \frac{I}{I_o} = 1 - 10^{-A},$$
$$A = -\log(\frac{I}{I_o})$$

Equation 1.8

$$APCE(\lambda) = IQE(\lambda) = \frac{IPCE(\lambda)}{\eta_{e^-/h^+}} = \eta_{transport}\eta_{interface}$$
$$= \frac{J_{ph}(mA/cm^2)\times 1239.8(V\times nm)}{P_{mono}(mW/cm^2)\times\lambda(nm)\times(1-10^{-A})} \qquad \text{Equation 1.9}$$

We can decouple $\eta_{transport}$ and $\eta_{interface}$ factors further from APCE values. Ideally, $\eta_{transport}$ is not strongly dependent on the types of redox couples, while $\eta_{interface}$ is affected by them.[30] Therefore, if an appropriate sacrificial redox couple is selected, $\eta_{interface}$ can be effectively 100%.

Among four main efficiencies that are discussed in this chapter, STH is the most critical value for benchmarking to compare different PEC candidate materials, and requires to be measured accurately. The other efficiencies such as ABPE, IPCE, and APCE, are important to understand material properties and improve their water splitting performances.

1.5 One-Demensional Nanostructures for PEC cell

Earlier works in the PEC water splitting have been focused on bulk or planar semiconductor materials, but the efficiency of those PEC devices still have room for improvement. Recently, nanostructured materials have been investigated a lot[36-39] for the PEC applications due to their unique physical, chemical, and optical properties compared to bulk materials. In addition, they have potential to use cost-effective mass production of the device such as nanomaterial inks for printed electronics. [40] The number of publications with nano-materials has emerged significantly since 2000 as shown in Figure 1. 8.

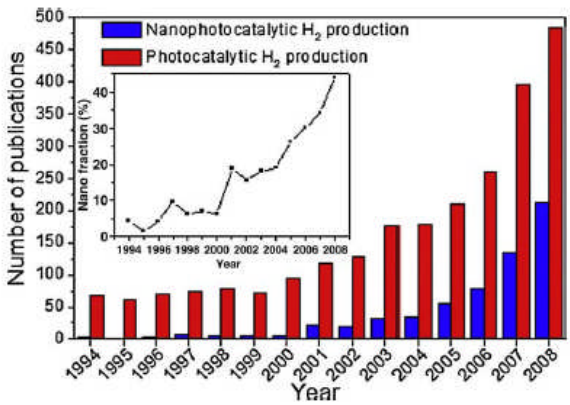

Figure 1.8. The number of publications on photocatalytic H_2 production versus the published year. The inset shows the fraction of publications with nanophotocatalysts.[36]

Nanoparticles and one-dimensional (1D) nanostructures such as nanowires and nanotubes can have several advantages over bulk materials for the PEC applications. First of all, those nanostructured materials can provide large semiconductor/electrolyte interface area where PEC chemical reactions happen due to their high surface to volume ratio. Their high surface area can be advantageous to increase the efficiency of interfacial charge transfer. Second, the nano-sized materials reduce the distance for photogenerated minority carriers to diffuse to the material surface. If the size of the nanomaterial is smaller than the diffusion length of minority carriers, photogenerated electron-hole pairs can separate efficiently before recombination within the material. (Figure 1.9) This is particularly important to increase the charge collection efficiency by reducing recombination rates when the diffusion length (or lifetime) of minority carrier is short such as Fe_2O_3.[41-42]

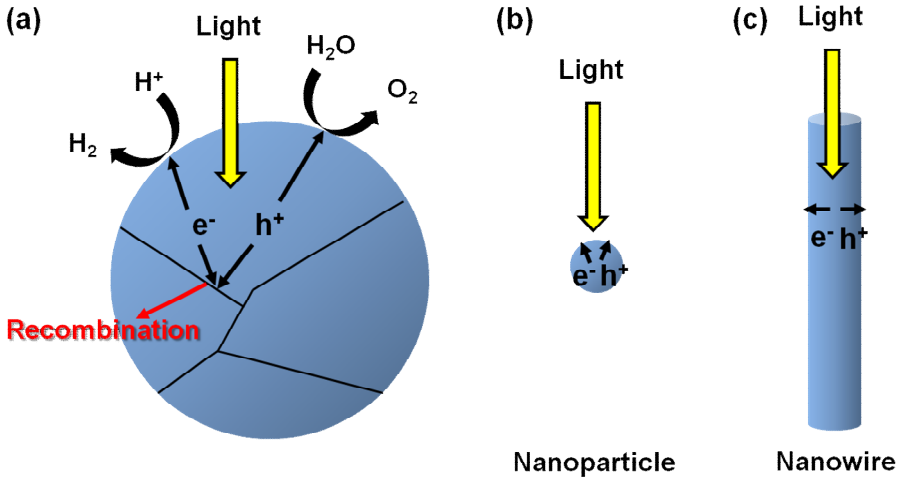

Figure 1.9. Schematic diagram showing electron-hole recombination and separation in (a) bulk material, (b) nanoparticle (0-dimensional nanostructure), and (c) nanowire (1-dimensional nanostructure). Photogenerated electron-hole pairs need to travel short distance to reach surface in nanostructured materials.

Third, E_g of the semiconductor materials can be tuned by varying their size to have desirable E_g for PEC water splitting such as MoS_2,[43] and the quantum size confinement can increase oscillator strength or absorption coefficient compared to bulk materials. Moreover, light trapping within oriented nanowire arrays [44] or light scattering with nanoparticles [45] have been demonstrated to increase the absorption of the incident light. Lastly, the unique bottom-up synthetic strategy allows the growth of the single-crystalline nanomaterials on different substrates [46-47] without the formation of dislocations or defects which can have been considered as trapping or recombination centers.

1D nanostructures such as nanowires and nanotubes are expected to have more improved charge transport properties than 0D nanostructures such as nanoparticles.[37-39]

People have been reported that the photoanodic currents for water oxidation increase with TiO_2 [35, 48-49] or Fe_2O_3 [50-51] nanowire [35, 48, 50-51] or nantube [39, 49] arrays due to the improved charge transport compared to nanoparticle thin films as shown in Figure 1.10. Charge carriers are required to hop between the nanoparticles to reach back contact electrode increasing the recombination losses at the boundaries, while they can transport efficiently along the nanowires or nanotubes. Moreover, vertically oriented 1D nanostructures can decouple the light absorption length and charge diffusion length, and thus enhance the charge collection efficiency despite short minority carrier diffusion length. (Figure 1.10b) For example, the small diameter of the nanowires reduces the distance for minority carriers to diffuse to the surface while the light can be absorbed along the nanowires.[8] These advantages offered by nanowire arrays have been demonstrated with various semiconductors such as TiO_2,[35, 48] ZnO,[52] $BiVO_4$,[53] and $KNbO_3$.[54] These reports support that nanowire is promising geometry to increase the quantum efficiency resulting in a high STH efficiency.

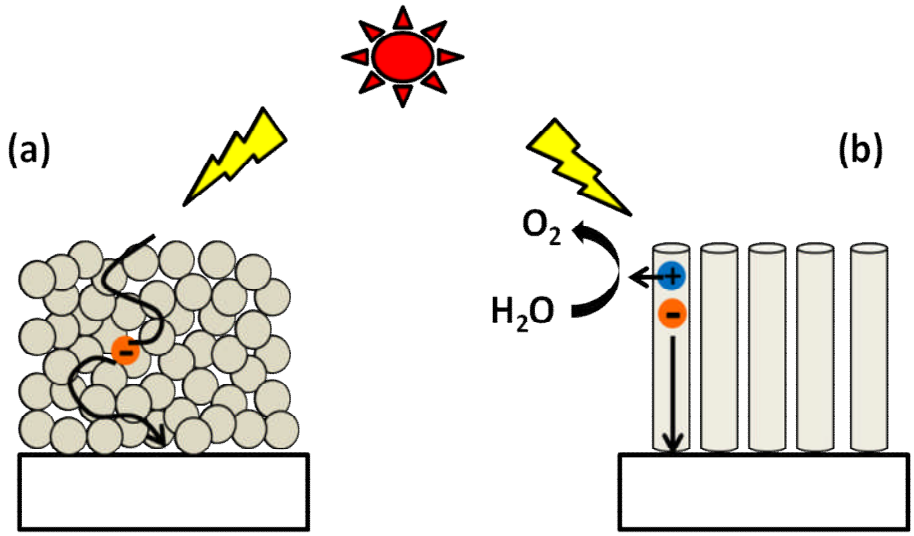

Figure 1.10. Schematic representation of the electron transport through (a) thin film of spherical nanoparticles, and (b) oriented nanowire arrays for water splitting. (b) shows the short hole diffusion length across the nanowire diameter and light absorption along the nanowires.

1.6 Research Objectives and Thesis Overview

This dissertation investigates photolysis of water with nanowire structured semiconductor photoelectrode to produce hydrogen which is a promising energy carrier as a future fuel. Several semiconductor materials are used to design advanced nanowire structures as a model system which can provide the directions how to enhance the STH

efficiency with current candidate materials as well as how to develop new semiconductor materials.

In **chapter 2**, TiO_2 nanowire arrays are investigated for photoanodic water splitting properties as a model system since TiO_2 has been the most heavily studied material for solar water splitting due to its capability of water oxidation and its stability. Photoanodic properties such as photocurrent density, the onset potential of photocurrents, and IPCE are compared with different lengths of hydrothermally grown TiO_2 nanowire arrays. The light absorption efficiency and charge collection efficiency of TiO_2 nanowire arrays are considered to understand the geometric effects. This chapter also examines the effect of atomic layer deposition (ALD) TiO_2 shell on the photoanodic properties with different lengths of TiO_2 nanowire arrays. It is proposed that the geometric and surface properties of semiconductors must be considered to achieve high water splitting efficiency.

In **chapter 3**, Si/TiO_2 heterojunction is designed as a dual semiconductor system since Si can compensate the lower conduction band potential for the hydrogen reduction while TiO_2 can protect the unstable core Si from photocorrosions. The planar Si and highly dense Si nanowire arrays coated by ALD TiO_2 thin film are tested for photocurrent measurements, and high surface are of nanowire is proposed for higher efficiency. In this dual semiconductor configuration, n-Si/n-TiO_2 and p-Si/n-TiO_2 core/shell nanowire junctions are compared to study the effect of the interface between two semiconductors on the photoanodic activities suggesting n/n heterojunction is more advantageous for the photoanode.

In **chapter 4**, an asymmetric Si/TiO_2 nanowire is fabricated to have a Si photocathode on one side for hydrogen evolution reaction and Si/TiO_2 photoanode on the other side for oxygen evolution reaction. The light induced vectorial charge separation within a single asymmetric nanowire is demonstrated using Kelvin probe force microscope (KPFM) to measure spatially resolved surface potential. Hydrogen evolution rates with the Si/TiO_2 asymmetric nanowire arrays vs Si/TiO_2 core/shell nanowire arrays are measured using gas chromatography. This study suggests that a photocathode/photoanode combination for water splitting can be realized with an asymmetric structure in nano-scale.

In **chapter 5**, Si/InGaN hierarchical nanowire structures are demonstrated as a potential candidate for solar water splitting. InGaN nanowire has been reported to have excellent bandgap tunability from the UV to the near IR region by alloying,[55] and valence bandedge of metal nitride is located higher than oxide semiconductors which make InGaN an attractive material for water splitting application. The Si/InGaN hierarchical nanowire arrays with extra high surface area are examined for the photoanode application in PEC water splitting cell.

In **chapter 6**, p-n PEC cells consisting of Si and TiO_2 nanowire structures are demonstrated in a two-electrode configuration for self-driven water splitting without bias voltage under illumination. A TiO_2 photoanode physically connected to a Si photovoltage cell is designed to increase the operating photocurrent of the p-n PEC cell by shifting the photoanodic I-V curves with the assistance of generate photovoltage from Si PV cell. To enhance the fill-factor of Si photocathode and its stability, surface modification with Pt or ALD TiO_2 is introduced, and the Si photocathode is linked with a Si PV embedded TiO_2 photoanode. These studies propose that the onset potential of the photocurrent and fill factor are important factor when we investigate semiconductor candidates to increase the operating current in the p-n PEC cell, and higher efficiency can be achieved with the combination of a PV cell.

In **chapter 7**, the contributions and perspectives of this dissertation are summarized.

References

[1] State of the World 2009, Worldwatch Institute, 2009, http://www.worldwatch.org/files/pdf/SOW09_chap3.pdf

[2] Keeling, C. D. *Ann. Rev. Energy. Env.* **1998**, *23*, 25-82.

[3] Global Warming Art http://www.globalwarmingart.com/wiki/Carbon_Dioxide_Gallery

[4] Lewis, N. S.; Nocera, D. G. *Proc. Natl. Acad. Sci. USA* **2006**, *103*, 15729-15735.

[5] http://en.wikipedia.org/wiki/World_energy_consumption

[6] http://en.wikipedia.org/wiki/Hydrogen_economy

[7] Nowotny, J.; Sorrell, C. C.; Sheppard, L. R.; Bak, T. *Int. J. Hydrogen Energy* **2005**, *30*, 521-544.

[8] Walter, M. G.; Warren, E. L.; Mckone, J. R.; Boettcher, S.W.; Santori, E. A.; Lewis, N. S. *Chem. Rev.* **2010,** *110*, 6446–6473.

[9] Fukishima, A.; Honda, K. *Nature* **1972**, 238, 37-38.

[10] Nozik, A. J. *Ann. Rev. Phys. Chem.* **1978**, *29*, 189-222.

[11] Gerischer H. Solar energy conversion, Seraphin BO, editor, Elsevier, Amsterdam, **1979**, 115–172.

[12] Sze, S. M.; Ng, K. K. Physics of Semiconductor Devices, Wiley, Hoboken, New Jersey, **2007**, 82-84.

[13] Bak, T.; Nowotny, J.; Rekas, M.; Sorrell, C. C. *Int. J. Hydrogen Energy* **2002**, *27*, 991-1022.

[14] Rajeshwar, K. *J. Appl. Electrochem.* **2007**, *37*, 765-787.

[15] Sheppard, L. R.; Nowotny, J. *Adv. Appl. Ceram.* **2007**, *106*, 9-20.

[16] Deutsch, T. G.; Koval, C. A.; Turner, J. A. *J. Phys. Chem. B* **2006**, *110*, 25297-25307.

[17] Wang, H.; Deutsch, T.; Turner, J. A. *J. Electrochem. Soc.* **2008**, *155*, F91-F96.

[18] Bolton, J. R.; Strickler, S. J.; Connolly, J. S., *Nature* **1985**, *316*, 495-500.

[19] Maeda, K.; Domen, K. *J. Phys. Chem. Lett.* **2010**, *1*, 2655-2661.

[20] Scaife, D. E. *Solar Energy* **1980**, *25*, 41-54.

[21] DOE Hydrogen Program, 2010 Annual Progress Report, http://www.hydrogen.energy.gov/pdfs/progress10/ii_g_4_turner.pdf

[22] Ni, M.; Leung, M. K. H.; Leung, D. Y. C.; Sumathy, K. *Renew. Sust. Energy Rev.* **2007**, *11*, 401-425.

[23] Meissner, D.; Memming, R.; Kastening, B.; Bahneman, D. *Chem. Phys. Lett.* **2007**, *127*, 419-423.

[24] Paracchino, A.; Laporte, V.; Sivula, K.; Grätzel, M.; Thimsen, E. *Nat. Mater.* **2011**, 10, 456-461.

[25] Grätzel, M. *Nature* **2001**, *414*, 338-344.

[26] Van de Walle, C. G.; Neugebauer, J. *Nature* **2003**, *423*, 626-628.

[27] Walukiewicz, W. *Physica B* **2001**, *302-303*, 123-134.

[28] Maeda, K.; Domen, K. *MRS Bulletin* **2011**, *36*, 25-31.

[29] Maeda, K.; Domen, K. *J. Phys. Chem. C.* **2007**, *111*, 7851-7861.

[30] Chen, Z. B.; Jaramillo, T. F.; Deutsch, T. G.; Kleiman-Shwarsctein, A.; Forman, A. J.; Gaillard, N.; Garland, R.; Takanabe, K.; Heske, C.; Sunkara, M.; McFarland, E. W.; Domen, K.; Miller, E. L.; Turner, J. A.; Dinh, H. N. J. *J. Mater. Res.* **2010**, *25*, 3-16.

[31] Gelderman, K.; Lee, L.; Donne, S. W. *J. Chem. Edu.* **2007**, *84*, 685-688.

[32] Measurements of PEC hydrogen production materials, U.S. Department of Energy , **2009**, http://www2.eere.energy.gov/hydrogenandfuelcells/pec_standards_review.html.

[33] Murphy, A. B.; Barnes, P. R. F.; Randeniya, L. K.; Plumb, I. C.; Grey, I. E.; Horne, M. D.; Glasscock, J. A. *Int. J. Hydrogen Energy* **2006**, *31*, 1999-2017.

[34] Schoonen, M. A. A.; Xu, Y.; Strongin, D. R.; *J. Geochem, Explor.* **1998**, *62*, 201.

[35] Cho, I. S.; Chen, Z.; Forman, A. J.; Kim, D. R.; Rao, P. M.; Jaramillo, T. F.; Zheng, X. *Nano. Lett.* **2011**, *11*, 4978-4984.

[36] Zhu, J.; Zäch, M. *Curr. Opin. Colloid Interface Sci.* **2009**, *14*, 260-269.

[37] Li, Y.; Zhang, J. Z. *Laser Photonics Rev.* **2010**, *4*, 517-528.

[38] Lin, Y.; Yuan, G.; Liu, R.; Zhou, S.; Sheehan, S. W.; Wang, D. *Chem. Phys. Lett.* **2011**, *507*, 209-215.

[39] Shankar, K.; Basham, J. I.; Allam, N. K.; Varghese, O. K.; Mor, G. K.; Feng. X.; Paulose, M.; Seabold, J. A.; Choi, K. S.; Grimes. C. A. *J. Phys. Chem. C.* **2009**, *113*, 6327-6359.

[40] Nanoparticle inks for printed electronics. NanoMas Tech. Inc. http://www.nanoparticles.org/pdf/YangZ.pdf

[41] Kay, A.; Cesar, I.; Grätzel, M. *J. Am. Chem. Soc.* **2006**, *128*, 15714-15721.

[42] Sivula, K.; Zboril, R. ; Le Formal, F.; Robert, R.; Weidenkaff, A.; Tucek, J. ; Frydrych, J.; Grätzel, M. *J. Am. Chem. Soc.* **2010**, *132*, 7436-7444.

[43] Chen, Z.; Kibsgaard, J.; Jaramillo, T. F. Solar Hydrogen and Nanotechnology V, edited by Hicham Idriss, Heli Wang, *Proc. of SPIE* **2010**, *7770*, 77700K.

[44] Garnett, E.; Yang, P. *Nano. Lett.* **2010**, *10, 1082-1087*.

[45] Kelzenberg, M. D.; Boettcher, S. W.; Petykiewicz, J. A.; Turner-Evans, D. B.; Putnam, M. C.; Warren, E. L.; Spurgeon J. M.; Briggs, R. M.; Lewis, N. S.; Atwater, H. A. *Nat. Mater.* **2010**, *9*, 239-244.

[46] Kuykendall, T.; Ulrich, P.; Aloni, S.; Yang, P. *Nat. Mater.* **2007**, *6*, 951-956.

[47] Hahn, C.; Zhang, Z.; Fu, A.; Wu, C. H.; Hwang, Y. J.; Gargas, D. J.; Yang, P. *ACS Nano*, **2011**, 5, 3970-3976.

[48] Khan, S. U.; Sultana, T. *Sol. Energy Mat. Sol. Cells* **2003**, *76*, 211-221.

[49] Park, J. H.; Kim, S.; Bard, A. J. *Nano. Lett.* **2005**, *6*, 24.

[50] Lindgren, T.; Wang, H. L.; Beermann, N.; Vayssieres, L.; Hagfeldt, A.; Lindquist, S. E. *Sol. Energy Mat. Sol. Cells* **2002**, *71*, 231.

[51] Beermann, N.; Vayssieres, L.; Lindquist, S. E.; Hagfeldt, A. *J. Electrochem. Soc.* **2000**, *147*, 2456.

[52] Ahn, K. S.; Shet, S. ; Deutsch, T. ; Jiang, C. S.; Yan, Y. F.; Al-Jassim, M.; Turner, J. A. *J. Power Sources* **2008**, *176*, 387.

[53] Su, J.; Guo, L.; Yoriya, S.; Grimes, C. A. *Cryst. Growth Des.* **2009**, *10*, 856.

[54] Ding, Q. P.; Yuan, Y. P.; Xiong, X.; Li, R. P.; Huang, H. B.; Li, Z. S.; Yu, T.; Zou, Z. G.; Yang, S. G. *J. Phys. Chem. C* **2008**, *112*, 18846.

[55] Kuykendall, T.; Ulrich, P.; Aloni, S.; Yang, P. *Nat. Mater.* **2007**, *6*, 951-956.

Chapter 2

Photoelectrochemical Properties of TiO_2 Nanowire Arrays: A Study on the Dependence of Length and Atomic Layer Deposition Coating

2.1 Introduction

Artificial photosynthesis has been considered as a desirable approach to supply clean energy since it can capture and convert the energy of sunlight into the chemical bonds of a fuel such as hydrogen.[1] Solar water splitting to convert water into hydrogen and oxygen is one of the most attractive forms of artificial photosynthesis. Since Honda and Fujishima demonstrated water splitting with TiO_2 in 1972,[2] the photoanodic properties of TiO_2 (rutile) have been widely studied [3-5] because it is highly resistant to photocorrosion, non-toxic, abundant, and cheap. However, TiO_2 has too wide of a bandgap (3.0 eV) [6] to absorb sunlight in the visible region, and its low electron mobility (1 $cm^2v^{-1}s^{-1}$) [7] and short minority carrier (hole) diffusion length (10~100 nm) [6, 8] limit its quantum efficiency even in the UV region.

Nanostructured TiO_2 has been demonstrated [9-12] to increase its quantum efficiency for water splitting since recombination can be mitigated by decreasing the distance necessary for the minority carrier to diffuse to the surface. In particular, one dimensional (1D) nanostructures such as nanowire, and nanotube arrays are advantageous over planar geometries because they can decouple the directions of light absorption and charge carrier collection.[13-16] TiO_2 nanowire arrays can have efficient charge transfer at the TiO_2/electrolyte interface despite a short hole diffusion length because the hole only needs to diffuse across the radius of the nanowire.[1,13] However, the low electron mobility in rutile TiO_2 can be an obstacle because electrons must transport along the nanowires to reach the electric contact.[17] To date, 1D nanostructured TiO_2 has been investigated, but the length dependence on water splitting activity has not been systematically studied.

The surface properties of nanostructures are especially important to the overall charge collection efficiency since they can influence the recombination velocity and the chemical reaction dynamics. Surface states in nanostructures can be different depending on the preparation method.[8] One method to decrease surface recombination velocity is a surface coating.[18] Atomic layer deposition (ALD) is a coating technique that can passivate surface states to decrease the surface recombination velocity.[19] Its layer-by-layer deposition allows for highly conformal coating even on the dense and rough surfaces of certain nanostructures. Formal *et al*. demonstrated that a thin layer of Al_2O_3 deposited by ALD on nanostructured Fe_2O_3 can lower the onset of the photocurrents by passivating surface states.[20]

For the ALD coating to have a beneficial effect on the water splitting efficiency, several factors should be considered for choosing the right material. First, an interface between the ALD layer and the semiconductor material should be considered. For example, large lattice mismatch can cause non-uniform coating and addition defects due to strain. Paracchino *et al.* reported ZnO and Al_2O_3 buffer layers was introduced to relax the strain at the interface which can increase stability of the TiO_2 ALD layer on the p-CuO electrode.[21] Second, the ALD layer should have the right band alignments with the semiconductor to prevent additional energetic barriers for charge carriers.[21-22] The valence band potential of the ALD shell should be equal or higher than that of rutile TiO_2 to allow efficient hole transfer. In addition, the valence band potential of the ALD shell should be lower in energy than the water oxidation potential to allow the reaction to be thermodynamically favorable. A coating of ALD TiO_2 on rutile nanowire arrays could satisfy all of the aforementioned factors.

This chapter will describe a quantitative study on the dependence of nanowire length and ALD TiO_2 coating on the IPCE of TiO_2 nanowires as a model system for photoelectrochemical (PEC) water splitting. From these results, this chapter demonstrates that the efficiency of the TiO_2 nanowire arrays can be improved by increasing the length of

the nanowires as well as by coating the surface with an ALD shell. These geometric studies of TiO_2 nanowire arrays can offer a strategy towards optimizing the energy conversion efficiency with other semiconductor materials in solar water splitting.

2.2 Synthesis of TiO_2 Nanowire and Measurement

2.2.1 Hydrothermal TiO_2 Nanowire Arrays Growth

TiO_2 nanowire photoanodes were prepared by growing nanowire arrays on FTO.[23] Deionized water (5 ml) was mixed with hydrochloric acid (5 ml, 36.5%-38% by weight) and stirred for 5 min before titanium isopropoxide (0.167 ml, TTIP, 97% Aldrich) was added. After stirring for 6 hrs, the mixture solution was transferred to a Teflon-lined stainless steel autoclave. Clean FTO/glass substrates (area 5 cm^2) were immersed with the conducting side face down. The autoclave was put in an oven at a temperature of 200 ^oC and was taken out from the oven after 50~150 min to control the nanowire length. After the autoclave was cooled down for 2 hrs to room temperature, the FTO substrate was rinsed with DI water and subsequently annealed at 400 ^oC for 1hr in air. TiO_2 nanowires grew only on the side of the FTO substrate where it was immersed in the growth solution. The final area of the nanowire arrays was approximately 2.6 ~2.8 cm^2.

2.2.2 Optical Characterization

The absorption properties of TiO_2 nanowire arrays on FTO substrates were obtained with an integrating sphere (ISR-3100, Shimadzu Corp.) and UV-Vis spectrophotometer (UV-3101 PC, Shimadzu Corp.). Since the FTO substrate was 3 mm thick, scattering was not completely accounted for in the transmission or reflection spectra. Therefore, absorption plus residual scattering were calculated from 100 - Reflectance – Transmission (%).

2.2.3 Photoelectrochemical Measurement

Photocurrents of TiO_2 nanowire electrodes were measured with a potentiostat (Gamry Ref 600) using an Ag/AgCl reference electrode and a Pt mesh counter electrode. A 300 W Xe lamp (Newport, 6258) was coupled with an AM 1.5 filter (Newport, 81094) to simulate sunlight, and a diffuser was used for uniform illumination intensity (100 mW/cm^2) over the entire TiO_2 nanowire electrode area (2.6 ~ 2.8 cm^2). TiO_2 nanowire photoanodes were immersed in 1M NaOH and illuminated through a quartz window of a glass cell. For the incident photon to current conversion efficiency (IPCE) measurement, a 300 W Xe lamp was coupled with a monochromator (Newport, cornerstone 130), and the incident

light intensity was measured with a calibrated Si photodiode. The IPCE was calculated from the photocurrents measured at 1.5 V versus RHE according to the following equation.

$$IPCE = \frac{I_{ph}\ (mA/cm^2) \times 1239.8\ (V \times nm)}{P_{mono}\ (mW/cm^2) \times \lambda\ (nm)} \tag{1}$$

2.3 TiO_2 Nanowire Arrays Photoanode

2.3.1 TiO_2 Nanowire Characterization

To study the photoanodic activity dependence on the length of TiO_2 nanowires, four different lengths of TiO_2 nanowire arrays were prepared on FTO from a hydrothermal method[23] by controlling the growth time between 50 min and 150 min at the same growth temperature (200 ^{o}C). When the growth time exceeded 3 hrs, TiO_2 nanowire arrays started to delaminate from the FTO substrate and form a white thin film due to the competition between crystal growth and dissolution at the FTO-nanowire interface.[23]

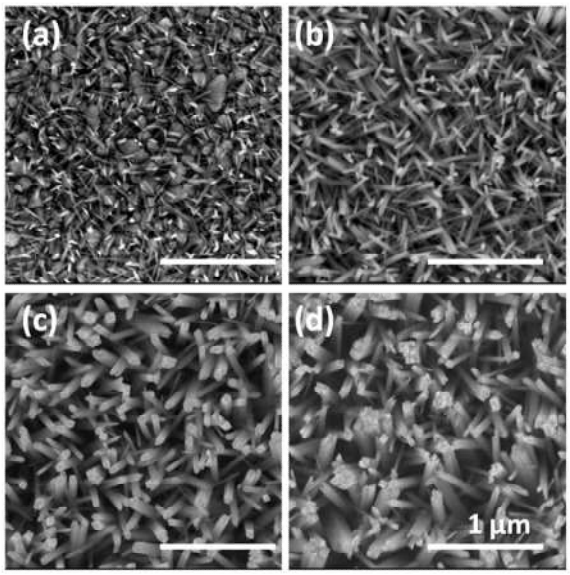

Figure 2.1. SEM images of hydrothermally grown TiO_2 nanowires on FTO substrates for (a) 50 min, (b) 60 min, (c) 80 min, and (d) 150 min at 200 ^{o}C.

Figure 2.1 shows top down scanning electron microscope (SEM) images of TiO_2 nanowire arrays grown on FTO. The bare FTO substrate was still visible within 50 min (Figure 2.1a) due to the short length and low density coverage of nanowire arrays. After 60 min, TiO_2 nanowire arrays completely covered the FTO substrate (Figure 2.1b-d). The average length of the nanowire arrays were measured (see Figure 2.9) to be 0.28 (± 0.03), 0.4 (± 0.05), 0.9 (± 0.08), and 1.8 (± 0.1) μm for growth times of 50, 60, 80, and 150 min respectively.

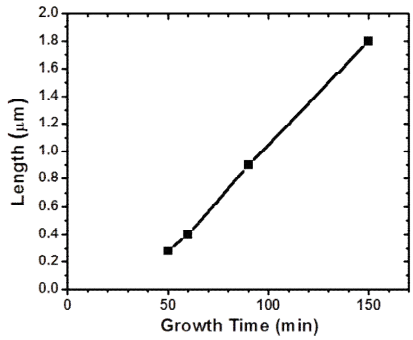

Figure 2.2. Plot of nanowire lengths vs time showing that the growth rate is linear.

The length of the nanowires linearly increased with time (T) (Figure 2.2, Equation 2) at a growth rate of 0.015 μm/min. A delay of 33 min was seen in the nucleation of TiO_2 nanowires due to the time required to heat the autoclave up to 200 ^{o}C and supersaturation of TiO_2.

$$Length\ (\mu m) = 0.015 \times (T\ (\text{min}) - 33) \tag{2}$$

2.3.2 TiO_2 Nanowire Photocurrents

PEC measurements were performed on four different lengths of TiO_2 nanowire arrays (Figure 2.3) with the electrodes mentioned above. Photocurrent measurements (Figure 2.3a) show that the onset potentials of photocurrents (0.1 V vs RHE) remain the same as the length of the nanowires increase. The onset potential of photocurrents is mainly determined by the properties of rutile TiO_2, such as the over potential of the oxidation reaction and the flat band potential,[22, 24] which were not influenced by the length of the nanowires or the growth time. Nanowires showed an increase in photocurrent with length, which is expected since longer nanowires have longer optical pathway. The highest photocurrent (0.73 mA/cm^2 at 1.5 V vs RHE) was observed for 1.8 μm long nanowires within the experiment conditions (0.28 ~ 1.8 μm). This is 40 % of the maximum

photocurrent density (1.8 mA/cm^2) for rutile TiO_2 under AM1.5G simulated sunlight illumination, assuming a quantum efficiency (QE) of 100% below the bandgap (3.0 eV).

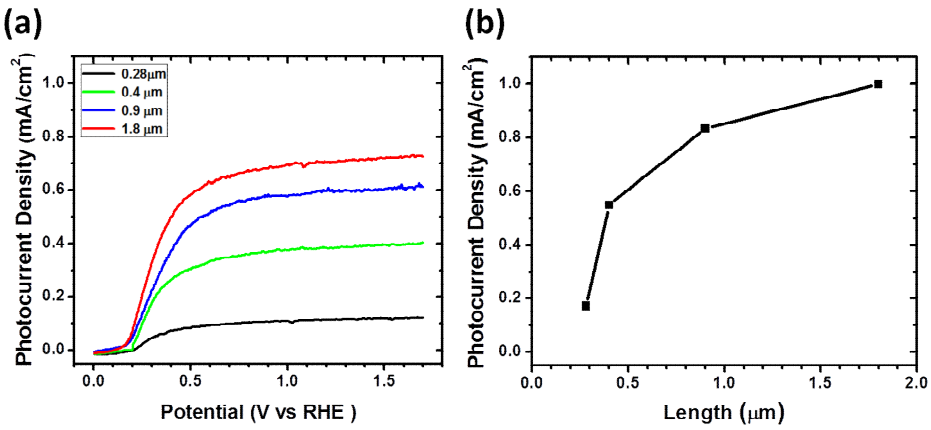

Figure 2.3. (a) Plots of photocurrent density vs RHE for TiO_2 nanowire arrays show an increase in photocurrent with nanowire length. (b) Photocurrent densities are compared at 1.5 V vs RHE for different nanowire lengths and show that the current begins to saturate with longer nanowires.

The photocurrent densities (1.5 V vs RHE) are plotted vs nanowire length in Figure 2.3b, showing that the photocurrent does not increase linearly with length. For example, the photocurrent increased by 0.275 mA/cm^2 (from 0.125 mA/cm^2 to 0.4 mA/cm^2) when the length grew from 0.28 μm to 0.4 μm, while it increased only by 0.12 mA/cm^2 (from 0.61 mA/cm^2 to 0.73 mA/cm^2) when the length grew from 0.9 μm to 1.8 μm. The shape of the curve implies that the photocurrent is close to saturation with a length of 1.8 μm for TiO_2 nanowires.

2.3.3 TiO_2 Nanowire External Quantum Efficiency

The effect of nanowire length on photocurrent can be discussed in more detail by comparing the wavelength (λ) dependence on the light absorption and the IPCE of TiO_2 nanowires (Figure 2.4). The absorption of light depends on the optical absorption length (x) and the absorption coefficient (α) where $\mathrm{Im}(n_s)$ is imaginary part of the refractive index (Equations 3-4).

$$A = \alpha x = -\log(\frac{I}{I_o}) \tag{3}$$

$$\alpha = \frac{4\pi\,\mathrm{Im}(n_s)}{\lambda} \tag{4}$$

The IPCE or external quantum efficiency (EQE) takes into account three efficiencies: photon absorptance (η_{e^-/h^+}), charge transport within semiconductor materials ($\eta_{transport}$), and charge transfer at the semiconductor/electrolyte interface ($\eta_{transfer}$) (Equation 5).[25] Here, the efficiency of photon absorptance is defined as the fraction of electron hole pair generation per incident photon flux, which can be related to the absorption length (Equation 6).

$$IPCE(\lambda) = EQE(\lambda) = \eta_{e^-/h^+}(\lambda) \times \eta_{transport}(\lambda) \times \eta_{transfer}(\lambda) \quad (5)$$

$$\eta_{e^-/h^+} = \frac{I_o - I}{I_o} = 1 - \frac{I}{I_o} = 1 - 10^{-\alpha x} \quad (6)$$

The IPCE was measured at 1.5 V vs RHE where the photocurrents of the nanowires were saturated (Figure 2.4a). As the nanowires increase in length, the enhancement in IPCE is significant. This is especially true between λ = 380~420 nm since α(λ) of rutile TiO_2 decreases significantly in this region.[26] At λ = 380 nm, the IPCE increases from 4.2% to 57.0%, as the length of the nanowires increases. A plot of IPCE vs efficiency of photon absorptance ($\eta_{e^-/h^+} = 1 - 10^{-\alpha x}$) at λ=410 nm is illustrated in Figure 2.4b where α(410 nm) = 0.5 × 10^3/cm,[27] assuming TiO_2 nanowires have the same absorption length as bulk TiO_2, and x is the average length of the nanowires. A strong linear correlation (R^2 = 0.993) between IPCE and $1 - 10^{-\alpha x}$ is observed except for the IPCE of 0.28 μm long nanowire arrays. The IPCE for the 0.28 μm sample is lower than the expected value because the nanowires do not cover the FTO substrate entirely (Figure 2.1a). The strong linear correlation verifies that the EQE of TiO_2 nanowire arrays is strongly influenced by the absorption of photons near the bandgap.

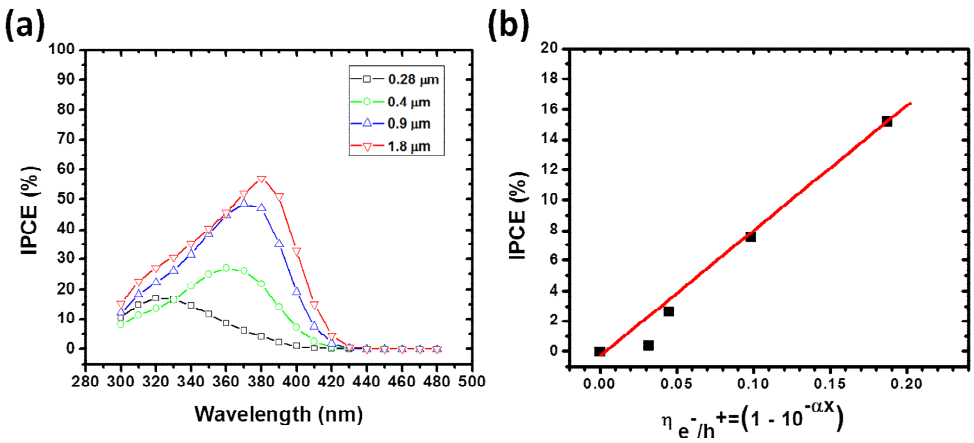

Figure 2.4. (a) IPCE (1.5 V vs RHE) of TiO_2 nanowire arrays electrodes show a shift in λ at the maximum EQE (λ (x=0.28 μm) = 320 nm, λ (x=0.4 μm) = 360 nm, λ (x=0.9 μm) = 370 nm, λ (x=1.8 μm) = 380nm). (b) A plot of IPCE versus $1 - 10^{-\alpha x}$ (absorption efficiency, $\eta_{e-/h+}$) shows that the IPCE has a linear correlation near the band edge (λ= 410 nm) of the TiO_2. $IPCE(\%) = 82.58 \times (1 - 10^{-\alpha x}) - 0.485, \quad R^2 = 0.993$

The maximum IPCE for TiO_2 nanowires shifts in wavelength as the length of nanowires increases, indicating some changes in dynamics for carrier collection (Figure 2.4a). Nanowires which are 1.8 μm long have a maximum IPCE at 380 nm which is consistent with other reports for rutile TiO_2.[17] Due to efficient light absorption with a larger α, [26-27] an increase in IPCE is expected at shorter wavelengths. However, at the shorter wavelengths, the IPCE of TiO_2 decreases since a fraction of the photogenerated majority carriers in the depletion region can diffuse to the electrolyte interface against the electric field and thus oppose the photocurrent by recombining with holes.[28] The effects of electron diffusion losses are significant when the majority carrier's mobility is low and/or there is a high density of interface states which creates a large recombination velocity. Higher energy photons at wavelengths shorter than 380 nm are mainly absorbed by the top part of the nanowires. Therefore, a lower charge collection efficiency is expected because these electrons must travel the entire length of the nanowire to reach the FTO back contact. As the length of TiO_2 nanowires decreases, the maximum IPCE shifts to shorter wavelengths. This implies that $\eta_{transport}(\lambda)$ and $\eta_{transfer}(\lambda)$ are important factors for the IPCE in the short wavelength region while $\eta_{e^-/h^+}(\lambda)$ is more significant near the bandgap illumination. Therefore, the longer nanowire arrays can enhance the EQE by increasing the absorption efficiency $(1-10^{-\alpha x})$ but are unfavorable for charge collection at the short wavelengths. This also explains the trend of photocurrent dependence on nanowire length that we observed in Figure 2.3b For TiO_2 nanowire arrays, it is necessary to improve the charge collection efficiency before growing longer nanowire arrays to increase the energy conversion efficiency.

2.4 TiO_2 Nanowire Arrays with ALD TiO_2 Shell Deposition

2.4.1 ALD TiO_2 Shell Deposition

ALD was tested to deposit a TiO_2 shell on rutile TiO_2 nanowires to increase charge collection efficiency by reducing surface states.[8,20] The TiO_2 samples were cleaned with isopropanol and DI water followed by drying with N_2 gas using a gun before ALD deposition. The exposed bare FTO substrate, where no TiO_2 nanowires were grown, was protected with aluminium foil and kapton tape to avoid direct deposition on the FTO surface. Shells were deposited on TiO_2 nanowire arrays by using a home-made ALD system at 300 ^oC with $TiCl_4$ (99.990%, Alfa) and pure DI water as the precursors. A series of shell thicknesses were deposited with various number of ALD cycles from 60 to 450 cycles on 1.8 μm long TiO_2 nanowires to examine the photocatalytic performance dependence on shell thickness.

2.4.2 ALD TiO_2 Shell Characterization

The ALD shell was characterized with high resolution transmission electron microscopy (JEOL JEM-2100 LaB6), X-ray diffraction (Bruker AXS D8 Advance), and Raman spectroscopy (HORIBA Jobin Yvon Inc).

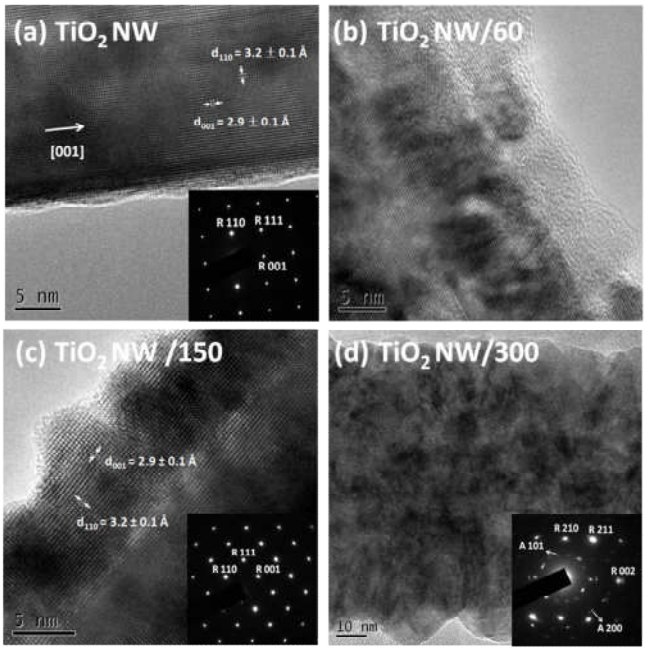

Figure 2.5. HRTEM images of TiO_2 nanowires with (a) no shell and nanowires with (b) 60, (c) 150, (d) and 300 ALD cycles of TiO_2. HRTEM images as well as SAED patterns (insets) show a phase change for the shell from rutile (150 cycles) to anatase (300 cycles) as the thickness increases.

First, Figure 2.5a shows a high resolution transmission electron microscopy (HRTEM) image and the corresponding selected area electron diffraction (SAED) pattern of a bare TiO_2 nanowire confirming that nanowires are grown in the <001> direction with the rutile crystal structure. When 60 cycles of TiO_2 is deposited, the ALD shell is about 5~7 nm thick and is composed of crystalline particles and an amorphous layer (Figure 2.5b). With 150 cycles of TiO_2, no amorphous layer was observed and epitaxial grains of rutile TiO_2 extend 13~15 nm from the surface of the TiO_2 nanowire (Figure 2.5c). When 300 cycles of TiO_2 is deposited, the shell has a polycrystalline anatase structure ($d_{101} = 3.5 \pm 0.1$ Å) with a shell thickness of 25~30 nm (Figure 2.5d). From the TEM study, we find that a phase transition of rutile to anatase TiO_2 happens as thicker ALD layers are deposited although rutile is more thermodynamically stable. Different phases of ALD TiO_2 have been reported depending on the substrate and the growth temperature.[29] More structural studies

are required to understand the unusual phase transitions of ALD TiO_2 on rutile nanowire surfaces.

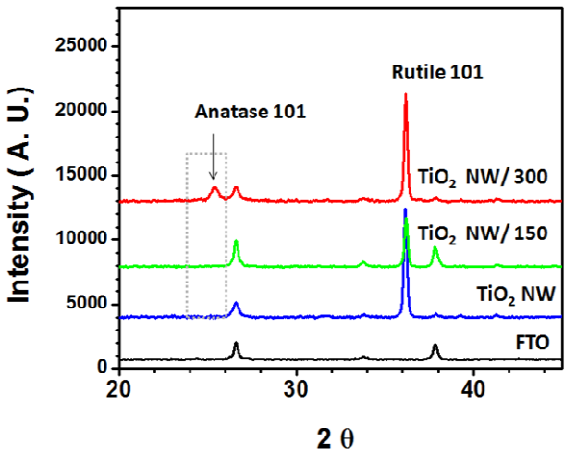

Figure 2.6. X-ray diffraction patterns confirm the appearance of the anatase (101) peak.

X-ray diffraction patterns of the ALD TiO_2 samples are consistent with TEM characterization showing anatase formation as the shell thickness increases. As grown TiO_2 nanowires and TiO_2 nanowires with 150 ALD cycles have the rutile 101 and FTO substrate peaks (Figure 2.6). However, the anatase 101 peak was observed for the sample with 300 ALD cycles indicating that the shell has the anatase phase with primarily the 101 orientation. Similarly, Raman spectroscopy (Figure 2.7) of TiO_2 nanowires with 300 ALD cycles shows characteristic peaks associated with the anatase phase (141 cm^{-1} E_g and 515 cm^{-1} A_{1g} and B_{1g}) [30] while only rutile peaks were observed with 150 ALD cycles.

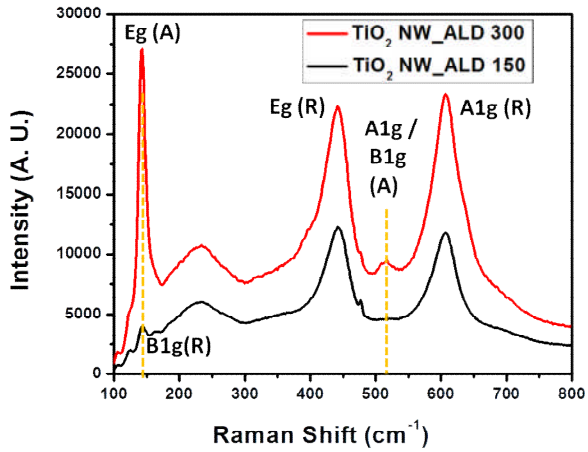

Figure 2.7. Raman shifts TiO_2 nanowires with 150 (black) and 300 ALD cycles (red). The peaks at 140 cm^{-1}, 441 cm^{-1} and 606 cm^{-1} are associated with the rutile B_{1g}, E_g, and A_{1g} modes respectively. The peaks at 141 cm^{-1} and 515 cm^{-1}, for nanowires with 300 ALD cycles, are associated with the Eg and A_{1g} /B_{1g} modes of the anatase phase.

2.5 ALD Shell Effects on Photoanodic Properties

2.5.1 ALD TiO_2 Shell Thickness Dependence

To examine the dependence of shell thickness on the PEC properties of ALD coated TiO_2 nanowires, we compared the photocurrents of 1.8 μm nanowires with different shell thicknesses (Figure 2.8). With a thin shell (60-100 cycles), the photocurrent (1.5 V vs RHE) is decreased up to 70% most likely because the amorphous layers formed at these thicknesses can block charge transfer across the TiO_2/electrolyte junction. Also, the continuous amorphous shell can decrease the photovoltage at the TiO_2/electrolyte junction which is the driving force for charge separation. As the shell increases in thickness and crystallizes into pure rutile TiO_2 (150 cycles), the current density reaches a maximum of 1.1 mA/cm^2 (1.5 V vs RHE). With this current density increase, ALD coated TiO_2 nanowires can obtain 61% of the maximum photocurrent (1.8 mA/cm^2) under AM1.5G simulated sunlight illumination. We propose that the performance increase is due to the role of the epitaxial rutile shell in suppressing surface recombination rates by passivating charge trapping sites.

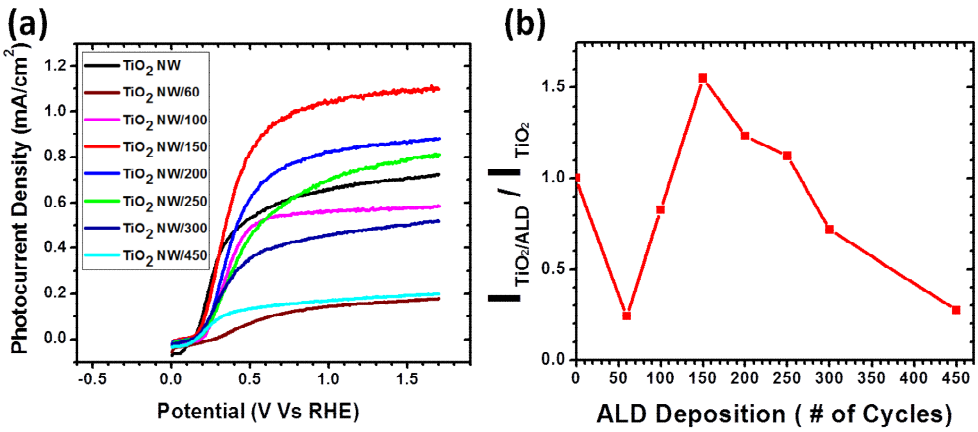

Figure 2.8. Plots of photocurrent densities vs RHE for 1.8 μm long TiO_2 nanowire arrays electrodes with various ALD cycles (60, 100, 150, 200, 250, 300, and 450 cycles). (b) A plot of normalized photocurrent densities ($I_{TiO_2/ALD} / I_{TiO_2}$) vs the number of ALD cycles shows a maximum enhancement at 150 cycles. Normalized current densities were obtained at 1.5 V vs RHE.

After the shell undergoes a phase transition to anatase (300~450 cycles), the photooxidation activity clearly decreases with increasing thickness. This implies that the anatase shell blocks efficient hole transfer from the rutile core to the electrolyte. To understand why the anatase shell is decreasing the overall photocatalytic activity we can consider both the structural and electronic characteristics of the junction between the shell and the core. First, we can examine the structure of the core/shell nanowires from HRTEM

images. Figure 2.5d shows that the anatase shell does not grow epitaxially from the rutile core due to lattice mismatch. The polycrystalline nature of the anatase shell can introduce new interfacial states and grain boundaries which can decrease the efficiency of hole transfer at the interface. Second, we can consider the band alignment between the two phases of TiO_2 to determine whether charge transfer is favorable. Anatase TiO_2 (3.2 eV) has a 0.2 eV larger bandgap when compared to rutile TiO_2 (3.0 eV). Since both anatase and rutile phases are typical n-type semiconductors, their Fermi levels can be considered to be close to their conduction band edges in energy.[31-32] Therefore, after contact and thermal equilibrium where the Fermi levels of rutile and anatase are equal, the valence band of rutile should be higher in energy than that of anatase. Because of this offset, the hole feels an energetic barrier to transfer from rutile to anatase, and we expect the photocatalytic activity to decrease when the anatase shell completely covers the rutile core. This is in contrast to mixtures of rutile and anatase phases, which have higher activity than either pure phase, because both phases in that geometry are exposed to the electrolyte.[13,33] These results emphasize that the phase of the ALD shell can have a significant influence on photocatalytic activity. Based on these results, we conclude that an epitaxial rutile ALD shell can increase water splitting efficiency with rutile TiO_2 nanowires.

The normalized photocurrent densities ($I_{TiO_2/ALD} / I_{TiO_2}$) at 1.5 V vs RHE were also compared vs the number of ALD cycles (Figure 2.8b) to show the change in performance between as made and ALD coated nanowires. The photocurrents were enhanced compared to bare TiO_2 nanowire arrays between 150~250 cycles of ALD coating, while the photocurrent decreased for all other thicknesses. A maximum of 1.5 times enhancement was obtained with 150 ALD cycles.

2.5.2 TiO_2 Nanowire Length Dependence

Additional PEC measurements were performed on TiO_2 nanowires with different lengths but the same shell thickness (150 cycles) to examine the effects of the epitaxial rutile ALD shell on photocatalytic activity. Top down and cross sectional SEM images were taken of 0.28, 0.4, 0.9, and 1.8 μm long TiO_2 nanowires with 150 ALD cycles (Figure 2.9). The cross section images show that the nanowire arrays are dense and slightly off-vertical.

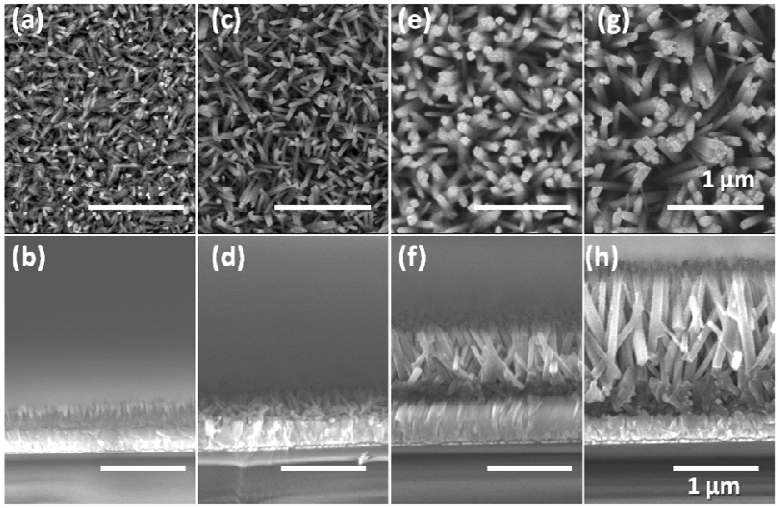

Figure 2.9.Top down and cross sectional SEM images of TiO_2 nanowire arrays, with 150 ALD cycles, grown on FTO substrates. The core TiO_2 nanowire arrays were grown for 50 (a,b), 60 (c,d), 80 (e,f), and 150 min (g,h) at 200 ^{o}C. Average nanowire lengths were 0.28, 0.4, 0.9, and 1.8 µm respectively.

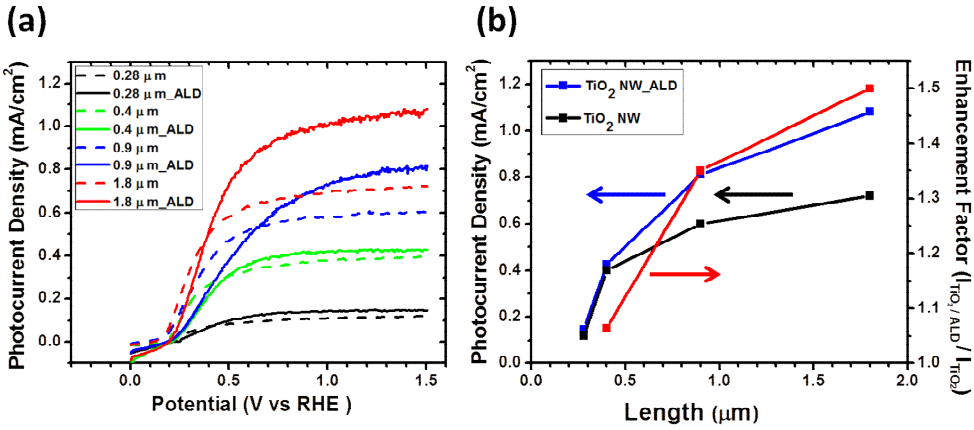

Figure 2.10. (a) Photocurrent densities for TiO_2 nanowires of different lengths are shown for nanowires with and without 150 ALD cycles. (b) Plots of photocurrent densities (1.5 V vs RHE) and enhancement factors ($I_{TiO_2/ALD}$ / I_{TiO_2}) vs the length of TiO_2 nanowire arrays.

Figure 2.10 shows the photocurrent densities of TiO_2 nanowire arrays with (solid lines) and without (dot lines) ALD coating. The photocurrent is enhanced with ALD coating regardless of the length of the nanowire, although the amount of increase is different. The enhancement factors, defined as the normalized photocurrent densities

($I_{TiO_2/ALD}$ / I_{TiO_2}) at 1.5 V vs RHE, were plotted vs the length of the nanowire arrays (Figure 2.10b) to quantify the increase in performance. The enhancement factor increases with nanowire length between 0.4 ~ 1.8 μm. It is most likely higher for the 0.28 μm long nanowires because the amount of TiO_2 deposited is relatively large since the FTO surface is not completely covered by nanowires.

2.5.3 ALD TiO_2 Shell Effects on External Quantum Efficiency

To determine the effect of the ALD shell on the EQE of different nanowire lengths, we measured the IPCE of TiO_2 nanowires with and without ALD coating (Figure 2.11). Nanowires with the ALD shell show varying levels of increase in IPCE depending on the nanowire length as well as the wavelength of light. The most prominent enhancement in IPCE was observed at shorter wavelengths (below the peak IPCE wavelength) with longer nanowires. For example, the IPCE of 1.8 μm long TiO_2 nanowire arrays with ALD coating is enhanced significantly at $\lambda < 380$ nm although it remains similar at higher wavelengths near the bandgap of rutile TiO_2.

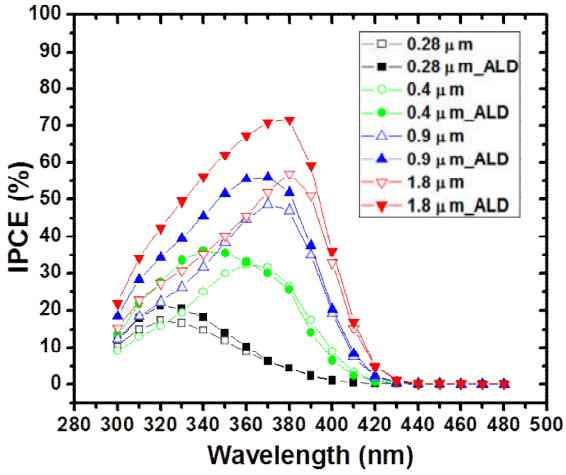

Figure 2.11. IPCE (1.5 V vs RHE) for TiO_2 nanowires of different lengths are shown for nanowires with and without 150 ALD cycles. The EQE is mainly enhanced at λ = 320~380 nm.

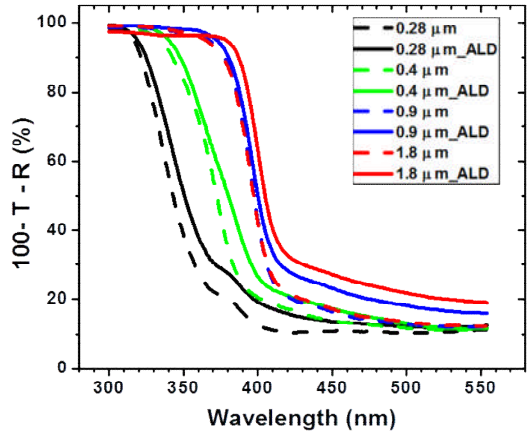

Figure 2.12. 100 - Transmission - Reflection (%) for the corresponding TiO_2 nanowire arrays.

By comparing the wavelength dependence of the enhancement in IPCE from ALD coating (Figure 2.11) to optical measurements (Figure 2.12) we can determine whether they are correlated. Figure 2.12 shows the optical properties of TiO_2 nanowire arrays on the FTO substrate with and without ALD coating. Due to a thick FTO/glass substrate, the scattering was not completely accounted for in the transmittance or reflectance spectra, so 100 - Reflectance - Transmission (%) indicates the absorption plus scattering. The absorption plus scattering for 1.8 μm long TiO_2 nanowire arrays is higher than 98 % at $\lambda < 370$ nm even without the ALD shell, so the improvement in absorption from ALD is minimal in this region. However, the ALD shell enhances the IPCE of TiO_2 nanowires at $\lambda < 390$ nm despite a minute amount of increase in the absorption of light. At longer wavelengths ($\lambda >$ 380 nm), TiO_2 nanowires with 150 ALD cycles have slightly higher absorption plus scattering. In contrast, the IPCE is similar with or without the ALD shell near the band edge region ($\lambda > 390$ nm). Therefore, we can conclude that the increase in IPCE is not due to a change in absorption efficiency (η_{e^-/h^+}).

Instead, the enhancement at $\lambda < 390$ nm from the ALD coating could be due to several factors affecting charge collection efficiency including $\eta_{transport}(\lambda)$ and $\eta_{transfer}(\lambda)$. First, the interface recombination velocity is expected to decrease when the ALD shell passivates surface states on TiO_2 nanowires. Salvador reported that the electron-hole recombination in TiO_2 is governed by a trapping mechanism in which the hole lifetime (τ_p) depends on the density of recombination centers.[8] The minority carrier diffusion length (L_p) is related to the lifetime by the following equation: $L_p = \sqrt{D_p \tau_p}$ where D_p is the diffusivity.[18] Passivation can increase the diffusion length of the hole by reducing recombination and can therefore increase the size of the active region since the active

region is L_p + W (width of the space-charge region), and decrease electron diffusion losses.[28]

Also, an increase in semiconductor/electrolye junction area has been demonstrated to be beneficial[12,17] for water splitting since the increase in surface area allows for holes to transfer more efficiently to the electrolyte. The HRTEM image in Figure 2.5c clearly shows that the ALD shell increases the surface area when compared to the as made TiO_2 nanowire (Figure 2.5a), and provides a larger area for the water oxidation reaction to happen. The rough surface also indicates that the sidewall of ALD coated (150 cycles) TiO_2 nanowires has other facets exposed in addition to the (110) surface, which is the exposed side facet of the bare TiO_2 nanowires. Reports show that rutile TiO_2 shows some crystal facet dependence on photocatalytic activity [34-35] due to a disparity in hole reactivity on different surfaces. Therefore, it is possible that the activity of core/shell nanowires can be affected by the mixture of different crystal facets. These synergistic effects show that ALD coating could contribute to an increase in charge collection efficiency.

Finally, we previously discussed that the IPCE of longer TiO_2 nanowires decreases at shorter wavelengths due to charge collection losses (Figure 2.4a). The photocurrent results show that the longer nanowire arrays are affected the most by charge collection losses but have the highest enhancement factors (Figure 2.10) from ALD coating. These results along with the increase in IPCE suggest that ALD coating can increase the charge collection efficiency for nanowires. The enhancement factor is decreased for shorter nanowire arrays because the increase in IPCE is observed at shorter wavelengths, which represent only a small fraction of sunlight.

2.6 Conclusion

This chapter demonstrates that the water splitting activity of TiO_2 nanowire arrays depends on their length and surface properties. Photocurrent measurements showed a non linear increase in photocurrent with nanowire length and approached saturation with a length of 1.8 μm. The IPCE of TiO_2 nanowires increased linearly vs $1-10^{-\alpha \times Length}$ with near bandgap illumination (λ = 410 nm) due to an increase in the absorption of light (η_{e^-/h^+}). However, the IPCE decreases significantly at shorter wavelengths for longer nanowires because of poor charge collection efficiency. To improve charge collection efficiency, a TiO_2 ALD layer was deposited on the TiO_2 nanowire arrays. The ALD shell showed different phases from amorphous, to epitaxial rutile, to polycrystalline anatase TiO_2 depending on thickness of the shell. Amorphous and anatase TiO_2 shells decreased the photocurrent when compared to as made nanowires. However, epitaxial grains of rutile shells showed a photocurrent enhancement of 1.5 times demonstrating the importance of the interface between the core and shell. By comparing optical and IPCE measurements, we determined that the ALD shell does not influence on the absorption of light significantly.

We suggest that the large enhancement is due to improved charge collection efficiency from passivation of defect sites and an increase in surface area. These results show that the geometric and surface properties of semiconductors must be considered to achieve high water splitting efficiency since these properties can affect all of the processes that affect the EQE (photon absorptance, charge transport, and charge separation) during PEC reactions.

References

[1] Walter, M. G.; Warren, E. L.; Mckone, J. R.; Boettcher, S.W.; Santori, E. A.; Lewis, N. S. *Chem. Rev.* **2010,** *110*, 6446–6473.

[2] Fukishima, A.; Honda, K. *Nature* **1972**, 238, 37-38.

[3] Nozik, A. J. *Nature* **1975**, 257, 384-386.

[4] Nowotny, J.; Sorrell, C. C.; Sheppard, L. R.; Bak, T. *Int. J. Hydrogen Energy* **2005**, 30, 521-544.

[5] Ni, M.; Leung, M. K.; Leung, D. Y.; Sumathy, K. *Renew. Sust. Energy. Rev.* **2007**, 11, 401-425.

[6] Linsebigler, A. L.; Lu, G.; Yates, J. T. *Chem. Rev.* **1995**, 95, 735-758.

[7] Hendry, E.; Koeberg, M.; O'Regan, B.; Bonn, M. *Nano. Lett.* **2006**, 6, 755-759.

[8] Salvador, P. *J. Appl. Phys.* **1984**, 55, 2977-2985.

[9] Zhu, J.; Zäch, M. *Curr. Opin. Colloid Interface Sci.* **2009**, 14, 260-269.

[10] Liu, G.; Sun, C.; Yang, H. G.; Smith, S. C.; Wang, L.; Lu, G. Q.; Cheng, H. M. *Chem. Commun*. **2010**, 46, 755–757

[11] Yu, J.; Zhang, L.; Cheng, B.; Su, Y. *J. Phys. Chem. C.* **2007**, 111, 10582-10589

[12] Shi, J.; Hara, Y.; Sun, C.; Anderson, M. A.; Wang, X. *Nano. Lett.* **2011**, 11, 3413-3419.

[13] Liu, M.; Snapp, N.; Park, H. *Chem. Sci.* **2011**, 2, 80-87.

[14] Khan, S. U.; Sultana, T. *Sol. Energy Mat. Sol. Cells* **2003**, 76, 211-221.

[15] Feng, X.; Shankar, K.; Varghese, O. K.; Paulose, M.; Latempa, T. J.; Grimes, C. A. *Nano. Lett.* **2008**, 8, 3781-3786.

[16] Shankar, K.; Basham, J. I.; Allam, N. K.; Varghese, O. K.; Mor, G. K.; Feng, X.; Paulose, M.; Seabold, J. A.; Choi, K. S.; Grimes, C. A. *J. Phys. Chem. C.* **2009**. *113*. 6327-6359.

[17] Cho, I. S.; Chen, Z.; Forman, A. J.; Kim, D. R.; Rao, P. M.; Jaramillo, T. F.; Zheng, X. *Nano. Lett.* **2011**, 11, 4978-4984.

[18] Law, M.; Greene, L. E.; Radenovic, A.; Kuykendall, T.; Liphardt, J.; Yang, P. *J. Phys. Chem. B* **2006**, 110, 22652-2266.

[19] Schmidt, J.; Merkle, A.; Hoex, B.; van de Sanden, M. C. M.; Kessels, W. M. M.; Brendel, R. *Photovoltaic Specialists Conference, IEEE* **2008** , 10.1109/PVSC.2008.4922636

[20] Formal, F. L.; Tétreault, N.; Cornuz, M.; Moehl, T.; Grätzel, M.; Sivula, K. *Chem. Sci.* **2011**, 2, 737-743.

[21] Paracchino, A.; Laporte, V.; Sivula, K.; Grätzel, M.; Thimsen, E. *Nat. Mater.* **2011**, 10, 456-461.

[22] Hwang, Y. J.; Boukai, A.; Yang, P. *Nano. Lett.* **2009**, 9 , 410-415.

[23] Liu, B.; Aydil, E. S. *J. Am.Chem. Soc.* **2009**, 131, 3985-3990.

[24] Dutoit, E. C.; Cardon, F.; Gomes, W. P. *Ber. Bunsenge. Phys. Chem.* **1976**, 80, 475-481.

[25] Chen, Z. B.; Jaramillo, T. F.; Deutsch, T. G.; Kleiman-Shwarsctein, A.; Forman, A. J.; Gaillard, N.; Garland, R.; Takanabe, K.; Heske, C.; Sunkara, M.; McFarland, E. W.; Domen, K.; Miller, E. L.; Turner, J. A.; Dinh, H. N. J. *J. Mater. Res.* **2010**, 25, 3-16.

[26] Persson, C.; Silva, A. F. *Appl. Phys. Lett.* **2005**, 86, 231912.

[27] Thomazi, F.; Roman, L. S.; Silva, A. F.; Persson, C. *Phys. Status Solidi C* **2009**, 6, 2740-2742.

[28] Reichman, J. *Appl. Phys. Lett.* **1981**, 38, 251-253.

[29] Cheng, H. E.; Hsu, C. M.; Chen, Y. C. *J. Electrochem. Soc.* **2009**, 156, D275-D278

[30] Ma, H. L.; Yang, J. Y.; Dai, Y.; Zhang, Y. B.; Lu, B.; Ma, G. H. *Appl. Surf. Sci.* **2007**, 253, 7497-7500

[31] Gerischer, H. *Solar Energy Conversion*; Springer Berlin: Heidelberg, 1979; p115-172.

[32] Radecka, M.; Rekas, M.; Trenczek-Zajac, A.; Zakrzewska, K. *J. Power Sources* **2008**, 181, 46-55

[33] van der Meulen, T.; Mattson, A.; Österlund, L. *J. Catal.* **2007**, 251, 131-144

[34] Nakamura, R.; Ohashi, N.; Imanishi, A.; Osawa, T.; Matsumoto, Y.; Koinuma, H.; Nakato, Y. *J. Phys. Chem. B.* **2005**, 109, 1648-1651.

[35] Wilson, J. N.; Idriss, H. *J. Am. Chem. Soc.* **2002**, 124, 11284-11285.

Chapter 3

High Density n-Si/n-TiO_2 Core/Shell Nanowire Arrays with Enhanced Photoactivity

3.1 Introduction

Direct solar energy conversion to storable fuels such as hydrogen offers a promising route towards less reliance on fossil fuels.[1-4] For example, photoelectrolysis of water to generate H_2 on a semiconductor/electrolyte interface has the attractive advantages of clean processing and energy savings over steam reforming of natural gas. One of the most critical issues in solar water splitting is the development of a photoanode with high efficiency and long term durability in an aqueous environment. TiO_2 has been extensively studied as a photoanode due to its high resistance to photocorrosion.[5-10] However, its conversion efficiency of solar energy to hydrogen is still low (less than 4 %) [6] due to its wide bandgap (E_g = 3.0 ~3.2 eV). TiO_2 requires an external bias to reduce water for H_2 production to overcome the chemical over potential.[5, 11] Si (E_g = 1.12 eV), on the other hand, can absorb sunlight efficiently. It is however challenging to use Si for photoelectrolysis since it readily corrodes in water. Moreover, it is thermodynamically impossible for Si to oxidize water

spontaneously due to its high valence band maximum (VBM) energy. Therefore, a composite semiconductor electrode composed of a semiconductor heterojunction has been proposed to compensate these shortcomings. In these cases, the photoanode is composed of a small band gap semiconductor that is protected by a stable semiconductor.[12-14]

Semiconductor heterojunctions can absorb different region of the solar spectrum.[15-18] The advantage of composite structures is that each semiconductor need to satisfy one energetic requirement: matching the conduction band minimum (CBM) or VBM with either the H_2 reduction or O_2 oxidation potential. Single semiconductor materials typically cannot satisfy the requirements of suitable bandgap energies for efficient solar absorption and meantime with band-edges aligned with both the H_2 and O_2 redox potential of water.[3,19] Here, we prepared TiO_2 coated Si nanowire arrays and studied their photo-oxidative properties. We observed that Si/TiO_2 core/shell nanowire arrays showed higher photocurrent than the planar Si/TiO_2. A semiconductor heterojunction of n-Si/n-TiO_2 or p-Si/n-TiO_2 has different band bending properties near the junction.[12,20] The n/n heterojunction has a potential energy barrier between the two semiconductor regions that reflects minority holes in the TiO_2 similar to the back surface field in solar cell.[21] Using photocurrent and open circuit voltage measurements, we show that the n/n heterojunction is more promising for photoelectrochemical (PEC) cell application.

3.2 Synthesis of Si/TiO_2 Nanowire Arrays

3.2.1 Synthesis of Electroless Etched Si Nanowire Arrays

Highly oriented Si nanowire arrays on the silicon wafers were synthesized by an aqueous electroless etching method.[22] These Si nanowire arrays significantly suppress reflection which has the potential to provide a higher efficiency of PEC cell. We prepared n-type and p-type Si electroless etched nanowire (EENW) arrays from n-Si(100) (Phosphorus doped, resistivity of 0.6~0.8 Ωcm) and p-Si(100) (Boron doped, resistivity of 1~5 Ωcm) wafers with dopant concentrations of ~10^{16} cm^{-3}. A silicon wafer was ultrasonicated in acetone and isopropanol for 10 min, respectively, and rinsed with isopropanol and deionized (DI) water. The clean silicon wafer was immersed into the aqueous etching solution containing 0.04 M $AgNO_3$ (99.999%, Aldrich) and 5M HF (49%, Honeywell) at room temperature. The length of the EENW was controlled by the etching time (0.2 μm/min growth rate).

3.2.2 Atomic Layer Deposition of TiO_2 Shell

TiO_2 was grown both on the Si EENW arrays and the planar Si wafer by a home-built atomic layer deposition (ALD) system with $TiCl_4$ (99.990%, Alfa) and pure DI water as the precursors. Si samples were cleaned with a 10: 1 buffered HF solution to remove the

native oxide layer right before loading into the ALD vacuum chamber. The ALD system deposits polycrystalline anatase TiO_2 layer with an average growth rate of 1.2 Å per cycle on the planar Si wafer and 0.7 Å per cycle on our Si EENW arrays at 300 °C. The thickness of the TiO2 film was monitored by ellipsometry for the planar sample and by transmission electron microscope (TEM) for the nanowire sample. On the Si EENW array, diffusion of the gas precursors is reduced due to the high density of the nanowire arrays, which leads to slower growth rate than the planar substrate. Care was taken to ensure that the TiO_2 thickness on the EENW arrays and planar substrates were equivalent.

3.2.3 Characterization of Si EENW/TiO_2

Typical cross sectional scanning electron microscope (SEM) and TEM images of Si EENW and the ALD TiO_2 coated Si EENW (Si EENW/TiO_2) are shown in Figure 3.1a-d. The Si EENW and Si EENW/TiO_2 arrays are produced vertically on the Si wafer with high density. Si EENW maintains the same crystallinity as the starting Si wafer,[22] and their diameters are in the range of 20 ~ 200 nm. Figure 3.1d shows polycrystalline TiO_2 deposition on the EENW. Figure 3.1e and f show the top view SEM images of Si EENW/TiO_2 arrays and TiO_2 thin film on the Si(100) wafer with average thickness of 35 nm. The nanocrystalline nature of the TiO_2 coating is similar for deposition on the nanowire surface and on the flat wafer surface.

The X-ray diffraction (XRD) characterization indicates that the ALD grown TiO_2 layer has an anatase structure both on the Si(100) wafer and on the Si EENW array, as shown in Figure 3.2. For photoelectrolysis of water, anatase TiO_2 has been reported to have an advantage of a flat band potential (U_{fb}) that is 200 mV more negative than that of the rutile TiO_2 (E_g = 3.0 eV). This allows anatase TiO_2 (E_g = 3.2 eV) to have sufficient cathodic potential for hydrogen reduction from water unlike rutile TiO_2.[23]

The carrier concentration (N_D) of TiO_2 layer by ALD was determined by capacitance versus voltage measurement. 90 nm TiO_2 thin film was deposited on the highly doped n-Si wafer (Arsenic doped, 0.001~0.004 Ωcm), and Ni was deposited on the TiO_2 thin film to form Schottky barrier between TiO_2 and Ni junction. From the Mott-Schottky relation, N_D was found to be 2.76 x 10^{17} cm^{-3}. The TiO_2 becomes n-type semiconductor because of defects such as oxygen vacancies and titanium interstitials, and their carrier concentrations have been reported to vary from ~$10^{17}cm^{-3}$ to ~10^{20} cm^{-3} depending on synthesis and post growth treatment. [24-26]

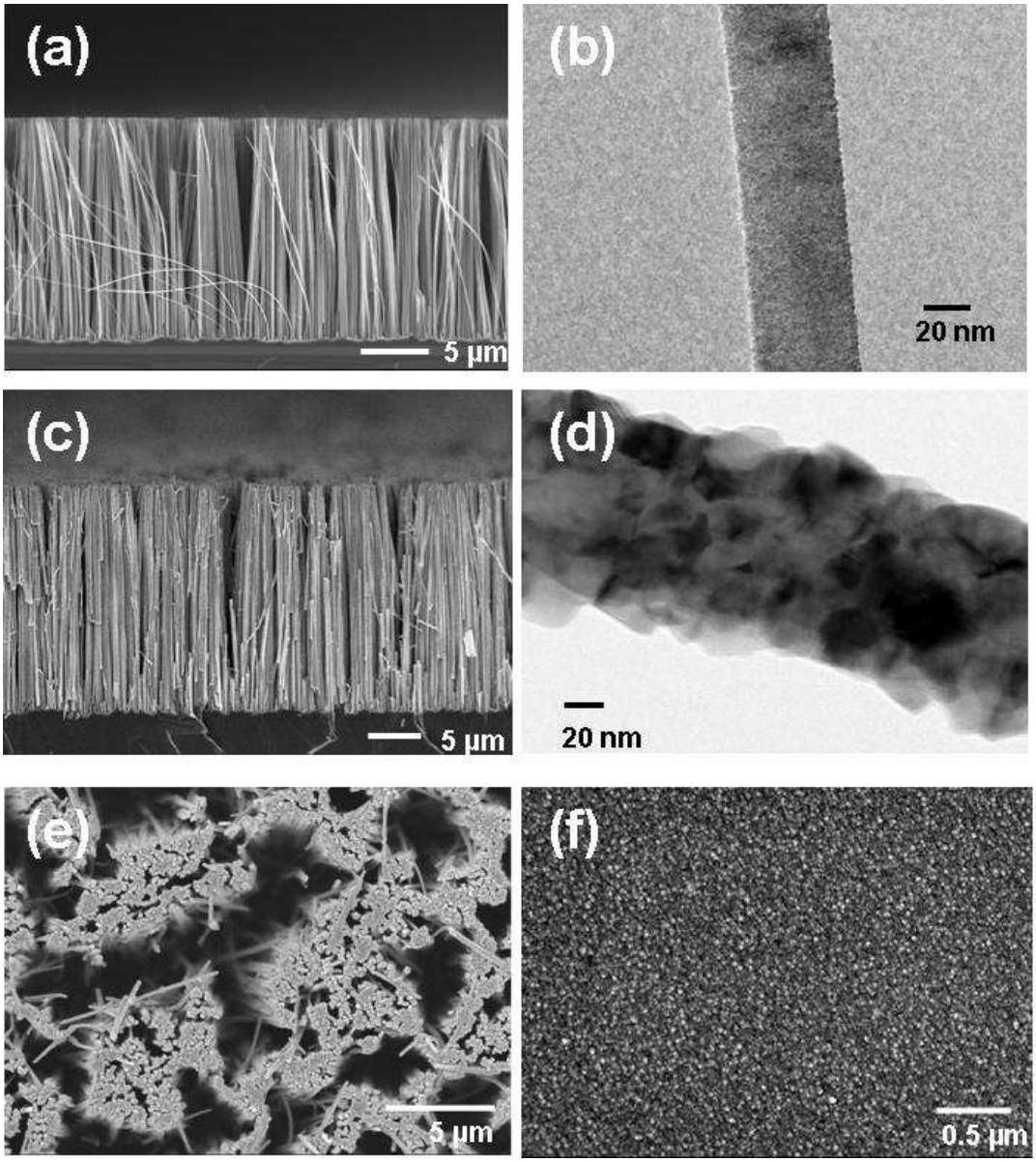

Figure 3.1. Characterization of Si EENW and Si/TiO_2 core/shell structures. (a) Cross sectional SEM of 20 µm long Si EENW arrays, demonstrating vertical alignment and high density. (b) Typical TEM image of a Si EENW. (c) Cross sectional SEM images of Si EENW arrays coated with TiO_2 by ALD at 300 ^{o}C. (d) Typical TEM image of Si EENW/TiO_2 core/shell nanowire, showing that polycrystalline TiO_2 covers the Si EENW. (e) Top view SEM images of Si EENW/TiO_2 array. (f) Top view SEM image an ALD grown TiO_2 thin film on a Si wafer, showing nanometer size grains of TiO_2.

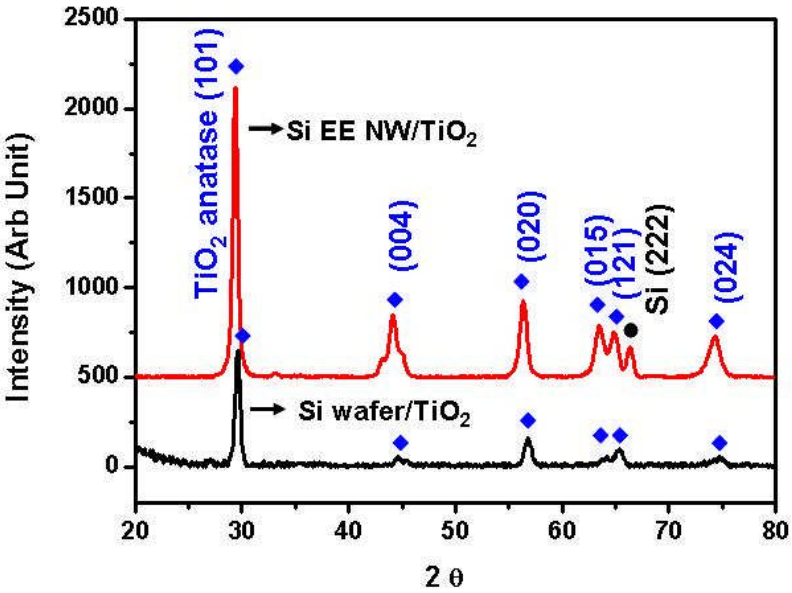

Figure 3.2. X-ray diffraction pattern of TiO_2 layer grown by ALD at 300 ^oC. 25~40 nm TiO_2 deposited on Si EENW arrays (red line), 35 nm TiO_2 thin film on a Si planar substrate (black line). Both TiO_2 layers index to polycrystalline anatase.

3.3 Photoanodic Properties with Si/TiO_2 Heterojunction

3.3.1 Photocurrents with Si EENW/TiO_2 Photoanode

Photocurrent measurements were performed in a 1M KOH electrolyte with three electrodes configuration (EG&E Pinceton Applied Research Potentiostat, VersaStat II): Si/TiO_2 photoanode as a working electrode, Pt gauze as a counter electrode, and a saturated calomel electrode (SCE, Pine Research Instrumentations, AFREF1) as a reference electrode. All three electrodes are in a glass cell which has a 1 inch quartz window, and Ar gas was bubbled through to remove the dissolved oxygen during the measurement. The current versus potential measurements were carried out at a 10 mV/s sweep rate. A constant light intensity of 100 mW/cm^2 from a 450 W Xe lamp (Oriel, 6266) illuminated our samples, and a liquid filter (Oriel, 6123NS) was used to avoid solution heating by infrared light.

Figure 3.3 shows the photocurrent versus bias potential characteristics for Si/TiO_2 composite photoanodes. Under illumination, oxidation of water takes place on the photoanode.

$$4OH^- + 4h^+ \rightarrow 2H_2O + O_2 \qquad E^o = +0.160\,V\,(vs\ SCE)$$

The photocurrent versus bias potential curves have three regions: low photocurrent density region at negative bias potential (region I), plateau of the photocurrent density at more positive bias potential (region III), and increasing photocurrent density region (region II) between regions I and III. No photocurrent passes through the semiconductor and electrolyte interface when the negative bias voltage is close to the flat band potential because any created excess holes and electrons are recombined before holes transfer into the electrolyte (region I).[27] The photocurrent plateau appears as the bias potential sweeps to more positive direction (region III), where the photocurrent is limited by the number of the holes excited by illumination.

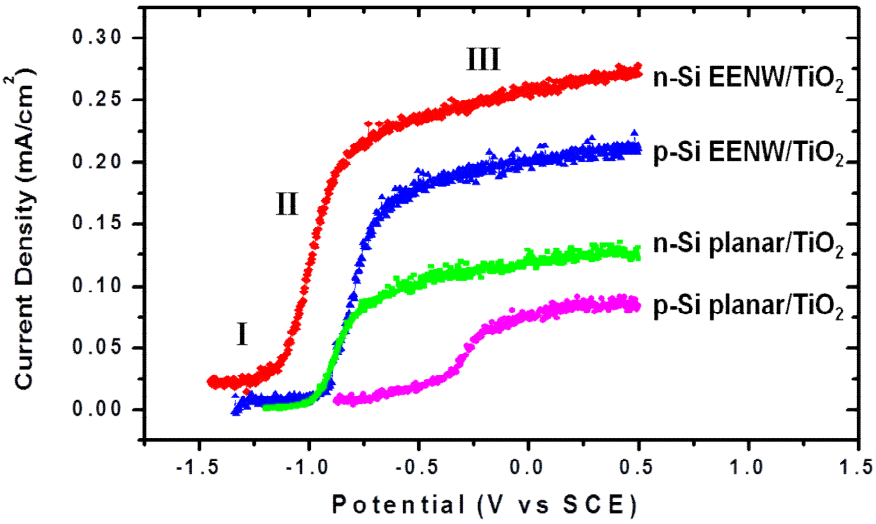

Figure 3.3. Photocurrent density versus bias potential (vs SCE) of Si/TiO_2 photoanodes: n-Si EENW array coated by TiO_2 (red), p-Si EENW array coated by TiO_2 (blue), n-Si(100) planar substrate coated by TiO_2 (green), p-Si(100) planar substrate coated by TiO_2 (purple).

Our planar Si/TiO_2 samples show comparable photocurrent density to those reported in the literature. The reported value [9] for a 15 µm thick film of P-25 TiO_2 on Ti foil is 0.1 mA/cm^2 under the same illumination conditions (Xe lamp, 100 mW/cm^2) even though the thickness of our ALD grown TiO_2 film is only 35 nm. At region III, 20 µm long Si EENW/TiO_2 samples show 2.5 times higher photocurrent density than planar Si/TiO_2

samples for both n-type and p-type Si. The Si EENW/TiO_2 composites have higher photocurrent mainly because of lower reflectance and larger surface area than the Si planar/TiO_2.

3.3.2 n-Si/n-TiO_2 versus p-Si/n-TiO_2 Heterojunction

Figure 3.3 also shows that n-Si/n-TiO_2 composites have 20~25 % higher photocurrent density and more negative onset potential than those of p-Si/n-TiO_2 for both nanowire and planar structures. Higher photocurrent is expected for the n/n junction since band bending at the junction helps charge separation. The band bending of the semiconductors at the junctions were shown in Figure 3.4. The Fermi energy (E_F) of our n and p type silicon are -4.25 eV, and -4.97 eV (relative to the vacuum level), respectively. E_F of TiO_2 was calculated [28-29] from the reported electron effective mass in anatase ($m_e^* = 1m_e$)[30] and the measured carrier concentration (N_D = 2.76 x 10^{17} cm^{-3}). Figure 3.4 illustrates the charge flow in n-Si/n-TiO_2 junctions under illumination. The e^- / h^+ pairs are created inside both the Si and TiO_2 because the TiO_2 shell is transparent under visible light. Visible light can be harvested by the core Si. Under the illumination, Fermi energies of the electrons and holes, so-called quasi-Fermi energies (E_F^*), differ from E_F in dark.[19] The quasi Fermi energies of minority holes ($_pE_F^*$) in the n-Si and n-TiO_2 are shown. The photogenerated hole in TiO_2 ($_{TiO_2}h^+$) moves toward the n-TiO_2/electrolyte interface and oxidizes OH^- to oxygen, while photogenerated electrons in the n-TiO2 ($_{TiO_2}e^-$) move away from the front surface due to the Schottky barrier at the interface with the electrolyte.

In addition to this charge separation, the interface between the n-Si and n-TiO_2 reduces the loss of holes in the TiO_2 region which results in an increase of the photoanodic current. The potential barrier seen by the holes at the n-Si/n-TiO_2 junction reflects holes back into the TiO_2 layer (Figure 3.4a). This is analogous to the back surface field of a solar cell which has shown larger photocurrent and larger output voltage by adding a heavily doped region adjacent to the contact.[31] To complete the circuit, the photogenerated electrons in the n-Si ($_{Si}e^-$) move to the counter electrode where the reduction reaction takes place. The photogenerated hole in n-Si ($_{Si}h^+$) moves toward the n-Si/n-TiO_2 junction and recombines with $_{TiO_2}e^-$. Therefore, n-Si/n-TiO_2 core/shell structure shows the largest increase in photocurrent since its band alignment at the junction helps reduce recombination under illumination. In the case of p-Si/n-TiO_2 junctions, the flow of electrons and holes at the junction of p-Si/n-TiO_2 is opposite to the desirable direction. Figure 3.4b shows that $_{TiO_2}h^+$ can move either to the electrolyte or to the p-Si in p/n

junction. The p-Si/n-TiO_2 junction, therefore, has smaller observed photo-anodic current density than n-Si/n-TiO_2.

3.3.3 Open Circuit Potential Enhancement with n-Si/n-TiO_2

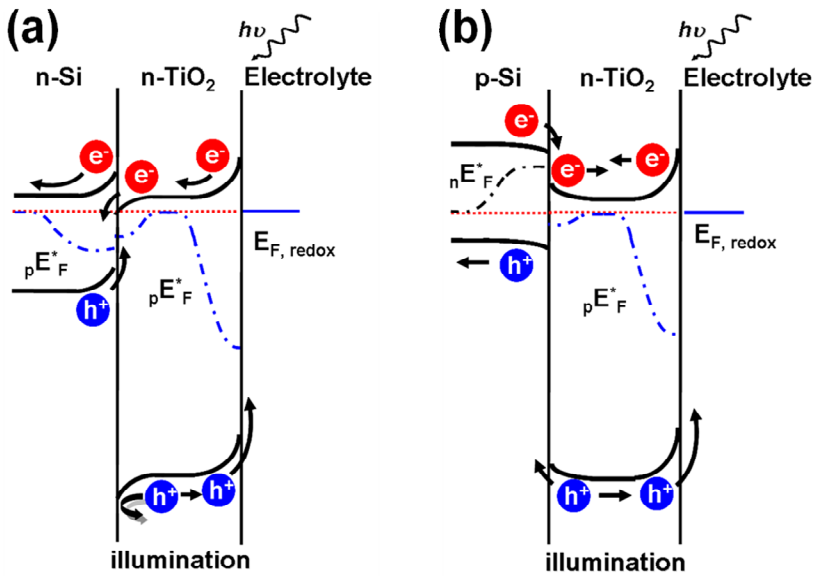

Figure 3.4. Schematic representation of band energies and charge transfer (a) for n-Si/n-TiO_2 and (b) for p-Si/n-TiO_2 under the illumination.

The larger photocurrent in the n-Si/n-TiO_2 leads to a larger negative onset potential. This is a result of the n/n junction's effective charge separation that leads to a larger short circuit current (J_{sc}).[31] Both n-Si EENW/TiO_2 and p-Si EENW/TiO_2 have similar dark current values (5μA/cm^2). Also, higher V_{oc} is expected for n-Si/n-TiO_2 since the E_F and band energies of the n-Si and n-TiO_2 shift upward at open circuit under the illumination. The V_{oc} of n-Si/n-TiO_2 photoanode is $V_{oc} = V_{oc}\ (TiO_2 / electrolyte) + V_{oc}\ (Si / TiO_2)$.[20] For the p-Si/n-$TiO_2$, the band energies of the n-TiO_2 shift upward but the band energies of the p-Si shift downward. The photovoltage at the p-Si/n-TiO_2 junction is in the opposite direction to the photovoltage at the n-TiO_2/electrolyte interface due to the downward band bending. The V_{oc} of p-Si/n-TiO_2 photoanode is $V_{oc} = V_{oc}\ (TiO_2 / electrolyte) - V_{oc}\ (Si / TiO_2)$.

We can take the advantage of the higher V_{oc} of the n/n junction for the PEC cell. Enhanced J_{sc} and V_{oc} will provide a higher efficiency PEC cell. Also, for the solar water splitting, larger V_{oc} provides high enough cathodic potential to reduce the water to

hydrogen. It is important that the flat band potential of the semiconductor is lower than the hydrogen reduction potential. For example, Fe_2O_3 (E_g = 2.1 eV) and WO_3 (E_g = 2.6 eV) have been studied due to higher stability and lower band gap than TiO_2. However, both need an external bias voltage to complete the water splitting since their CBMs are lower than hydrogen reduction potential by 0.2 V and 0.1V.[6] Therefore, the n/n composites have the potential for the spontaneous photoelectrolysis of water.

3.4 Nanowire Length Dependence

Figure 3.5 demonstrates the photocurrent density depending on the length of the n-Si EENW/TiO_2 arrays. We prepared 5 µm, 10µm, and 20µm long n-type Si EENW/TiO_2 arrays and planar n-Si/TiO_2. We observed that the longer Si EENW/TiO_2 arrays have higher photocurrent although the photocurrent density normalized by the length of the nanowires decrease as shown in Figure 3.5b.

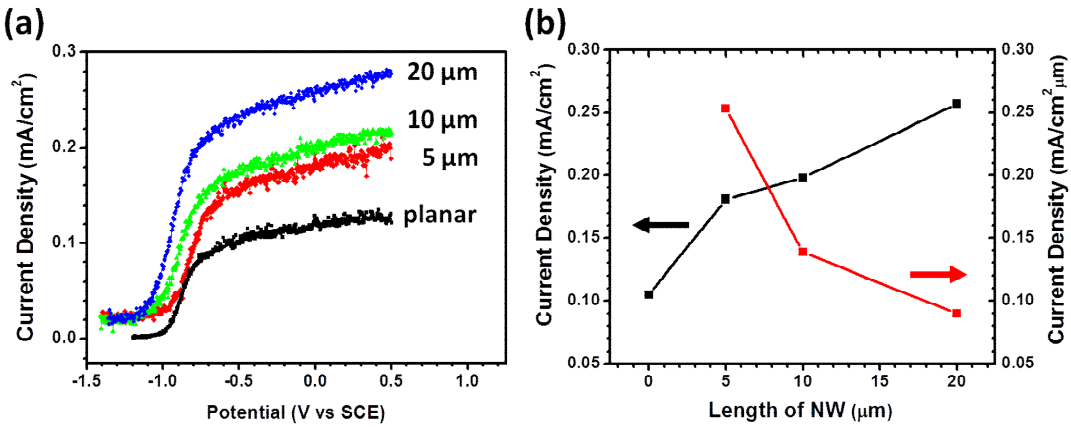

Figure 3.5. (a) Variation of photocurrent density versus potential depending on the length of n-Si EENW/TiO_2 arrays: 20 µm (blue line), 10 µm (green line), 5 µm (red line) long NW arrays and n-Si planar/TiO_2 (black line). (b) Relationship between photocurrent density versus the length of n-Si EENW/TiO_2, illustrating longer wire arrays have higher photocurrent. The axis to the right is the current density normalized by the length of the nanowire.

The reflectance of the Si/TiO_2 core/shell nanowrie arrays with various length were measured in the range of 200~900 nm when the reflectance of the Si planar/TiO_2 structure was taken as background. Figure 3.6 shows that all of the three different length of Si EENW/TiO_2 arrays had significantly lower reflectance than Si planar/TiO_2 sample. The Si EENW/TiO_2 sample can effectively trap the light by extending the path length due to multiple reflection in a high density array structures similar to textured surfaces.[32] When the wires are 5 ~ 20µm long, their reflectance values are nearly the same. All of the three different length Si EENW/TiO_2 arrays have about 1~2 % of reflectance in the UV region

(200~350 nm), and about 5 % of reflectance in the visible region (450 ~900 nm). In addition to low reflectance, the high surface area of Si EENW is also expected to contribute the higher photocurrent since it increases the interface area with the electrolyte as well as the overall amount of TiO_2. Lower reflectance and higher surface area of the Si EENW/TiO_2 contribute to higher absorption and higher photocurrent density than the planar samples.

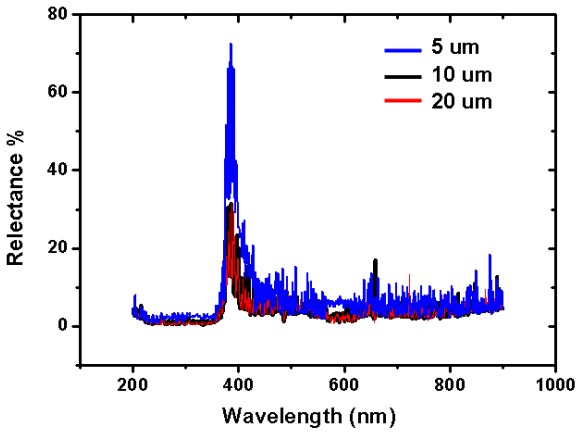

Figure 3.6. Reflectance (%) versus wavelength for the three different length of n-Si EENW/TiO_2 in the range of 200 ~ 900 nm when blank is n-Si planar/TiO_2 sample. Less than 5 % reflectance for all three n-Si EENW/TiO_2 samples except near the TiO_2 band gap (~380 nm). 5 µm ~ 20 µm long Si EENW/TiO_2 arrays have almost same reflectance which means the reflectance does not vary much depending on the nanowire length except near 380 nm.

3.5 Enhanced Stability with TiO_2 Shell

Stability is another important requirement for the PEC cell. We measured the photocurrent density versus elapsed time under the Xe lamp illumination (100 mW/cm^2) at zero bias potential (vs SCE) with both of the n-Si/n-TiO_2 and p-Si/n-TiO_2 core/shell nanowire photoanodes. The n and p type Si EENW/TiO_2 core/shell structures have shown constant photocurrent levels while testing for one hour as shown in Figure 3.7. By coating the Si with TiO_2, we can make the photoanode stable in the 1M KOH aqueous solution. In contrast, planar Si wafers and Si EENW arrays generate vigorous H_2(g) bubbles in the KOH electrolyte and as a result they are etched.

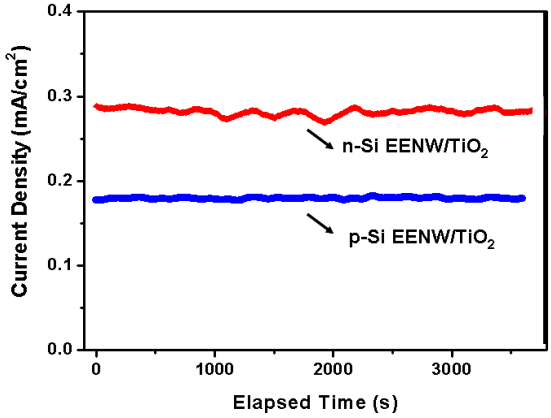

Figure 3.7. Photocurrent density versus elapsed time for n-Si EENW/TiO_2 and p-Si EENW/TiO_2 core/shell nanowire arrays. Both of the samples have stable photocurrent for an hour in 1M KOH electrolyte.

3.6 Visible Light Illumination

In order to ascertain the contribution of the core Si, we measured the photocurrent and V_{oc} of the Si/TiO_2 photoanodes under the visible light illumination. The light was passed through a 441.6 nm edge filter to cut off the UV region from the Xe lamp so that carriers are generated only in the Si due to the wide band gap of TiO_2 (3.2 eV). No photocurrents was observed under the visible light with both of n-Si/n-TiO_2 and p-Si/n-TiO_2 composites as shown in Figure 3.8. This is consistent with the schematic diagram of

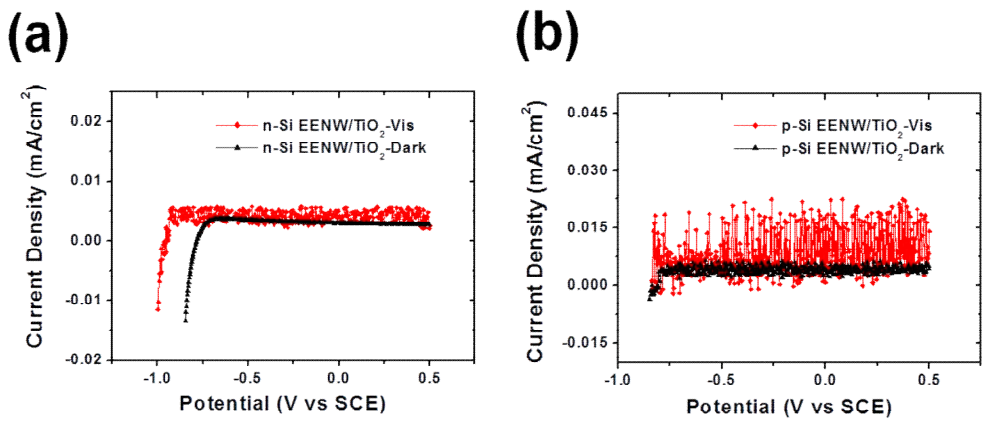

Figure 3.8. Current density comparison in dark and under visible light illumination ($\lambda >$ 441.6 nm) with (a) n-Si EENW/TiO_2, and (b) p-Si EENW/TiO_2.

the band bending under visible light (Figure 3.9a and b). Photogenerated holes in Si cannot be transferred to the valence band of TiO_2 since the valence band maximum of Si is located on higher potential, so there is a significant barrier for the hole at the junction. Instead of transferring holes to TiO_2 shell, the photogenerated e^- / h^+ pairs in Si recombine at steady state, and there is no net charge flux.[19, 33] Therefore, photo-oxidation cannot take place at the TiO_2 surface unless carriers are photogenerated in the TiO_2 shell.

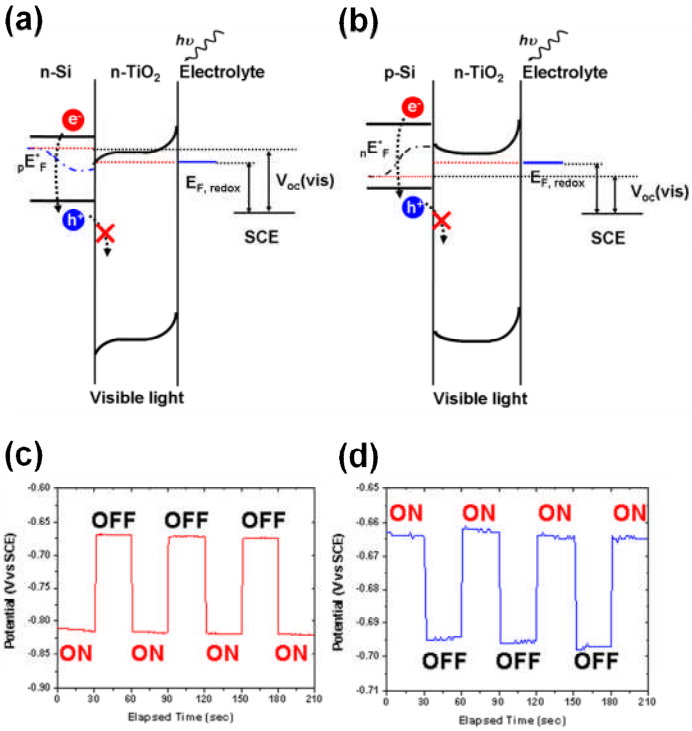

Figure 3.9. Schematic diagram of band bending and V_{oc} for (a) n-Si/n-TiO_2 and (b) p-Si /n-TiO_2 under visible light illumination, and open circuit voltage (V_{oc}) versus elapsed time for (c) n-Si EENW/TiO_2 and (d) p-Si EENW/TiO_2 arrays under visible light illumination (ON) and in dark (OFF).

Figure 3.9 shows that the V_{oc} shifts under visible light illumination: n-Si EENW/TiO_2 increase the V_{oc} while the p-Si EENW/TiO_2 decrease the V_{oc}. For n-Si/n-TiO_2, the photogenerated holes in the Si move toward the TiO_2 and recombine with electrons in TiO_2 due to an electric field in space charge region. The charge separation shifts the E_F and the band energies of the n-Si upward, so that the space charge region diminishes. When flat band is attained, there will be no more charge separation. Therefore, the V_{oc} of the n-Si/n-TiO_2 photoanode becomes more negative (Figure 3.9c). For p-Si/n-TiO_2, the band bending of the p-Si diminishes similar to n-Si/n-TiO_2, but the reduced band

bending shifts the band energies of p-Si downward which reduces the V_{oc} under visible light (Figure 3.9d). From the change of the V_{oc} under visible light, we confirmed that the core Si absorbs the visible light and it contributes shift of the band energies but not the photocurrents.

3.7 Conclusion

This chapter compares the photocurrent density of the planar Si and Si EENW coated by ALD TiO_2 thin film. The Si EENW/TiO_2 has 2.5 times higher photocurrent density than the planar Si/TiO_2 due to lower reflectance and higher surface area. We also observed an increase of the photocurrent by using n-Si/n-TiO_2 heterojunctions because n/n junctions enhance the charge separation and minimize recombination. The n/n heterojunction is a promising structure for solar water splitting since the photovoltage at the junction can compensate the lower energy level of the conduction band of the shell semiconductor. Also, the n/n heterojunction could potentially increase the efficiency of the photovoltaic cell due to a higher open circuit voltage and higher photocurrent.

This section first appeared in Nano Letters:

Hwang, Y. J.; Boukai, A.; Yang, P. "High Density n-Si/n-TiO_2 Core/Shell Nanowire Arrays with Enhanced Photoactivity" *Nano. Lett.* **2009**, *9*, 410-415.

References

[1] Lewis, N. S.; Nocera, D. G. *Proc. Natl. Acad. Sci. USA* **2006**, *103*, 15729.

[2] Sanderson, K. *Nature* **2008**, *452*, 400.

[3] Grätzel, M. *Nature* **2001**, *414*, 338.

[4] Nowotny, J.; Sorrell, C. C.; Sheppard, L. R.; Bak, T. *Int. J. Hydrogen. Energy* **2005**, *30*, 521.

[5] Fujishima, A.; Honda, K. *Nature* **1972**, *238*, 37.

[6] Rajeshwar, K. *J. Appl. Electrochem.* **2007**, *37*, 765.

[7] Ni, M.; Leung, M.K.; Leung, D. Y.; Sumathy, K. *Renewable & Sustainable Energy Reviews* **2007**, *11*, 461.

[8] Kitano, M.; Matsuoka, M.; Ueshima, M.; Anpo, M. *Appl. Catalysis A* **2007**, *325*, 1.

[9] Park, J. H.; Kim, S.; Bard, A. J. *Nano. Lett.* **2005**, *6*, 24.

[10] Kongkanad, A.; Dominguez, R. M.; Kamat, P.V *Nano. Lett.* **2007**, *7*, 676.

[11] Kavan, L.; Grätzel, M.; Gilbert, S.E.; Klemenz, C.; Scheel, H. J. *J. Am. Chem. Soc.*. **1996**, *118*, 6716.

[12] Takabayashi, S.; Nakamura, R.; Nakato, Y. *J. Photochem. Photobiol. A* **2004**, *166*, 107.

[13] Morisaki, H.; Watanabe, T.; Iwase, M.; Yazawa, K. *Appl. Phys. Lett.* **1976**, *29*, 338.

[14] Lin, C. Y.; Fang, Y. K.; Kuo, C. H.; Chen, S. F.; Lin, C.; Chou, T. H.; Lee, Y.; Lin, J.; Hwang, S. *Appl. Surf. Sci.* **2006**, *253*, 898.

[15] Khaselev, O.; Turner, J. A. *Science* **1998**, *280*, 425.

[16] Yin, Y.; Jin, Z.; Hou, F. *Nanotechnology* **2007**, *18*, 495608.

[17] Yu, Z. G.; Pryor, C. E.; Lau, W. H.; Berding, M. A.; MacQueen, D. B. *J. Phys. Chem. B.* **2005**, *109*, 22913.

[18] Mor, G. K.; Vargnese, O. K.; Wilke, R. H.; Sharma, S.; Shankar, K.; Latempa, T.; Choi, K.; Grimes, C. A. *Nano. Lett.* **2008**, *8*, 3555.

[19] Gerischer, H. *Solar Energy Conversion*; Springer Berlin: Heidelberg, 1979; p115-172.

[20] Wagner, S.; Shay, J. L.; *Appl. Phys. Lett.* **1977,** *31*, 446.

[21] Hovel, H. J.; Woodall, J. M.; *J. Electrochem. Soc.* **1973**, *120*, 1246.

[22] Peng, K. Q.; Xu, Y.; Wu, Y.; Yan, Y. J.; Lee, S. T.; Zhu, J. *Small* **2005**, *1*, 1062.

[23] Radecka, M.; Rekas, M.; Trenczeck-Zajac, A.; Zakrzewska, K. *J. Power. Sources.* **2008**, *181*, 46.

[24] Mahajan, V. K.; Misra, M.; Raja, K. S.; Mohapatra, S.K.; *J. Phys. D: Appl. Phys.* **2008**, *41*, 125307.

[25] Akiknsa, Jun.; Khan, S. U.; *Int. J. Hydrogen. Energy.* **1997,** *22*, 875.

[26] Cheng, H.; Lee, W.; Hsu, C.; Hon, M.; Huang, C. *Electrochem. Solid-State. Lett.* **2008**, *11*, D81.

[27] Bard, A. J.; Faulkner, L. R. *Electrochemical Methods: Fundamentals and Applications*; John Wiley & Sons, Inc.: New York, 1980; p637.

[28] Bak, T.; Nowotny, J.; Rekas, M.; Sorrell, C. C. *Int. J. Hydrogen. Energy* **2002**, *27*, 991.

[29] Perego, M.; Seguini, G.; Scarel, G.; Fanciulli, M.; Wallrapp, F. *J. Appl. Phys.* **2008**, *103*, 43509.

[30] Asahi, R.; Taga, Y.; Mannstadt, W.; Freeman A. J. *Phys. Rev. B.* **2000**, *61*, 7459.

[31] Sze, S. M. *Physics of Semiconductor Devices*; John Wiley & Sons, Inc.: New York, 1981; p790-825.

[32] Nelson, J. *The Physics of Solar Cell*; Imperial College Press.: London, 2002; p276.

[33] Hinckley, S.; Mccann, J. F.; Haneman, D. *Solar Cells* **1986**, *17*, 317

Chapter 4

Light Induced Vectorial Charge Transport within a Single Asymmetric Nanowire

4.1 Introduction

Semiconductor used for direct solar water splitting [1,2] is required to be photoelectrochemically stable with appropriate band gap and energy levels that can support broad absorption of solar spectrum, fast charge transfer at semiconductor/electrolyte interface and efficient water reduction/oxidation half reactions.[1,3] Because of these stringent requirements on bandgap and bandedges, much of early efforts has been focused on the discovery of semiconductors with relatively large bandgap, and mostly UV-absorbing semiconductors.[4-6] On the other hand, the dual-bandgap approach enables the usage of smaller bandgap materials with much better solar spectrum coverage,[7] and it was predicted that such scheme could lead into a PEC system with energy conversion efficiency as high as $\eta = 27\%$.[8]

In natural photosynthetic system, [9] a two-photon process is in operation for the oxidation of water and storage of the solar converted chemical energy in sugar. Similarly, in an ideal dual-bandgap PEC cell, [7] two photons could be used to excite the two semiconductors in close contact. The minority carriers of the two semiconductors will be used for the water oxidation and reduction, while the majority carriers could recombine at

the semiconductor junction. Chemical redox mediators or metal can be introduced for fast electron transfer between two semiconductors.[10, 11]

An asymmetric Si/TiO_2 core/shell nanowire heterostructure was designed to explore feasibility of such dual-bandgap scheme for PEC reaction such as direct solar water splitting. Although TiO_2 has been widely studied in photo-degradation for environmental application and water splitting, its wide bandgap, fast carrier recombination and back reaction limit the energy conversion efficiency [12-14]. Silicon, on the other hand, possesses the proper conduction band edge for the water reduction to generate H_2 with visible light absorption [15-17]. This proposed asymmetric Si/TiO_2 nanowire heterostructures are desirable for direct solar water splitting with water oxidation reaction on TiO_2 surface and reduction reaction on Si surface. In this chapter, charge separation of this asymmetric design is observed at a single nanowire level. Using Kelvin probe force microscopy (KPFM) [18], light-induced local surface potential change within a single asymmetric nanowire is mapped to demonstrate the proposed spatial charge separation mechanism, in a condition mimicking a real water splitting environment. In ensemble measurement, enhanced direct solar water-splitting efficiency is also observed for asymmetric nanowire arrays. These experiments suggest that a dual-bandgap asymmetric configuration with exposed anode and cathode surface indeed helps the charge separation and enhances the photocatalytic activity. Such structure provides an ideal platform for the development of solar fuels generation technology.

4.2 Synthesis of Asymmetric Si/TiO_2 Nanowires

4.2.1 Asymmetric Si/TiO_2 Nanowire

The asymmetric Si/TiO_2 core-shell nanowire structures were synthesized, with one part consisting of a Si nanowire and the other part consisting of a Si/TiO_2 core-shell structure. This asymmetric structure ensures large contact area and charge separation/collection efficiency across the semiconductor/semiconductor and the semiconductor/electrolyte junction.[15, 19-21] Detail synthesis scheme of asymmetric nanowire is illustrated in Figure 4.1. 80 nm of Au nanoparticle catalyst was deposited on a clean p-type Si (111) wafer (10-20 Ωcm) by drop casting of colloidal solution (Ted Pella Inc.) [22], and Si nanowires were vertically grown at 850°C by controlling a flow ratio of $SiCl_4$ (g) to Ar (10% H_2) carrier gas. Au catalyst was removed with KI/I_2 solution followed by rinsing with water. The Si nanowire arrays sample was cleaned by buffered HF (BHF) solution to remove the native oxide layer right before atomic layer deposition (ALD) of TiO_2. 30 nm amorphous TiO_2 shell was coated conformally at 80°C in ALD system using $TiCl_4$ and H_2O as precursors. Later, G-line photoresist (Microchem Corp.), diluted with ethyl acetate, was drop-casted onto the sample to cover the bottom half of the Si/TiO_2 core/shell nanowires, and was baked at 100°C. Then, the sample was immersed in 1:5 BHF solution to etch the top half of the amorphous TiO_2 layer only which was not protected by the photoresist. After

photoresist was removed by O_2 plasma, the sample was post annealed to crystallize TiO_2 to anatase structure at 600°C in air for 1h, confirmed by X-ray diffraction (XRD) and transmission electron microscopy (TEM).

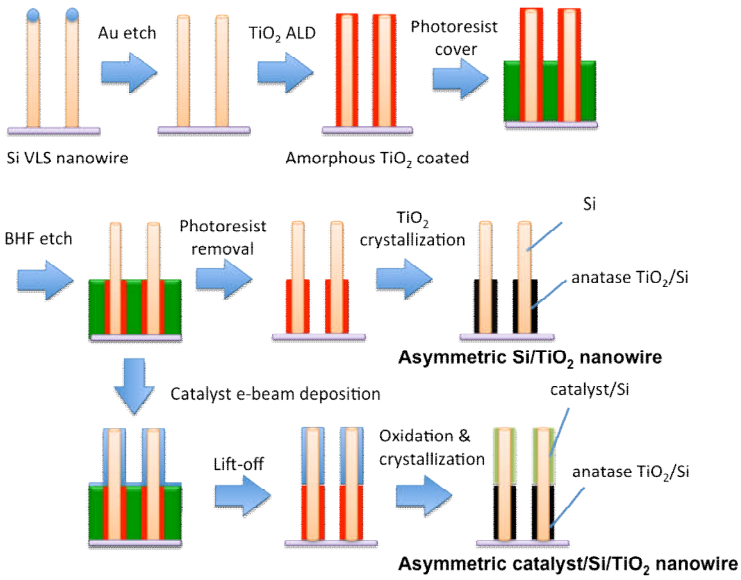

Figure 4.1. A schematic illustration of the asymmetric nanowire fabrication. The Si VLS nanowire in the first step was catalyzed either by 80 nm Au nanoparticles or by Au thin film deposited on the soft-lithographically patterned substrate.

4.2.2 Patterned Asymmetric Si/TiO_2 Nanowires

The patterned asymmetric nanowire arrays sample was also prepared for H_2 generation experiment. By Plasma-enhanced chemical vapor deposition (PECVD), 175 nm oxide layer was deposited on the starting Si wafer mentioned above, and 6% poly-methyl methacrylate (PMMA) in toluene was spin-coated onto the substrate, annealed at 85°C. Then, 500 nm diameter holes with 1μm periodicity were patterned by soft-lithographically.[23] After Cr deposition at a tilting angle as a mask, O_2 plasma and CHF_3/CF_4 plasma were sequentially applied to remove residual PMMA and oxide layers, respectively. 150 nm Au film was e-beam deposited, and PMMA layer was lift-off by acetone which gave a patterned Au film catalyst for Si nanowire growth. Si/TiO_2 asymmetric nanowire arrays are prepared as described above. Before G-line photoresist lift-off, ~5 nm Pt was deposited onto asymmetric nanowire arrays sample by sputtering, therefore having Pt cocatalyst only on Si surface of the asymmetric nanowire arrays.

4.3 Local Surface Potential Mapping in a Single Asymmetric Nanowire

4.3.1 Characterization of Asymmetric Si/TiO_2 Nanowire

Scanning electron microscopy (SEM), and TEM images show that these asymmetric Si/TiO_2 nanowires are typically 5~6 μm in length, with a Si core of 120 nm in diameter and a TiO_2 layer of 30 nm in thickness (Figure 4.2). A sharp junction between the Si and Si/TiO_2 core/shell parts is generated, and the nanowires remain vertical on the Si substrate after all the processing steps. The TiO_2 layer often has single-crystalline domain up to 100 nm.[19]

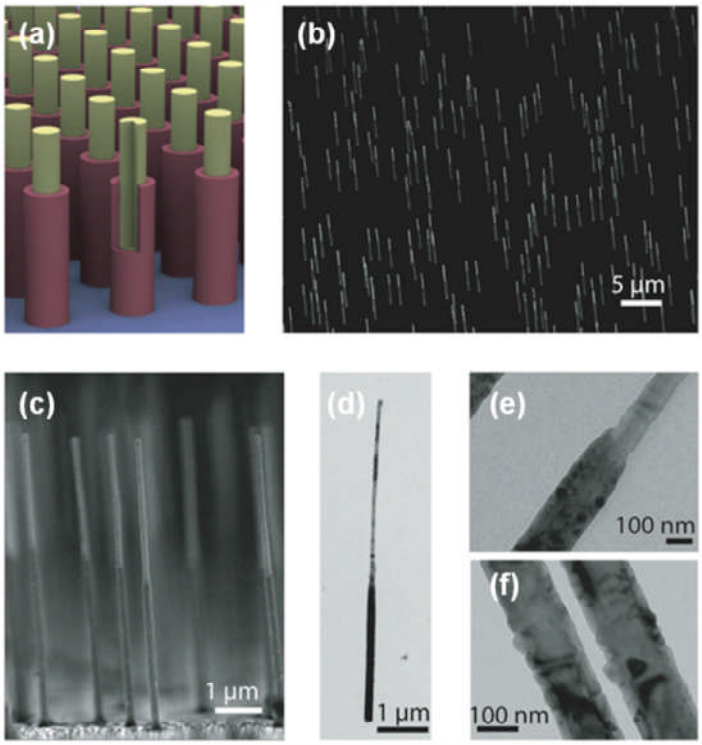

Figure 4.2. (a) Schematic illustration of asymmetric nanowires, with silicon core (yellow) and TiO_2 shell (red). (b) Corresponding tilted SEM image of asymmetric nanowires grown vertically on Si(111) substrate, and (c) a cross-sectional SEM images of asymmetric nanowires, showing the contrast difference between top Si (bright) and bottom Si/TiO_2 (dark) parts. (d)-(f) TEM images of asymmetric nanowires, indicating the sharp Si/TiO_2 junctions (e), and core-shell TiO_2/Si structure (f).

For such asymmetric nanowire heterostructure with dual-bandgap configuration, electron-hole pairs can be generated in silicon and TiO_2 using photons of different wavelengths within the solar spectrum. Because of the band-bending of the space-charge layer at the semiconductor/electrolyte interface,[3] solar illumination would leave positively charged holes on the n-TiO_2 side (anode behavior) and negatively charged electrons on the p-Si side (cathode behavior), with the recombination of majority carriers between the two semiconductors (Figure 4.3a) . As the result, a dipole along the asymmetric nanowire is expected with more positive electrical potential in the n-TiO_2 part relative to that of the p-Si part when both of Si and TiO_2 absorb light (Figure 4.3 a-b). The minority carriers on both semiconductors, with proper energetics, are ready to perform a complete water splitting reaction.[7]

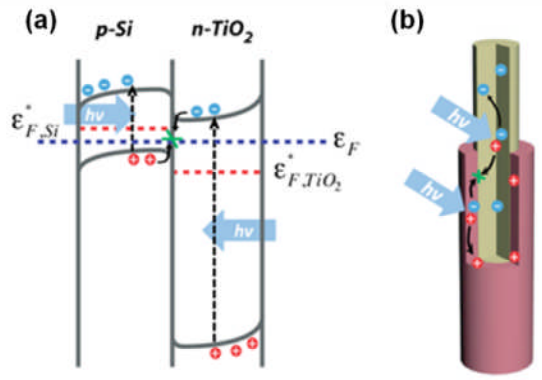

Figure 4.3. (a) Schematic energy diagram of charge separation for the Si/TiO_2 dual-bandgap configuration. The Fermi level in dark (dashed blue) and quasi-Fermi levels under illumination (dashed red) are shown. For simplicity, a uniform distribution of quasi-fermi level is assumed within each part of the asymmetric nanowire. (b) Schematic spatial charge distribution within an asymmetric nanowire under illumination according to (a).

4.3.2 Surface Potential Mapping: KPFM Measurement

To examine this charge separation, KPFM [18] is used to map the surface potential distribution of an isolated asymmetric nanowire. KPFM measurement was performed in Asylum MFP-3D™ stand alone AFM equipped with AEK 2002 acoustic isolation hood. In detail, an asymmetric nanowire was transferred to fused silica substrate (6 mm square shape), patterned with Au grids to minimize static electricity. Then, the quartz substrate was put on top of a large Al sample stage, and there was a hole beneath the quartz substrate (Figure 4.4). 2.5 mW, 365 nm UV LED (T-1 ¾ package, NICHIA Inc.) was put ~0.5 mm underneath quartz substrate to excite both Si and TiO_2. [24] The light intensity was controlled by the current through the LED with an external circuit, and was measured by a calibrated

photodiode (Newport Inc. 71648). Controlled humidity (60~70% r.h) was applied to condense water onto the nanowire surface [25-27] and to establish semiconductor/electrolyte interfaces.

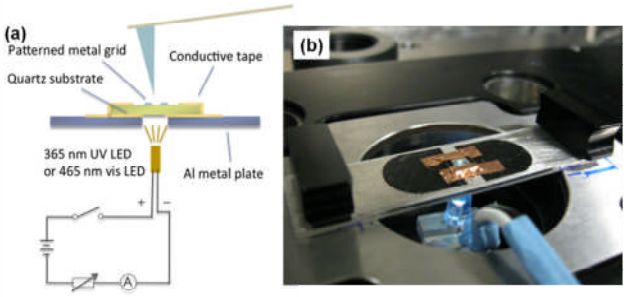

Figure 4.4. (a) Schematic illustration, and (b) a picture of the measurement setup with back side LED illumination.

Topographical AFM image of the asymmetric nanowire was taken before surface potential mapping (Figure 4.5a). The surface potential of the Si/TiO_2 core/shell part was about 15 mV higher than that of the Si-only part in dark (Figure 4.5b), mainly due to the work function difference between these two materials[18]. Under UV illumination, the local surface potential of the Si/TiO_2 part was significantly more positive (by 60 mV) than that of the Si (Figure 4.5c), indicating positive charge buildup on Si/TiO_2 part as expected. This photoresponse of the surface potential was reversible (Figure 4.5d), suggesting that the change of the surface potentials originates from UV illumination.

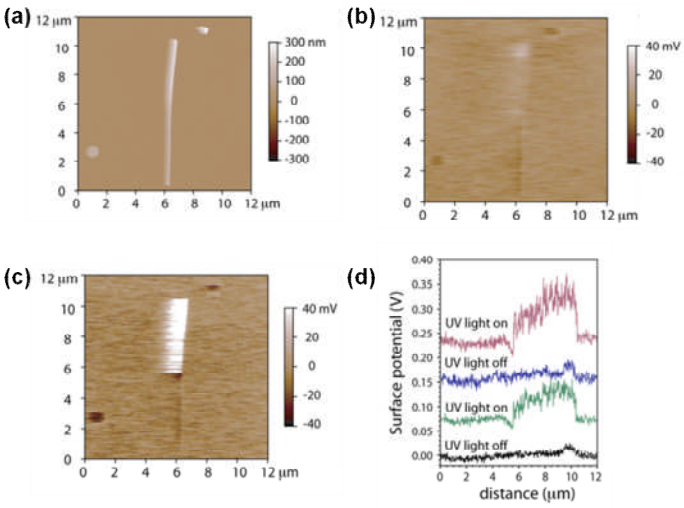

Figure 4.5. (a) Topographical AFM image of the asymmetric nanowire. The surface potential mapping of an asymmetric nanowire (b) in dark, and (c) under 365 nm UV illumination with 4.5 mW/cm^2 intensity (d) Surface potential profiles along an asymmetric nanowire from Si (distance 0 µm) to Si/TiO_2 collected sequentially from bottom to top, switching between dark and UV illumination. The curves are offset for clarity.

Control experiments with both a pristine Si nanowire and a complete Si/TiO_2 core/shell nanowire showed no comparable surface potential changes (Figure 4.6a-b) under the UV illumination. Changing the wavelength of illumination to 465 nm also gave no significant change of surface potential profile (Figure 4.6c) even with a Si/TiO_2 asymmetric nanowire. These control experiments show that photo excitation of both Si and TiO_2 semiconductors, especially TiO_2 activation by UV light, is necessary for effective charge separation in dual bandgap system and dipole formation along the asymmetric nanowire.

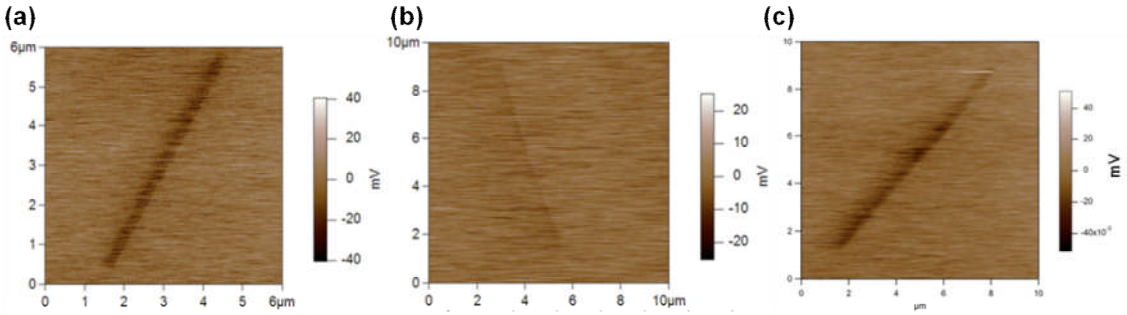

Figure 4.6. Surface potential profile of (a) a Si nanowire, (b) a Si/TiO_2 core-shell nanowire under 365 nm UV illumination (4.5 mW/cm^2), and (c) an asymmetric Si/TiO_2 nanowire under 465 nm visible illumination (4.5 mW/cm^2).

4.3.3 Light Intensity Dependence

The surface potential difference between the Si part and Si/TiO_2 part increased gradually as the light intensity was increased (Figure 4.7) although we consider that the surface potentials on the Si/TiO_2 part were not uniform under illumination (Figure 4.7a), probably because of the domain structure of the TiO_2 shell. The surface potential difference is close to get saturate at high light intensity (Figure 4.7b), expected for dual-bandgap configuration, by flatting of band at semiconductor/electrolyte interface.[7,8] Moreover, our estimation of surface potential difference under UV illumination is consistent with the KPFM measurement, assuming that all the photogenerated minority carriers in TiO_2 contribute to the observed surface potential difference at steady state condition. This suggests that photogenerated minority carriers of holes in the TiO_2 layer and electrons in the Si core can be efficiently separated in our asymmetric core/shell nanostructures which are desirable to complete water oxidation on the TiO_2 layer and hydrogen reduction on the Si part.

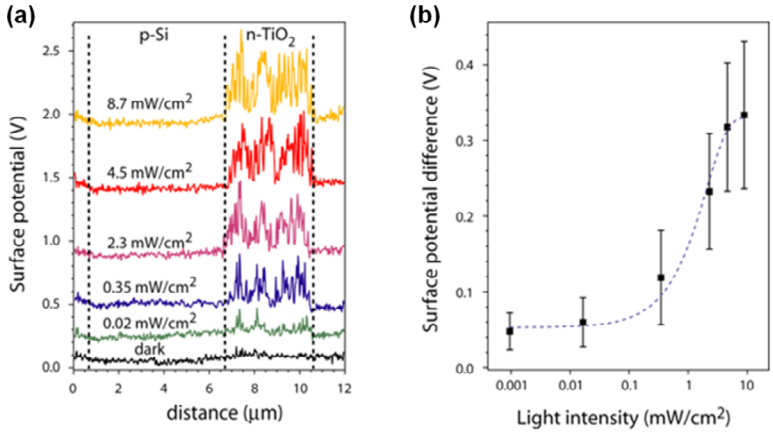

Figure 4.7. Surface potential profile of an asymmetric nanowire measured at different light intensities. The potential profiles are offset for clarity. **b**, Averaged surface potential difference between the Si/TiO_2 core-shell region and the Si region, and its dependence on the intensity of the 365 nm UV light. The error bars on the data indicate the spatial variation of the surface potential of the Si/TiO_2 core-shell region as compared to the averaged value of the Si region caused by the heterogenity of the photoresponse among TiO_2 domains. The average was calculated from multiple samples with different scan parameters performed at the same light intensity.

4.4 H_2 Evolution from Asymmetric Nanowire Arrays

To test the PEC activities with an ensemble of asymmetric nanowires, high density asymmetric nanowire arrays were prepared as mentioned above. The patterned structure provides dense arrays of asymmetric nanowire as well as other desirable property such as light trapping.[15, 28, 29]

Optical images of 1 cm^2 chips of patterned asymmetric nanowire arrays clearly show the periodicity of the nanowires in large scale (Figure 4.8a) and have rainbow color gradient. Asymmetric core-shell nanowire arrays are synthesized with Si cores of 400 nm in diameter and with 30 nm thick TiO_2 coating (Figure 4.8b). In addition, a thin film of Pt layer is selectively coated on the bare Si part as a cocatalyst for H_2 evolution reaction and a protective layer from Si oxide formation (Figure 4.8c).

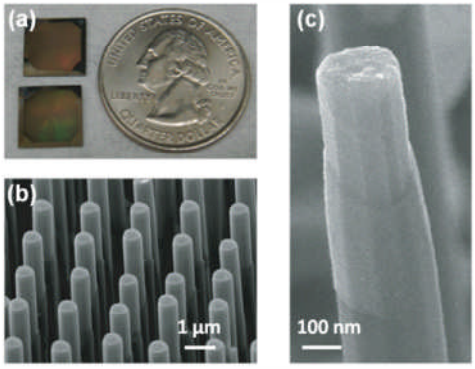

Figure 4.8. (a) optical image of 1cm^2 chips of asymmetric nanowire arrays made from soft-lithography, showing iridescent color because of periodicity. (b)-(c) SEM images of asymmetric nanowire arrays. The top part of an asymmetric nanowire is coated by Pt on Si, and the bottom part is Si/TiO_2 core/shell.

Spontaneous solar water splitting experiments were carried out on these patterned asymmetric nanowire arrays in 5 mL of pure water under illumination from a 500W Hg (Xe) lamp (Newport Inc.) with a liquid filter (Newport Inc.). Nanowire arrays substrate was faced into the incident light through a quartz window of a PEC glassware. Micro gas Chromatography (Agilent Micro GC 3000A) was used to measure the generated H_2 amount, and the weight-normalized photoactivity was calculated based on the geometry taken from SEM and TEM characterization and density of bulk anatase TiO_2. The control experiment was performed with Si/TiO_2 core/shell nanowire arrays which had the same thickness of TiO_2 shell coating over the entire core Si nanowire arrays but no bare Si exposure. The weight-normalized H_2 generation rate of asymmetric nanowire array was typically 2-3 times faster than that of core/shell nanowire arrays (Figure 4.9), which demonstrates the importance of charge separation in asymmetric nanowire design. We were not able to, however, conclusively detect the oxygen evolution, likely due to the formation of peroxide on TiO_2 surface.[30]

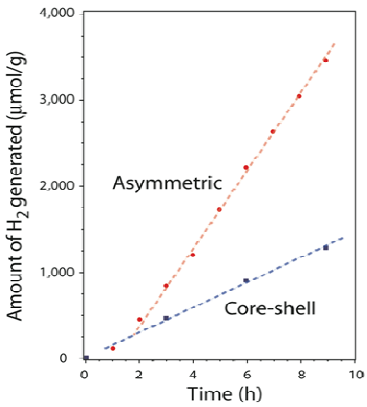

Figure 4.9. Comparison of the weight-normalized hydrogen generation efficiency of asymmetric (red) and core-shell (blue) nanowire arrays.

The observed enhancement of H_2 production over asymmetric nanowires is consistent with the observation in surface potential measurement, as long as the charge transfer across the semiconductor/electrolyte interface is kinetically slower than the charge transfer at the semiconductor heterojunction.[31, 32] The effective charge separation in asymmetric nanowire allows silicon to absorb longer wavelength photon thus contribute towards water reduction, in addition to the UV-absorbing TiO_2 shell. This charge separation at the interface could also possibly reduce back reaction on TiO_2. These two effects enable the utilization of longer wavelength photons and increase the internal quantum efficiency of the asymmetric nanowire, leading to higher efficiency of direct solar water-splitting.

4.5 Conclusion

As a powerful technique to spatially resolve surface potential of materials, KPFM has been widely applied in surface chemistry, light emitting diode, and solar cells. In this study, we applied this technique to a photoelectrochemically relevant nanostructure, and examined the photo-responses of surface potential at semiconductor/electrolyte and semiconductor heterojunctions. The light-induced vectorial charge transport within an asymmetric nanowire was observed through KPFM in a dual-bandgap configuration, indicating minority carriers of semiconductors are separated while majority carriers of semiconductors are recombined at the interface. We also demonstrate that spatial charge separation over Si/TiO_2 asymmetric nanowire structures helps to enhance the overall hydrogen generation activity. This asymmetric nanostructure design could be applicable to other semiconductors, and the overall solar to hydrogen conversion efficiency can potentially be improved further by coupling two visible light absorbers whose carrier generation rates are balanced under solar spectrum for the efficient recombination between majority carriers at the interface between two semiconductors.

This section first appeared in Nano Letters:

Liu, C.; Hwang, Y. J.; (co-first authorship) Jeong, H. E.; Yang, P. "Light-Induced Charge Transport within a Single Asymmetric Nanowire" *Nano. Lett.* **2011**, *11*, 3755-3758.

References

[1] Walter, M. G.; Warren, E. L.; McKone, J. R., Boettcher, S. W.; Mi, Q.; Santori, E. A.; Lewis, N. S. *Chem. Rev*. **2010**, *110*, 6446-6473.

[2] Fujishima, A.; Hongda, K. *Nature* **1972**, *238*, 37-38.

[3] Grätzel, M. *Nature* **2001**, *414*, 338-344.

[4] (a) Khan, S. U. M.; Al-Shahry, M.; Ingler Jr., W. B.; *Science* **2002**, *297*, 2243-2245 (b) Chem., X.; Liu, L.; Yu, P. Y.; Mao, S. S. *Science* **2011**, *331*, 746-750.

[5] Tiley, S. D.; Cornuz, M.; Sivula, K.; Grätezl, M. *Agnew. Chem. Int. Ed.* **2010**, *49*, 6405-6408.

[6] Lu, D.; Takata, T.; Saito, N.; Inoue, Y.; Domen, K. *Nature* **2006**, *440*, 295.

[7] Nozik, A. J. *Appl. Phys. Lett*. **1976**, *29*, 150-153.

[8] Bolton, J. R.; Strickler, S. J.; Connolly, J. S. *Nature* **1985**, *316*, 495-500.

[9] Raven, P. H.; Evert, R. F.; Eichhorn, S. E. *Biology of Plants, 7th Ed.*, 124-127 (W. H. Freeman and Company Publishers, New York, 2005)

[10] Hiroaki, T.; Mitsui, T.; Kiyonaga, T.; Akita, T.; Tanak, K. *Nature Mater*. **2006**, *5*, 782-786.

[11] Abe, R.; Sayama, K.; Sugihara, H. *J. Phys. Chem. B* **2005**, *109*, 16052-16061.

[12] Serpone, N.; Lawless, D.; Khairutdinov, R. *J. Phys. Chem*. **1995**, *99*, 16655-16661.

[13] Bahnemann, D. W.; Hilgendorff, M.; Memming, R. *J. Phys. Chem. B* **1997**, *101*, 4265-4275.

[14] Cowan, A. J.; Tang, J.; Leng, W.; Durrant, J. R.; Klug, D. R. *J. Phys. Chem. C* **2010**, *114*, 4208-4214.

[15] Boettcher, S. W.; Spurgeon J.; Putnam, M. C.; Warren, E. L.; Turner-Evans, D. B.; Kelzenberg, M. D.; Maiolo, J. R.; Atwater, H. A.; Lewis, N. S. *Science* **2010,** *327*, 185-187.

[16] Boettcher, S. W.; Warren, E. L.; Putnam, M. C.; Santori, E. A.; Turner-Evans, D.; Kelzenberg, M. D.; Walter, M. G.; McKone, J. R.; Brunschwig, B. S.; Atwater, H. A.; Lewis, N. S. *J. Am. Chem. Soc*. **2011**, *133*, 1216-1219.

[17] Hou, Y.; Abrams, B. L.; Vesborg, P. C. K.; Bjorketun, M. E.; Herbst, K.; Bech, L.; Setti, A. M.; Damsgaard, C. D.; Pedersen, T.; Hansen, O.; Rossmeisl, J.; Dahl, S.; Norskov, J. K.; Chorkendorff, I. *Nature Mater*. **2011**, *10*, 434-438.

[18] Liscio, A.; Palermo, V.; Samori, P. *Acc. Chem. Res*. **2010**, *43*, 541-550.

[19] Hwang, Y. J.; Boukai, A.; Yang, P. *Nano Lett*. **2009**, *9*, 410-415.

[20] Law, M.; Greene, L. E.; Johnson, J. C.; Saykally, R.; Yang, P. *Nature Mater*. **2005**, *4*, 455-459.

[21] Tian, B.; Zheng, X.; Kempa, T. J.; Fang, Y.; Yu, N.; Yu, G.; Huang, J.; Lieber, C. M. *Science* **2007**, *449*, 885-889.

[22] Hochbaum, A. I.; Fan, R.; He, R.; Yang, P. *Nano Lett*. **2005**, *5*, 457-460.

[23] Choi, S.-J.; Yoo, P. J.; Baek, S. J.; Kim, T. W.; Lee, H. H. *J. Am. Chem. Soc.*, **2004**, *126*, 7744-7745.

[24] Coffey, D. C.; Ginger, D. S. *Nature Mater*. **2006**, *5*, 735-740

[25] Fan, F. F.; Bard, A. J. *Science* **1995**, *270*, 1849-1852

[26] Verdaguer, A.; Weis, C.; Oncins, G.; Ketteler, G.; Bluhm, H.; Salmeron, M. *Langmuir* **2007**, *23*, 9699-9703

[27] Salmeron, M.; Bluhm, H.; Tatarkhanov, M.; Ketteler, G.; Shimizu, T. K.; Mugarza, A.; Deng, X.; Herranz, T.; Yamamoto, S.; Nilsson, *A. Faraday Discuss.* **2009**, *141*, 221-229

[28] Garnett, E.; Yang, P. *Nano. Lett*. **2010**, *10*, 1082-1097.

[29] Kelzenberg, M. D; Boettche, S. W.; Petykiewicz, J. A.; Turner-Evans, D. B.; Putnam, M. C.; Warren, E. L.; Spurgeon, J. M.; Briggs, R. M.; Lewis, N. S.; Atwater, H. A. *Nature Mater*. **2010,** *9*, 239-244.

[30] Kiwi, J.; Gräetzel, M. *J. Mol. Catal*. **1987**, *39*, 63-70.

[31] Law, M.; Greene, L. E.; Radenovic, A.; Kuykendall, T.; Liphardt, J.; Yang, P. *J. Phys. Chem. B* **2006**, *110*, 22652-22663.

[32] Rothenberger, G.; Moser, J.; Grätzel, M.; Serpone, N.; Sharma, D. K.; *J. Am. Chem. Soc*. **1985**, *107*, 8054-8059.

Chapter 5

Si/InGaN Core/Shell Hierarchical Nano-wire Arrays and their Photoelectro-chemical Properties

5.1 Introduction

Photolysis of water with semiconductor materials has been investigated as a clean and renewable energy conversion process by storing solar energy in chemical bonds such as hydrogen.[1-3] Since Fujishima and Honda[4] reported the capability of water splitting with TiO_2, metal oxide semiconductors have been studied extensively due to their stability under photo-anodic conditions.[5-6] However, the valence band of metal oxide semiconductors consists mainly of O 2p orbitals resulting in a low energy maximum (around +3 V vs NHE compared to +1.23 V vs NHE for the water oxidation reaction). This leads to a significant loss in energy from the large difference in potential between the valence band and water oxidation reaction. In addition, lowering the metal oxide bandgap energy for visible light absorption generally comes at the cost of moving the conduction band minimum (CBM) towards lower potentials than the hydrogen reduction potential which cannot perform spontaneous solar water splitting.

On the other hand, metal nitrides have less positive valence band maximum (VBM) potentials than metal oxides because N 2p orbitals have smaller ionization energies than O 2p orbitals.[6-7] For example, GaN is one of the nitride semiconductors that have been studied for photocatalytic applications[8-11] because its CBM and VBM straddle the hydrogen reduction (H^+/H_2) and water oxidation (H_2O/O_2) potentials. Although GaN has a large bandgap (3.4 eV), indium alloying to form InGaN can tune the bandgap from the ultraviolet to the near infrared region[12] encompassing the entire solar spectrum. The $In_{0.5}Ga_{0.5}N$ alloy has a bandgap of around 2.0 eV which is desirable for overall water splitting considering the overpotential for the water oxidation reaction.[13-14] Moses *et al.*[15] calculated that the VBM of InGaN alloy increases in energy almost linearly with indium composition. Therefore, the InGaN alloy was suggested to accomplish spontaneous overall water splitting with up to 50% indium incorporation since both the CBM and VBM can satisfy the energetic requirements. Experimentally, single crystalline $In_xGa_{1-x}N$ nanowires with compositions up to x = 0.4~0.5 have been realized using a halide chemical vapor deposition (HCVD) technique.[16] Although the InGaN alloy is a very promising water splitting material, only a few studies have been reported[17-19] with no studies on nanowire geometries.

One dimensional nanostructures have been demonstrated to be efficient in photoelectrochemical (PEC) cell and photovoltaic cell applications because they can decouple the directions of light absorption and charge carrier collection.[20-21] When the life time of the minority carrier is short, the minority carrier can recombine in bulk before it reaches the semiconductor/electrolyte junction. However, because nanowires have a small radius, the minority carrier can diffuse to the surface before recombination. This can increase charge separation efficiency, especially when the minority carrier diffusion length is comparable to the radius of the nanowire.

This chapter investigates the photoanodic properties of Si/InGaN hierarchical nanostructures consisting of InGaN nanowires grown directly on Si wire arrays. Compared with one dimensional nanostructures, this hierarchical nanostructure provides additional InGaN/electrolyte interfacial area. Complex two or three dimensional nanostructures such as interlinked branches[22-26] and dendritic[27] nanostructures have shown enhanced efficiencies for solar water splitting from increased charge transport or charge separation. In addition, the Si/InGaN hierarchical nanostructure arrays can potentially increase light absorption due to increased scattering from the hierarchical structures.

5.2 Si/InGaN Hierarchical Nanowire Growth for Photoanode

5.2.1 Patterned Si Wire Growth

High surface area Si/InGaN hierarchical nanowire arrays were grown by conformal coating of InGaN nanowires on patterned Si wire arrays on n-Si (111) substrate (resistivity < 0.005 Ωcm). Using plasma-enhanced chemical vapor deposition (PECVD), a 200 nm silicon oxide layer was deposited on a n-Si(111) wafer and photo-lithographically patterned. The oxide layer was dry etched with CHF_3/CF_4 plasma and followed by evaporation of a 120 nm Au film and lift-off of the photoresist. The Si wire arrays were subsequently grown from the patterned Au catalysts with $SiCl_4$ (99.99% Sigma Aldrich) and 10% H_2/Ar at 875 °C. The Vapor-Liquid-Solid (VLS) grown Si wires were 750~ 800 nm in diameter and 20~25 μm in length. After Si wire growth, the Au catalyst was removed from the tops and sidewalls of the Si wires by KI/I_2 gold etchant.

For photoanodic applications, we have reported that a n/n heterojunction can produce higher photocatalytic activity from better charge separation.[28] Therefore, we chose to n-type dope the Si wire arrays with phosphorus since the as-grown InGaN nanowires are n-type. Post-growth doping of the Si wires could also create a better electron conducting pathway for charge collection. A n-type Si substrate, spin coated by spin-on-diffusant (P509, Filmtronics), was placed on top of a Si wire array with a 1 mm spacer and annealed at 900 °C for 4 hr with 10% O_2/Ar flow to diffuse vaporized phosphorus into silicon wire. Afterwards, Si wire arrays were annealed at 1000 °C under vacuum with Ar flow for an additional 2 hr. Under analogous conditions, a silicon (100 nm) on insulator substrate was measured to have a carrier concentration of 10^{20} cm^{-3} from its resistivity (four point).

5.2.2 HCVD InGaN Nanowire Growth

Single-phase InGaN nanowires with homogeneous composition were grown on Si wire arrays and planar n-Si(111) in a three zone HCVD furnace as described in Figure 5.1.[16] $GaCl_3$ (99.999% metals basis, Alfa Aesar), $InCl_3$ (99.999% metals basis, Alfa Aesar), and NH_3 were used as III/V precursors with N_2 as a carrier gas. The composition of InGaN nanowires was controlled by modifying the $GaCl_3$ and $InCl_3$ precursor temperatures. Immediately prior to InGaN nanowire growth, the native oxide was removed from Si wires by using a buffered HF solution. Samples were placed on the 30° tilted quartz plate for conformal coating of the Si wire arrays unless InGaN nanowire bundles preferred to grow on the tips of the Si wires (Figure 5.2). During the reaction, the $GaCl_3$ and $InCl_3$ precursors were kept at 70 °C and 390-415 °C respectively.

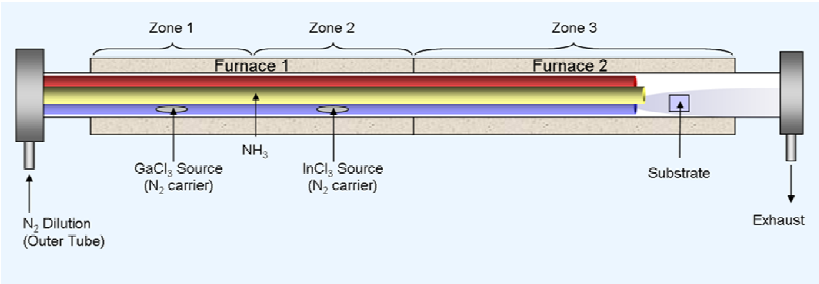

Figure 5.1. Schematic illustration of the three-zone HCVD system. This system has three 1/4-inch quartz tubes housed in a 1-inch quartz tube situated within two furnaces equipped with three independently controlled thermocouples (zones 1-3). The system supplies $GaCl_3$ (N_2 carrier), $InCl_3$ (N_2 carrier), and NH_3 precursors through two inner tubes (blue, yellow). $GaCl_3$ and $InCl_3$ were placed in the same inner tube and spaced apart such that the vapor pressures of each precursor could be independently controlled in zone 1 ($GaCl_3$) and zone 2 ($InCl_3$). N_2 gas also flows through the outer tube during the reaction.

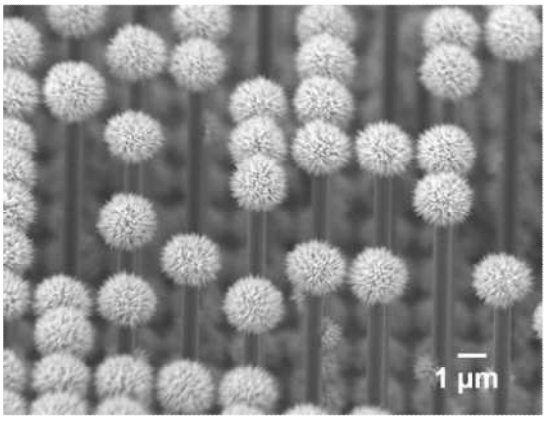

Figure 5.2. Tilted (45°) SEM images of InGaN nanowires grown on Si wires when Si wire arrays sample was placed on non-tilted quart plate. InGaN nanowire bundles (top bright color) are grown on the tips of Si wire arrays, and bare Si are exposed on the side walls of Si wires causing non-uniform InGaN coating.

Scanning electronic microscopy (SEM) images of hierarchical Si/InGaN nanowire arrays show that InGaN nanowires (less than 100 nm in diameter) grow conformally on the Si wire arrays (Figure 5.3). The cross sectional SEM image (Figure 5.3d) of a hierarchical Si/InGaN nanowire clearly shows six facets of the Si wire, usually observed in VLS grown Si wires with the <111> growth direction, with InGaN nanowires grown vertically out of the Si facets. The conformal InGaN coating over Si wires can prohibit photooxidation of Si from direct contact between Si and the electrolyte. Similarly, InGaN nanowires grew vertically from the planar Si(111) substrate as shown in top down and cross sectional SEM

images (Figure 5.3e-f). Elemental analysis using SEM energy-dispersive x-ray spectroscopy (EDS) showed that $In_xGa_{1-x}N$ nanowires have a composition of x = 0.08~0.1.

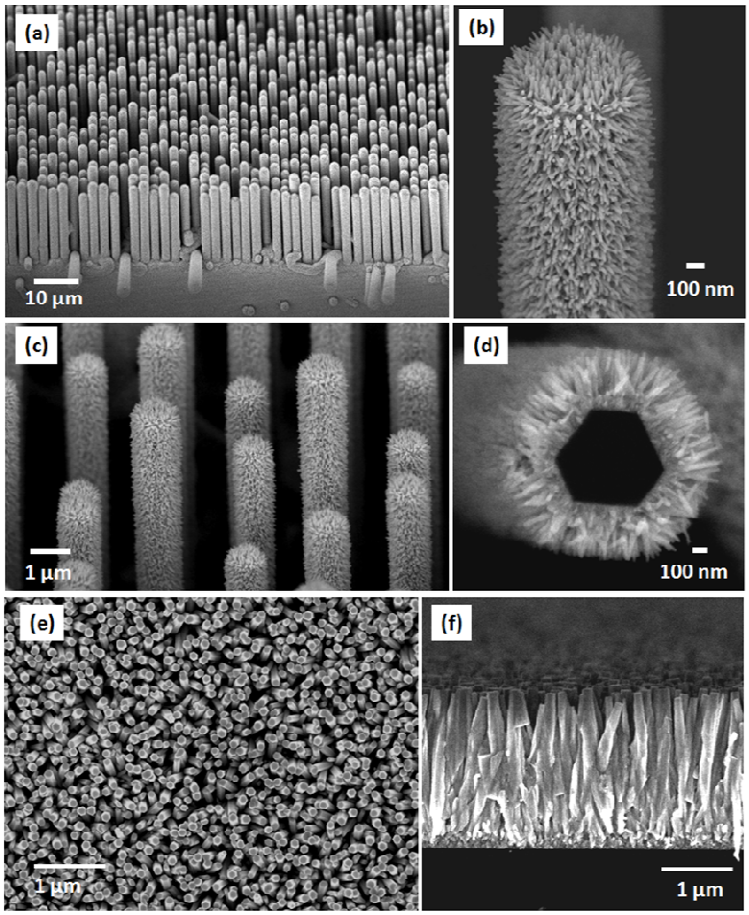

Figure 5.3. Tilted (45°) SEM images of hierarchical Si/$In_xGa_{1-x}N$ nanowire arrays on Si (111) substrate with x = 0.08~ 0.1 (a-c). A fractured wire reveals the cross section (d) showing that InGaN nanowires grow vertically from the six Si wire facets. Top down (e) and cross sectional (f) SEM images of vertical $In_xGa_{1-x}N$ nanowires grown on a planar Si (111) substrate.

X-ray diffraction (XRD) patterns for vertically grown InGaN nanowires on planar Si(111) show predominantly the wurtzite 002 peak (Figure 5.4) which is consistent with previous reports of epitaxially grown InGaN nanowires on Al_2O_3(001) and quartz[16]. However, Si/InGaN hierarchical nanowire arrays show a decrease in intensity of the 002 peak while the 100 and 101 peaks get stronger compared to InGaN nanowires on planar Si. This can be attributed to the difference in geometric orientation of InGaN nanowires on Si wires vs planar Si.

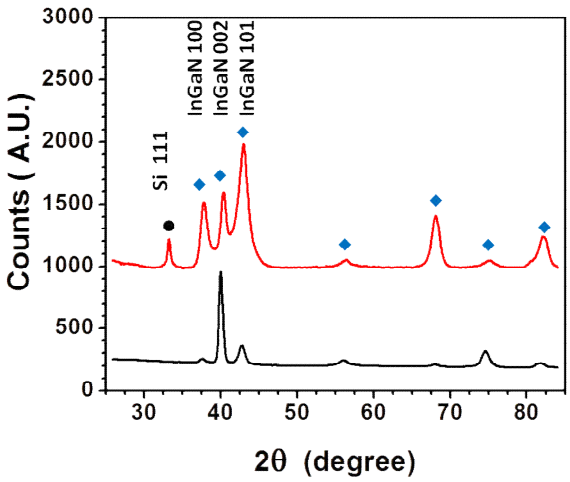

Figure 5.4. X-ray diffraction patterns of $In_xGa_{1-x}N$ nanowires (x = 0.08-0.10) grown on planar Si(111) (black) and Si wires (red). $In_xGa_{1-x}N$ nanowires grown on planar Si (111) show a higher intensity 002 wurtzite peak indicating mostly vertical growth of InGaN nanowires from the silicon surface (blue diamond for wurtzite peak of InGaN) . Hierarchical Si/$In_xGa_{1-x}N$ nanowire arrays show a 111 peak from Si (black dot) wires and all other wurtzite peaks.

5.2.3 Photoanode Preparation

To measure the PEC properties of Si/InGaN, electrodes were constructed from the as grown samples. An In-Ga eutectic was applied to the back side of the Si substrate and a copper wire was connected with silver paste. The substrate and wire were subsequently covered with insulating epoxy (Hysol) to expose only the desired surface area. Samples were immersed in a pH 3 H_2SO_4 solution with 0.5 M of Na_2SO_4 salt as an electrolyte. All PEC measurements were conducted at pH 3 since photoanodic etching of GaN has been observed in both strongly basic (1M KOH) and strongly acidic (1M H_2SO_4) electrolyte.[29] Working electrodes were illuminated through a quartz window of a PEC glass cell. A 300 W Xe lamp (Newport, 6258) was coupled with a diffuser for uniform illumination intensity (samples typically 0.3~0.5 cm^2) and an AM 1.5 filter (Newport, 81094) for simulated sunlight. The illumination intensity was measured with a calibrated Si photodiode. Photocurrents were measured in a three-electrode configuration using an Ag/AgCl reference electrode and a Pt mesh counter electrode.

5.3 Photoanodic Properties of Si/InGaN Hierarchical Nanowire Arrays

5.3.1 Photocurrents

Figure 5.5a shows dark current and photocurrent densities plotted vs the reversible hydrogen electrode (RHE) for Si/InGaN hierarchical nanowire arrays and InGaN nanowires grown on the planar Si substrate. The dark current densities of both samples were negligible until 1.5 V vs RHE. The photocurrent density for hierarchical nanowire arrays increased beginning from 0.1 V vs RHE and reaches 33 μA/cm^2 at 1.23 V vs RHE while InGaN nanowire arrays grown on planar Si only reached a current density of 6 μA/cm^2 at the same bias. We believe that the higher surface areas of hierarchical nanostructures result in higher photocurrent by enhancing the optical pathway and assisting in charge separation.

Hierarchical nanowire arrays were further tested under different illumination conditions (Figure 5.5b) to determine whether the measured photocurrent was due to light absorption. As the input light intensity increases, the InGaN nanowires should absorb more photons resulting in higher photocurrent at the same bias voltage. The photocurrent density increased from 16 μA/cm^2 to 33 μA/cm^2 (at 1.23 V vs RHE) when the portion of UV increased by removing the AM 1.5 filter. It increased further to 62.6 μA/cm^2 (at 1.23 V vs RHE) under a higher light intensity of 350mW/cm^2 without the AM 1.5 filter.

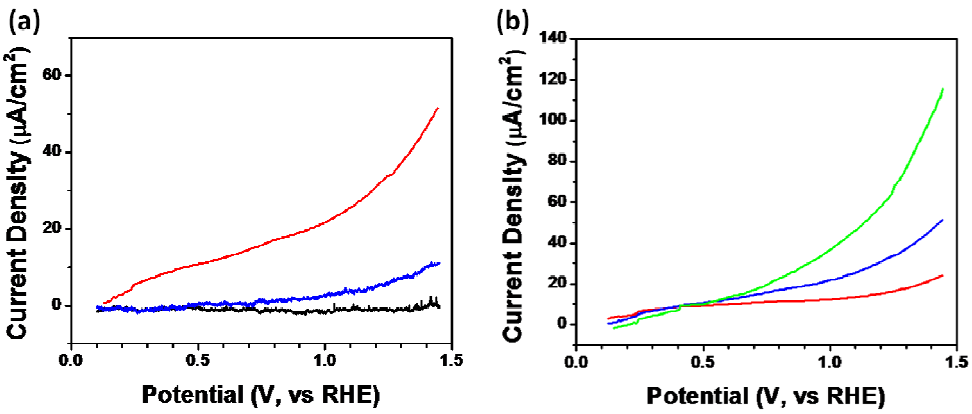

Figure 5.5. Photoelectrochemical measurements on Si/$In_xGa_{1-x}N$ (x = 0.08~0.10) photoanodes. Photocurrent density plots (a) of hierarchical Si/$In_xGa_{1-x}N$ nanowire arrays (red) and planar Si/$In_xGa_{1-x}N$ (blue) under 100 mW/cm^2 without AM 1.5 filter show an increase in current for the hierarchical geometry. A representative dark current density plot is shown in black. Photocurrent density plots (b) of hierarchical Si/$In_xGa_{1-x}N$ nanowire arrays show a photocurrent dependence on illumination condition: red (100mW/cm^2, with AM 1.5 filter), blue (100mW/cm^2, without AM 1.5 filter), and green (350mW/cm^2, without AM 1.5 filter).

5.3.2 Photoanodic Stability

One of the concerns for metal nitride semiconductors is chemical stability to anodic photooxidation. To test the stability of InGaN nanowires, we illuminated the nanowires with a high light intensity (350 mW/cm^2) for 15 hrs in pH 3 electrolyte. The photocurrent density was stable and did not change before and after illumination. Also, no noticeable decomposition of InGaN nanowires was observed by SEM and XRD after illumination. Figure 5.6 show high resolution TEM (HRTEM) images of InGaN nanowires taken from Si/InGaN hierarchical wire arrays after 15 hr of illumination. The images clearly show that the crystalline structure of InGaN nanowires remains intact and with no observed structural decomposition or surface oxide formation. The surface of InGaN nanowires was clean indicating that they were not oxidized during the measurement.

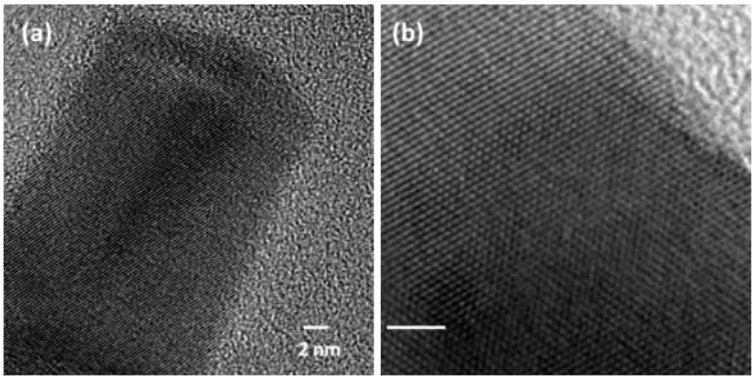

Figure 5.6. High resolution TEM images of a representative InGaN nanowire taken from hierarchical Si/InGaN nanowire arrays after 15 hours of illumination. Nanowires show no obvious photochemical etching or amorphous layer formation after illumination.

5.4 Factors Affecting Quantum Efficiency

To examine the performance of Si/InGaN photoanodes we can compare the measured photocurrent with the theoretical maximum photocurrent assuming a quantum efficiency (QE) of 1. The bandgap of $In_{0.1}Ga_{0.9}N$ is 3.1 eV which can have maximum photocurrent of 1.31 mA/cm^2 for water splitting under AM1.5 illumination. However, the measured photocurrent is only 1.2 % of this maximum photocurrent. Some important processes that can influence the QE in this system are light absorption, charge transport across the Si/InGaN junction, and charge separation at the semiconductor/electrolyte junction. InGaN nanowires have a high absorption coefficient even on planar substrates.[16] Moreover, scattering within the Si/InGaN hierarchical structures is expected to increase

light absorption. Therefore, light absorption is unlikely to be limiting the QE of Si/InGaN hierarchical structures. The charge transport between planar n-Si and InGaN nanowires was checked by measuring the I-V characteristics of the junction (Figure 5.7) which suggest that charge transport across the Si/InGaN junction is also not a limiting factor. The current was measured while a bias voltage was provided between Si and InGaN nanowires. 300 nm of Ti followed by 100 nm of Au were deposited by e-beam evaporation on InGaN nanowire arrays to have ohmic contact. The sample was titled (60 degree) during metal deposition to have a continuous contact through InGaN nanowire. On the other hand, 50 nm of Ti and 100 nm of Au were deposited on the backside of Si substrate for electrical contact on Si side. The shapes of the photocurrent curves are similar to materials known to have fast charge recombination and highly resistive charge transfer processes into solution. Therefore, we expect that a higher photocurrent can be achieved by improving the efficiency of the charge transport within InGaN nanowires and charge transfer at the semiconductor/electrolyte interface.

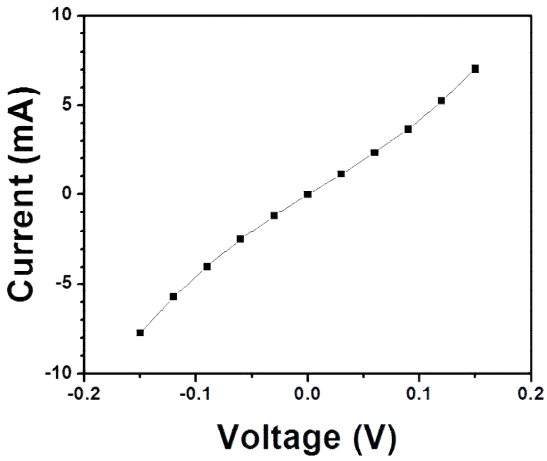

Figure 5.7. Current-Voltage measurement between Si substrate and InGaN nanowires showing low resistivity between Si and InGaN junction.

Several intrinsic material properties can influence excited carrier dynamics at the semiconductor/electrolyte junction. One property is the band bending (photovoltage) at this interface. III-nitrides have been reported to have varying degrees of Fermi level pinning depending on the growth method.[30-31] A direct result of this high electronic state density at the surface is a reduction in photovoltage at the semiconductor/electrolyte junction.[32] This is unfavorable since band bending is the driving force for the separation of photogenerated carriers. One possible method for decreasing surface states is to passivate the surface effectively. Another potential issue for solar water splitting with III-nitrides is fast carrier recombination. Fluorescence dynamics studies on InGaN and other highly strained III-nitride alloys have shown lifetimes on the order of sub 1 ns due to charge localization and native defects.[33-34] Therefore, these alloys tend to have short minority carrier diffusion lengths (<200 nm) which can prevent efficient charge transfer. We propose that the

addition of an oxidation co-catalyst to the surface of our InGaN nanowires could significantly improve charge separation[35] during that short time-scale. An oxidation co-catalyst could also increase photocatalytic activity by reducing the required overpotential for water oxidation. Finally, studies have shown that the photocurrent of n-GaN electrodes is strongly correlated to its carrier concentration.[36] According to the charge transfer model at the semiconductor/electrolyte interface, the photocurrent decreases above the optimized carrier concentration due to the fast recombination in the space charge region. Photovoltage studies on our HCVD grown InGaN nanowires indicate that they are n-type from unintentional doping during growth. Therefore, we believe that the photocurrent can be optimized through better synthetic control of the doping concentration/mobility in InGaN nanowires.

5.5 Conclusion

In this chapter, we have demonstrated the potential for solar water splitting with high surface area Si/InGaN hierarchical nanowire arrays. An enhancement of 5 times in photocurrent was observed when the surface area increased from InGaN nanowires on planar Si to InGaN nanowires on Si wires. The photocurrent generated from Si/InGaN was constant over extended illumination times and no degradation of InGaN nanowires was observed by TEM. These measurements indicate that Si/InGaN hierarchical arrays can be used as stable photoanodes and are promising for efficient solar water splitting. Further work will be done to improve the performance of Si/InGaN hierarchical arrays by examining the effects of surface passivation, oxidation co-catalysts, and controlled doping on InGaN nanowires. Also, we plan to further increase visible light absorption by incorporating more indium into Si/InGaN hierarchical nanowire arrays.

This section first appeared in Nano Letters:
Hwang, Y. J.; Wu, C.; Hahn, C.; Jeong, H. E.; Yang, P. “Si/InGaN Core/Shell Hierarchical Nanowire Arrays for Solar Water Splitting” *Nano. Lett.* **2012**, *12*, 1678-1682.

References

[1] Walter, M. G.; Warren, E. L.; Mckone, J. R.; Boettcher, S.W.; Santori, E. A.; Lewis, N. S. *Chem. Rev.* **2010,** *110,* 6446–6473.

[2] Grätzel, M. *Nature* **2001**, 414, 338-344.

[3] Maeda, K.; Domen, K. *J. Phys. Chem. Lett.* **2010**, 1, 2655-2661.

[4] Fukishima, A.; Honda, K. *Nature* **1972**, 238, 37-38.

[5] Rajeshwar, K. *J Appl Electrochem* **2007**, 37, 765-787.

[6] Maeda, K.; Domen, K. *MRS Bulletin* **2011**, 36, 25-31.

[7] Maeda, K.; Domen, K. *J. Phys. Chem. C.* **2007**, 111, 7851-7861.

[8] Beach, J. D.; Collins, R. T.; Turner, J. A. *J. Electrochem. Soc.* **2003**, 150, A899-A904

[9] Maeda, K.; Teramura, K.; Saito, N.; Inoue, Y.; Domen, K. *Bull. Chem. Soc. Jpnt.* **2007**, 80 , 1004-1010.

[10] Wang, D.; Pierre, A.; Kibria, M. G.; Cui, K.; Han, X.; Bevan, K. H.; Guo, H.; Paradis, S. ; Hakima, A. R.; Mi, Z. *Nano. Lett.* **2011**, 11 , 2353-2357.

[11] Jung, H. S.; Hong, Y. J.; Li, Y.; Cho, J. ; Kim, Y. J.; Yi, G. C. *ACS Nano*, **2008**, 2, 637-642.

[12] Kuykendall, T.; Ulrich, P.; Aloni, S.; Yang, P. *Nat. Mater.* **2007**, *6* , 951-956.

[13] Bolton, J. R.; Strickler, S. J.; Connolly, J. S. *Nature* **1985**, 316, 495-500.

[14] Wang, H.; Deutsch, T.; Turner, J. A. *ECS Transactions* **2008**, 6, 37-44.

[15] Moses, P. G.; Van de Walle. C. G. *Appl. Phys. Lett.* **2010, 9**6, 021908.

[16] Hahn, C.; Zhang, Z.; Fu, A.; Wu, C. H.; Hwang, Y. J.; Gargas, D. J.; Yang, P. *ACS Nano*, **2011**, 5, 3970-3976.

[17] Fujii, K.; Kusakabe, K.; Ohkawa, K.; *Jpn. J. Appl. Phys.* **2005,** 44, 7433–7435

[18] Li, J.; Lin, J. Y.; Jiang, H. X.; *Appl. Phys. Lett.* **2008, 9**3, 162107.

[19] Theuwis, A.; Strubbe, K.; Depestel, L. M.; Gomes, W. P. *J. Electrochem. Soc.* **2002**, 149, E173-E178.

[20] Shankar, K.; Basham, J. I.; Allam, N. K.; Varghese, O. K.; Mor, G. K.; Feng. X.; Paulose, M.; Seabold, J. A.; Choi, K. S.; Grimes. C. A. *J. Phys. Chem. C.* **2009**, 113, 6327-6359.

[21] Kayes, B. M.; Atwater, H. A.; Lewis, N. S. *J. Appl. Phys.* **2005**, *97*, 114302.

[22] Lin, Y.; Zhou, S.; Liu, X.; Sheehan, S.; Wang, D. *J. Am. Chem. Soc.* **2009**, 131, 2772-2773.

[23] Lin, Y.; Yuan, G.; Liu, R.; Zhou, S.; Sheehan, S. W.; Wang, D. *Chem. Phys. Lett.* **2011**, 507, 209-215.

[24] Shi, J.; Hara, Y.; Sun, C.; Anderson, M. A.; Wang, X. *Nano. Lett.* **2011**, 11 , 3413-3419.

[25] Cho, I. S.; Chen, Z.; Forman, A. J.; Kim, D. R.; Rao, P. M.; Jaramillo, T. F.; Zheng, X. *Nano. Lett.* **2011**, 11 , 4978–4984.

[26] Bierman, M. J.; Jin, S. *Energy Environ. Sci.* **2009**, 2, 1050–1059.

[27] Kay, A.; Cesar, I.; Grätzel, M. *J. Am. Chem. Soc.* **2006**, 128, 15714-15721.

[28] Hwang, Y. J.; Boukai, A.; Yang, P. *Nano. Lett.* **2009**, 9 , 410-415.

[29] Huygens, I. M.; Strubble, K.; Gomes, W. P. *J. Electrochem. Soc.* **2000**, 147, 1797-1802.

[30] Kočan, M.; Rizzi, A.; Lüth, H.; Keller, S.; Mishra, U. K. *Phys. Stat. Sol. (b)* **2002**, 234, 773-777.

[31] Segev, D.; Van De Walle, C. G. *Europhys. Lett.* **2006**, 76, 305-311.

[32] Bard, A. J.; Bocarsly, A. B.; Fan, F. F.; Walton, E. G.; Wrighton, M. S. *J. Am. Chem. Soc.* **1980**, 102, 3671-3677.

[33] Sun, C. K.; Keller, S.; Wang, G.; Minsky, M. S.; Bowers, J. E.; DenBaars, S. P. *Appl. Phys. Lett.* **1996**, 69, 1936-1938.

[34] Chichibu, S.F.; Uedono, A.; Onuma, T.; Haskell, B.A.; Chakraborty, A.; Koyama, T.; Fini, P.T.; Keller, S.; Denbaars, S.P.; Speck, J.S.; Mishira, U.K.; Nakamura, S.; Yamaguchi, S.; Kamiyama, S.; Amano, H.; Akasaki, I.; Han, J.; Sota, T. *Nat. Mater.* **2006**, 5, 810-816.

[35] Yoshida, M.; Yamakata, A.; Takanabe, K.; Kubota, J.; Osawa, M.; Domen, K. *J. Am. Chem. Soc.* **2009**, 131, 13218-13219.

[36] Ono, M.; Fujii, K.; Ito, T.; Iwaki, Y.; Hirako, A.;Yao, T.; Ohkawa, K. *J. Chem. Phys.* **2007**, 126, 054708.

Chapter 6

Design of Efficient Self-Driven Solar to Water Splitting Device: Si Nanowire Photocathode Linked with Si Photovoltage Cell Embedded TiO_2 Photoanode

6.1 Introduction

Photoelectrolysis of water with semiconductors have been intensely investigated to convert solar energy to chemical energy such as hydrogen.[1-5] For spontaneous water splitting, semiconductor must satisfy several requirements. First, the bandgap of the semiconductor needs to be greater than 1. 23 eV, the potential difference between hydrogen evolution reaction (HER) and the oxygen evolution reaction (OER), and the ideal bandgap would increase up to 1.6~1.9 eV considering the overpotentials for each reaction.[6] According to a thermodynamic point of view, conduction band minimum (CBM) and valence band maximum (VBM) of the semiconductor have to straddle the potentials of HER and OER. [7] Lastly, the semiconductor must be stable in aqueous solution during photolysis reaction, and ideally want to be inexpensive and non-toxic.

In the first report on photoelectrolysis of water, Fujishima and Honda [8] demonstrated oxygen evolution at n-TiO_2 electrode, and hydrogen evolution at a Pt counter electrode. However, since the CBM of rutile TiO_2 cannot provide a high enough potential for HER, an external bias potential (0.25~ 0.5 V) is required to fulfill the water splitting. [9-10] If the Pt electrode replaces with a p-type semiconductor whose CBM is higher than hydrogen reduction potential, an additional photovoltage generated at its junction with the electrolyte can make that the Fermi level of the electrons in the p-type semiconductor reach the sufficiently high potential level for HER.[8] Therefore, a photoelectrochemical (PEC) cell, in which an n-type semiconductor photoanode and a p-type semiconductor photocathode (p-n PEC) are immersed in the same electrolyte, has been proposed to increase the chemical conversion efficiency.[11-20] Weber and Dignam reported [21-22] that theoretical upper limit with the p-n PEC cell (9.8~16.6%) is higher than a single semiconductor electrode cell (4.5~11.6%), and the efficiencies with the p-n PEC cell are less sensitive to changes in fill factor and overpotential of reaction.[21] In addition, p-n PEC type of water splitting cell can provide an increase in light absorption by using smaller bandgap semiconductors since bandedges of each semiconductor are required to satisfy only one of HER or OER condition.[22]

In the p-n PEC cell, holes and electrons are separated in space charge regions of the respective semiconductors. Photogenerated minority carriers in each semiconductor transport to the electrolyte interface and use for OER (holes in n-type semiconductor) and HER (electrons in p-type semiconductor). Meanwhile, photogenerated majority carriers move to back contacts where they are recombined. Therefore, the Fermi level of electrons in n-type semiconductor needs to be higher than that of holes in p-type semiconductor for the facile recombination between majority carriers.[14-15] For self-driven water splitting, a positive illuminated open-circuit voltage (V_{oc}) is required when the voltage of p-type electrode is measured with respect to the n-type electrode, [21] while a negative V_{oc} indicates an additional external bias voltage is necessary. A positive V_{oc} in the p-n PEC cell is the first criteria for self-driven water splitting, although the efficiency of the device is not governed by V_{oc} but by the operating photocurrent (I_{op}). The I_{op} of the p-n PEC cell can be estimated from the intersection point of the individually tested current-voltage (I-V) data for each n- and p-type semiconductor, since the photocurrent at each semiconductor electrode must be matched.[1,21] The I_{op} can increase when the onset potential of photocurrent with p-type semiconductor is more cathodic than that of photocurrent with n-type semiconductor, and fill factor of individual electrode increases, which are strongly related with the electron transfer kinetics and the quality of the semiconductor/electrolyte junction.[21-22]

Since Yoneyama *et al.* firstly demonstrated the p-n PEC cell with combination of n-TiO_2 and p-GaP,[11] n-TiO_2 has been coupled with other p-type materials (p-CdTe, and p-SiC) [13,19] but not with p-Si yet due to the early concern of poor current increase [11] although

H_2 evolution with p-Si has been improved and Si is an abundant material.[23-25] Decoration of the noble metals on p-Si such as Pt can improve fill factor, output photovoltage, and therefore, overall efficiency.[23] Furthermore, Si wire geometry has been proposed to increase the collection efficiency despite the short minority diffusion length of p-Si. [25-26]

This chapter demonstrates the p-n PEC cell with the combination of n-TiO_2 and p-Si, as a model system, and several strategies are demonstrated to improve solar to hydrogen (STH) efficiency. First, photovoltaic cell embedded electrode (PV/PEC) is constructed to utilize photovoltage from PV cell. The integrated PV cell can provide a bias voltage to the semiconductor to vary the energetics of its bandedges and manage the onset potential of the photocurrent.[27-31] This chapter also verifies the effects of the embedded PV cell on the photoanodic properties of TiO_2 as well as on I_{op} in the p-n PEC cell. Second, the surface of electrode was modified. The platinized p-Si photocathode can increase the fill factor and have a more positive onset potential of the photocurrent compared to the bare p-Si by reducing the overpotential for HER on the Si surface. [23-25] The surface of silicon was also modified with thin film of TiO_2 atomic layer deposition (ALD) to increase HER activities as well as stability of the electrode. With all of these strategies, we could enhance I_{op} of the p-n PEC cell by 100 times, which also demonstrate that p-n PEC configuration is very promising approach for self-driven solar water splitting considering the fact that it is very challenging to find a single material satisfying all of the requirements.

6.2 PV Cell Embedded Si/TiO_2 Nanowire Arrays for Photoanode

6.2.1 Fabrication of PV Cell Embedded Si/TiO_2 Nanowire Arrays

A large bandgap material can be joined physically to a smaller bandgap photovoltaic device such that the latter is expected to provide an electrical bias for the former. Due to a wide bandgap of TiO_2 (Eg = 3.2 eV, anatase), visible light of solar spectrum will not be utilized for water splitting, but transmitted photons can be absorbed by the embedded Si PV cell due to smaller bandgap of Si (Eg = 1.1 eV). The PV cell with the Si nanowire arrays (n-Si/p-Si) was prepared as described in the previous report.[32] n-type Si nanowire arrays were fabricated by dry etching of n-Si(100) wafer (0.66~0.8 ohmcm) with monolayer of 500 nm silica beads as a mask until the length of wire was about 5 μm. Thermal decomposition of BCl_3 (g) diluted by 10% H_2/Ar carrier gas at 900 ^oC compensated the top shell layer to highly doped p-type Si (n-Si/p-Si nanowire). For the Si /TiO_2 core/shell photoanode, 45~ 50 nm thin layer of TiO_2 was deposited by ALD at 300 ^oC on n-Si and n-Si/p-Si samples which were clean by buffered HF solution right before the deposition. The thickness of the TiO_2 on the Si nanowire was measured by transmission electron microscopy (TEM) images.

Figure 6.1a shows that scanning electron microscopy (SEM) images of the n-type Si nanowire arrays. The n-Si nanowire arrays are 5 μm long with hexagonal shape and their diameters are are 500 nm close to the size of silica beads. The morphology of the n-Si/p-Si nanowire arrays were maintained even after boron doping with BCl_3 (gas) at 900 ^oC (Figure 6.1b) for 10 min. Figure 6.1c-d show the top view and cross sectional SEM images of n-Si and n-Si/p-Si nanowire arrays after 45~50 nm of ALD TiO_2 deposition showing polycrystalline deposition of TiO_2. The deposited TiO_2 shell was confirmed to be anatase structure by x-ray diffraction patterns as we reported previously.[33]

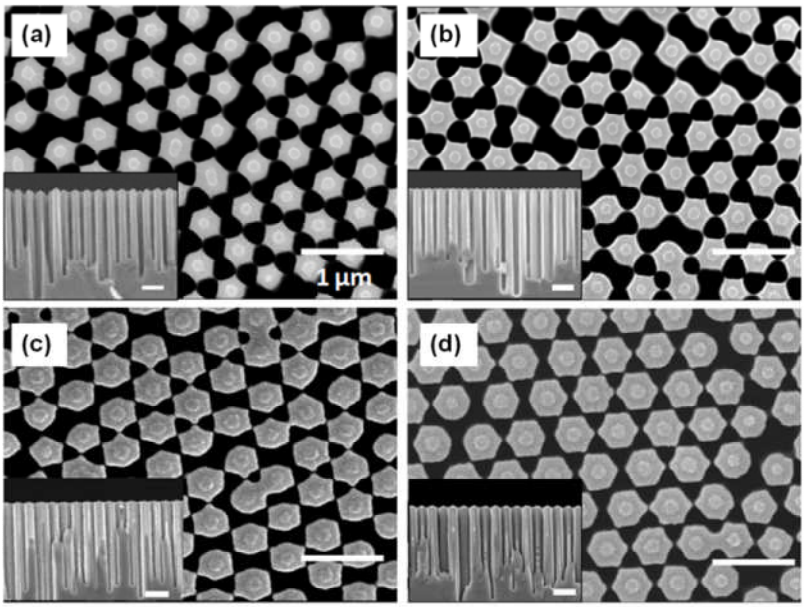

Figure 6.1. SEM images of (a) n-Si nanowire, (b) n-Si/p-Si nanowire, (c) n-Si/TiO_2 nanowire, and (d) n-Si/p-Si/TiO_2 nanowire. Insets are the cross-sectional SEM images of the corresponding samples showing the nanowire arrays are ~5 μm long. Scale bars are 1 μm.

6.2.2 Polarity of Embedded PV Cell

To examine an effect of the polarity of the embedded Si PV cell on the photoanodic properties, planar TiO_2 photoanodes with two opposite polarities of the Si PV cell were prepared respectively: n-Si/p-Si PV cell embedded TiO_2 photoanode (npSi/TiO_2, thin p-Si layer is contacting with n-TiO_2), and p-Si/n-Si PV cell embedded TiO_2 photoanode (pnSi/TiO_2, thin n-Si layer is contacting with n-TiO_2). The planar npSi/TiO_2 sample was prepared similarly to the nanowire device but a clean n-type Si(100) was used for boron doping and ALD TiO_2 deposition. Meanwhile, for the planar pnSi/TiO_2 photoanode, a p-

type Si(100) (1~2 ohmcm, Boron) wafer was cleaned and doped by phosphorous at 900 ^{o}C for 40 min after spin coating of a spin-on-dopant (Honeywell, phosphorous 8545).[34] The surface of the wafer was cleaned by O_2 plasma followed by cleaning with the buffered HF, before TiO_2 ALD was coated.

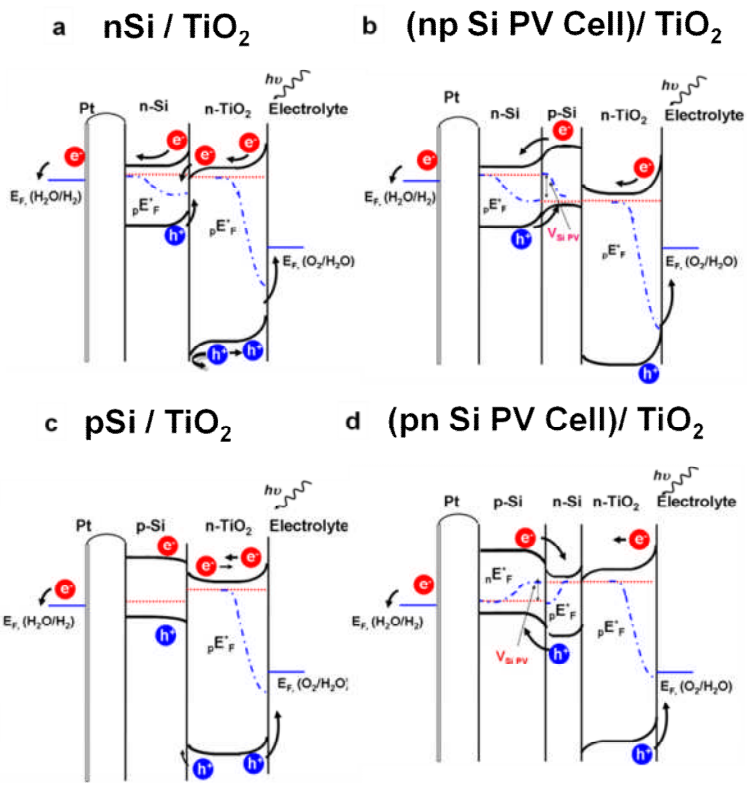

Figure 6.2. Schematic energy diagram of (a) n-Si/TiO_2 photoanode, (b) n-Si/p-Si PV embedded TiO_2 photoanode, (c) p-Si/TiO_2 photoanode, and (d) p-Si/n-Si PV embedded TiO_2 photoanode under illumination, showing the embedded PV cell can provide an extra bias potential in the opposite direction depending on the polarity of the embedded PV cell.

The schematic energy diagrams of PV cell embedded TiO_2 photoanodes are shown with charge flows (Figure 6.2). In the case of npSi/TiO_2 photoanode (Figure 6.2b), the core n-Si/p-Si junction can provide positive photovoltage to the TiO_2 layer since p-Si layer is contacting to TiO_2 layer.[1] The amount of the photovoltage provided by the embedded Si PV cell and the photocurrent with PV/PEC cell are given uniquely by an intersection between the I-V curve of n-Si/p-Si PV cell and that of the n-TiO_2 electrode (Figure 6.3 and 6.4) since the charge flow rates across junctions such as Si/TiO_2, TiO_2/electrolyte, and Si to counter electrode are required to be balanced at a steady state condition.[30] According to the I-V photoresponse of the n-Si/p-Si PV cell and the n-Si/TiO_2 photoanode (Figure 6.4a-b),

the biasing voltage is expected to be + 0.585 V in the planar npSi/TiO_2 photoanode. On the other hand, a negative bias photovoltage output is expected to the TiO_2 shell in the case of the pnSi/TiO_2 photoanode since the polarity of the Si PV cell is the opposite and n-type Si connects with TiO_2 layer (Figure 6.2c-d). Similarly, from the overlap between IV curve of the planar p-Si/n-Si PV cell and that of the pSi/TiO_2 photoanode (Figure 6.4c-d), the biasing voltage is expected to be - 0.48 V in the planar pnSi/TiO_2 photoanode.

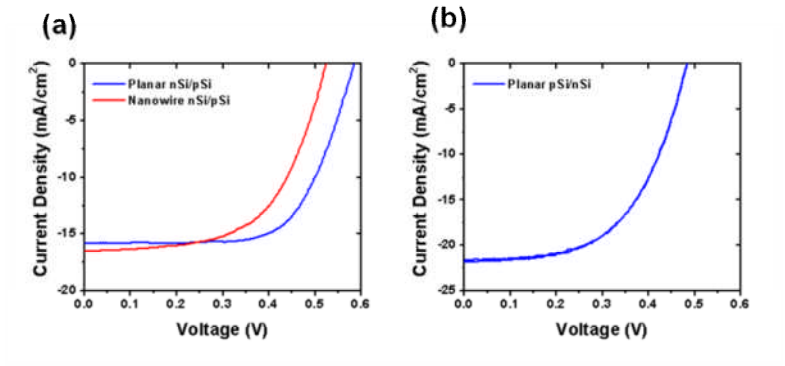

Figure 6.3. I-V photoresponse of Si PV cell under AM 1.5 simulated sunlight illumination: (a) planar and nanowire PV cell of n-Si/p-Si junction prepared by boron doping on n-Si sample, and (b) planar PV cell of p-Si/n-Si junction prepared by phosphorous doping on p-Si sample.

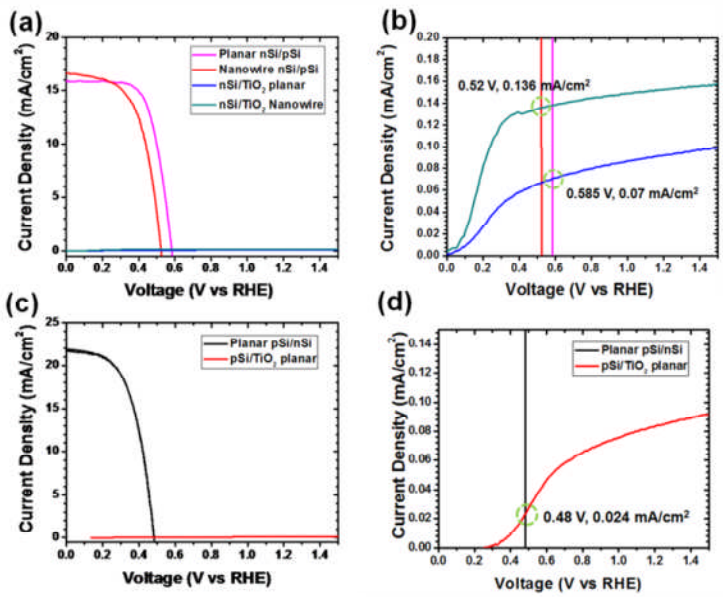

Figure 6.4. I-V photoresponses of embedded PV cell and photoanode: (a) n-Si/p-Si PV cell, and n-Si/n-TiO_2 photoanode of planar and nanowire geometry, and (b) the enlarged graph of (a) showing the intersection of I-V curves of PV cell and photoanode. (c) p-Si/n-Si PV cell and p-Si/ n-TiO_2 photoanode, and (d) the enlarged graph of (c).

6.2.3 Photoanodic Properties of n-Si/p-Si PV Embedded TiO_2 Photoanode

Photoanodic properties of the Si PV cell embedded TiO_2 planar photoanodes were measured with a Pt counter electrode (CE) in 1M KOH (pH 13.6) electrolyte under 100 mW/cm^2 (Figure 6.5a). The onset potential of the n-Si/nTiO_2 electrode is more negative than that of the p-Si/nTiO_2 due to band bending at Si/TiO_2 junction which is consistent with our previous reports.[33] When npSi PV cell was embedded, onset potential of the TiO_2 photoanode (-1.62 V vs CE) shifted toward more negative potential by 490 mV (± 30 mV) compared to that of simple n-Si/n-TiO_2 junction photoanode (-1.13 V vs CE) as expected from the schematic energy diagram in Figure 6.2b. However, the photoanodic currents became similar as the biased potential increase more positively (more than + 0.5 V vs CE) since the current is mainly limited by the absorption of TiO_2 layer under the anodically highly biased potential. The photocurrent enhancement with the npSi embedded PV cell was especially distinguishable closed to the onset potential region where the charge separation is less efficient due to small electric field at TiO_2/electrolyte. The extra + 0.5 V potential generated by the embedded npSi PV cell can move the valence band of TiO_2 toward positive potential and increase the electric field, a driving force for hole to transfer to the electrolyte.[9] Meanwhile, the onset potential of the pnSi/TiO_2 electrode had more anodical open circuit potential (- 0.50 V vs CE) than the p-Si/TiO_2 photoanode (- 0.87 V vs CE) by 370 mV since the negative bias potential from the pnSi PV cell move the quasi Fermi level of the holes to less positive potential.

The npSi/TiO_2 photoanode (0.075 mA/cm^2) shows higher photocurrent and conversion efficiency than the pnSi/TiO_2 (0.03 mA/cm^2) at zero bias potential (vs CE). This reiterates the embedded PV cell can provide an extra photovoltage under illumination, and the npSi PV cell is favorable polarity for the n-TiO_2 photoanode to increase the spontaneous water splitting activity. The n-type/p-type junction is desirable PV cell in the case of a photoanode by providing a positive extra potential as suggesting here, while p-type/n-type junction is required in the case of a photocathode. [28]

Figure 6.5b shows the photoanodic currents of the npSi PV cell embedded TiO_2 electrodes with planar and nanowire structures measured with three-electrode configuration as a conventional measurement. An Ag/AgCl reference electrode and a Pt counter electrode were used. The onset of the photocurrent from npSi/TiO_2 nanowires was shifted cathodically by 440 mV (± 50 mV) which was about 50 mV smaller compared to a planar npSi/TiO_2 device, consistent with the smaller V_{oc} of the Si nanowire PV cell. The Si nanowire PV cell shows about 60 mV smaller V_{oc} than the planar PV cell. The higher surface area of the nanowire geometric PV cell can cause the smaller V_{oc} due to the fast recombination velocity through the surface states. [32, 35]

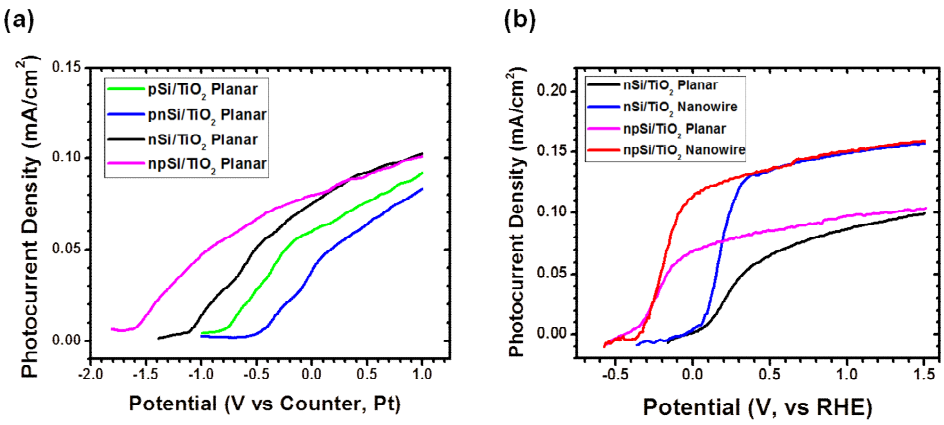

Figure 6.5. (a) Photocurrent densities of the PV cell embedded planar TiO_2 photoanodes: two opposite polarities, npSi/TiO_2 and pnSi/TiO_2, showing that the onset potential of the photocurrents shifts in the opposite direction depending on the polarity. (b) Photocurrent densities of the planar and the nanowire structure of npSi/TiO_2 photoanode.

The npSi/TiO_2 nanowire arrays have about 1.6 times higher photocurrent (0.16 mA/cm^2) at 1.23 V vs RHE compared to the planar device (0.10 mA/cm^2) although the calculated surface area of the nanowire arrays increased by 10 times based on the geometry from the SEM images. We expect the relative smaller enhancement in the photocurrent compared to the enhancement in surface area is because core Si and shell TiO_2 compete to absorb UV light ($\lambda < 380$ nm). Si has a direct band gap of ~ 3.2 eV which is similar to the bandgap of anatase TiO_2. When the core Si absorbs light, the excited holes cannot contribute to oxidation of water [33] because the VBM of Si locates higher than the VBM of TiO_2.

As a model system, TiO_2 shows that the embedded core/shell nanowire of the Si PV cell can shift the onset potential of the photocurrents with the assistance of the photovoltage, and higher surface area of nanowire arrays can increase the photocurrents although the photocurrent is limited by the absorption of the TiO_2. The larger photocurrents can be realized with smaller bandgap materials, and the onset potential of photocurrent can be adjustable with the embedded PV cell.

6.2.4 IPCE of npSi/TiO_2 Nanowire Photoanode

Incident photon to current conversion efficiency (IPCE) was measured at 1.5 V vs RHE in 1M KOH (Figure 6.6). nSi/TiO_2 and npSi/TiO_2 show almost same IPCE within error bar at 1.5 V vs RHE although IPCE varies at smaller bias potential which will be discussed later. This is because the quantum efficiencies are determined by the absorption of TiO_2 when the bias voltage was anodically positive enough. The onset of the

photocurrent is λ=390 nm consistent with the bandgap of anatase TiO_2, and the nanowire device has higher IPCE than the planar device under the entire spectrum region (λ < 390 nm). The IPCE increases as the wavelength of the light gets shorter toward 310 nm since the absorption efficiency increase due to larger absorption coefficient,[36] and electron diffusion loss is not significant in anatase TiO_2 electrode.[37]

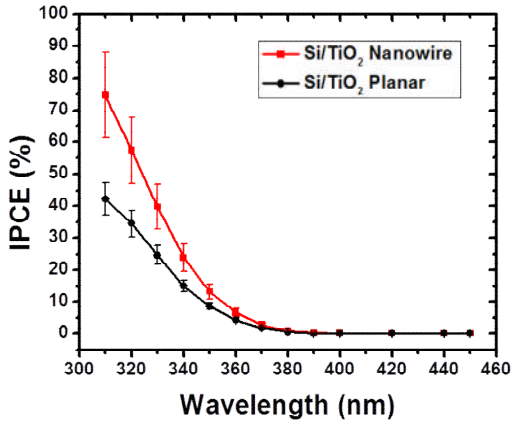

Figure 6.6. IPCE of planar, and nanowire npSi/TiO_2 photoanodes measured at 1.5 V vs RHE in 1M KOH electrolyte.

The effect of the embedded PV cell on the external quantum efficiency (EQE) was examined experimentally by measuring IPCE under various bias voltages in the range of λ = 310 nm ~ 390 nm with the nSi/TiO_2 nanowire (Figure 6.7a and c) and the npSi/TiO_2 nanowire devices (Figure 6.7b and d). The onset potentials of the IPCE (- 0.8 V vs RHE) were similar at λ=310 nm with and without the embedded Si PV cell since most of the incident light is absorbed by the 40~50 nm of TiO_2 shell.[36] Therefore, contribution of the embedded PV cell to IPCE enhancement is not significant at short wavelength. As the wavelength of the incident light gets longer, the less amount of incident light is absorbed by TiO_2 shell due to smaller absorption coefficients [36] so that a core Si PV cell can absorb light and generate a photovoltage. Therefore, the onset potentials of the IPCE move toward more cathodically when the incident light varies from 320 nm to 370 nm. The bias potential caused by the embedded PV cell increases the charge collection efficiency under the same absorptance efficiency of TiO_2 shell. IPCE of the npSi/TiO_2 nanowire device measured under - 0.65 V vs RHE has the maximum value of 20 % at λ=330 nm (Figure 6.7d) while that of the nSi/TiO_2 nanowire device was almost zero (less than 2 %). (Figure 6.7b) This is because the charge collection efficiency increases by the extra photovoltage from the embedded PV cell. In addition, the nSi/TiO_2 nanowire photoanode shows higher IPCE at shorter wavelength due to higher absorption coefficient, while the PV embedded npSi/TiO_2 photoanode shows maximum IPCE at λ=330 nm under - 0.65 V vs RHE. The IPCEs were enhanced by utilizing the extra positive bias potential from the embedded npSi PV cell as λ

changes from 310 nm to 330 nm, while they decrease at λ > 330 nm even with extra bias potential effects due to smaller absorption by TiO_2 shell near the bandgap illumination.

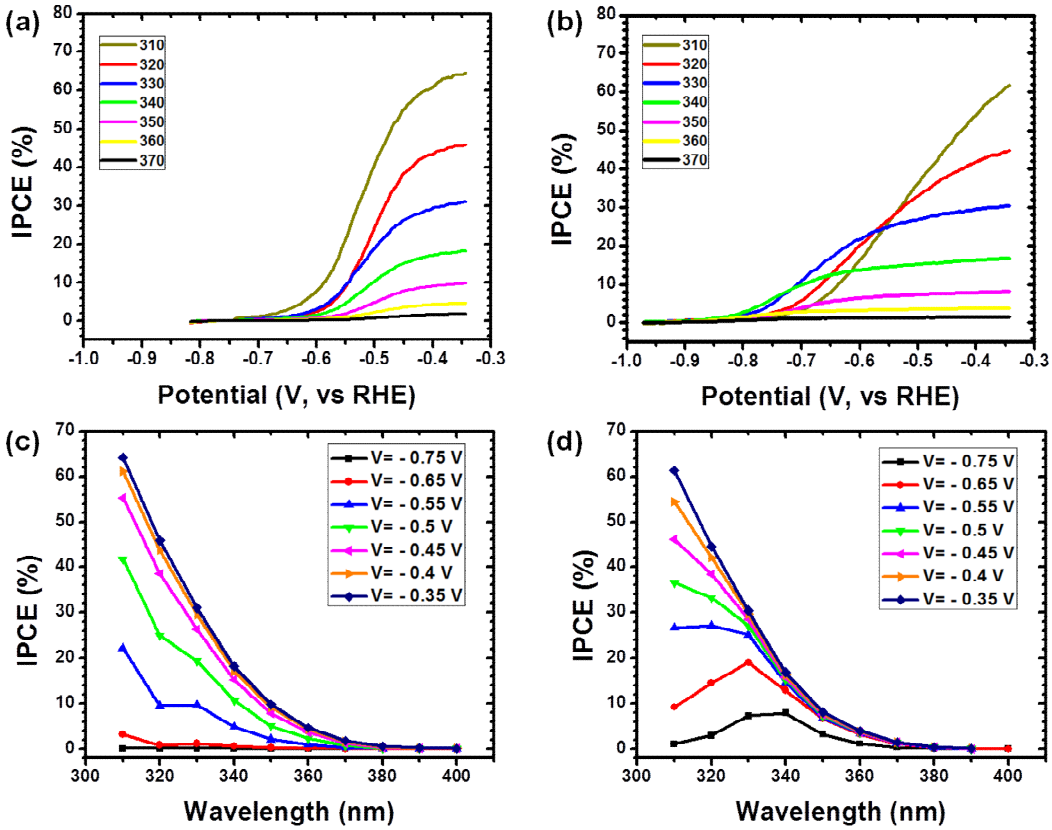

Figure 6.7. Plots of IPCE vs RHE (sweeping rate, 50 mV/s) with (a) nSi/TiO_2 nanowire photoanode, and (b) npSi/TiO_2 nanowire photoanode while the light source varied λ = 310 nm ~370 nm. Plots of IPCE vs wavelength of the incident light with (c) nSi/TiO_2 nanowire photoanode, and (d) npSi/TiO_2 nanowire photoanode under various biased potentials - 0.75 V to - 0.35 V (vs RHE).

6.3 Si Nanowire Arrays for Photocathode

6.3.1 Synthesis of Si Nanowire Arrays for Photocathode

Silicon has been studied a lot for hydrogen evolution, and recently Shannon *et al.* studied Si wire arrays as a photocathode to generate hydrogen on the silicon electrode.[25, 38] The authors demonstrated that the collection efficiency of Si wires can increase even with

short minority diffusion length which is advantageous compared to the bulk Si electrode for solar to hydrogen application.[1, 26]

We grew Si nanowire arrays by vapor-liquid-solid (VLS) mechanism with soft-lithographically [39] patterned Au catalyst. 200 nm of silicon oxide layer was deposited on p-Si(111) (3~6 ohmcm) wafer by plasma-enhanced chemical vapor deposition (PECVD), and 7% poly(methyl methacrylate) (PMMA) in toluene was spin-coated and annealed at 85°C. Then, the sample was patterned with a Si mask [39] of 500 nm diameter holes with 1.5 μm periodicity. After 10 nm Cr was evaporated by e-beam at a tilted angle (65 ^{o}) as a mask, O_2 plasma and CHF_3/CF_4 plasma was sequentially introduced to etch exposed PMMA and oxide layers. After the patterned substrate was clean by buffered HF, 100 nm of Au film was deposited by e-beam evaporator, and then, PMMA layer was lift-off in acetone. The patterned Au film was transferred to VLS furnace to grow Si nanowire arrays vertically from the substrate with $SiCl_4$ (Sigma Aldrich, 99.99%) and 10 % of H_2/Ar carrier gas [40] at 875 °C. To remove Au catalyst from tops and sidewalls of the nanowire arrays, nanowire arrays were first etched by an KI/I_2 gold etchant. After rinse with water, 30 nm oxide shell was formed by dry oxidation at 930 °C for 1hr under oxygen flow and removed by the buffered HF before second Au etching in an KI/I_2 solution.[41] After twice of the Au etching, we obtained nanowire arrays with ~400 nm in diameter and 15~20 μm in length, and the Si nanowire surfaces are clean and well faceted. The p-Si/TiO_2 core/shell nanowire arrays photocathode was prepared by depositing 15 nm of ALD TiO_2 layer on the pSi nanowire arrays.

Figure 6.8a shows the SEM image of the bare p-Si nanowire arrays after Au etching and removing oxide layer with BHF etching which shows facets at the sidewall. Figure 6.8b shows the p-Si/TiO_2 core/shell nanowire arrays prepared by 15~20 nm of ALD of TiO_2 on the bare Si nanowire to increase stability of the electrode. To reduce the overpotential for HER, Pt was deposited on either bare Si or Si/TiO_2 core/shell nanowire photocathode. (Figure 6.8c-d)

Pt was deposited on the bare Si nanowire surface in 4mM of H_2PtCl_6 and 0.5 M of Na_2SO_4 with a Pt counter electrode under illumination and 0 V vs an Ag/AgCl reference electrode was applied for 15 sec to reduce Pt^{4+}. The photo-assisted electro-plating was reported to give more uniform Pt particles on the nanowire surface since the photo excited electrons on the Si surface can provide more nucleation center.[42] Tilted SEM images shows that Pt nanoparticles are deposited preferentially at the edge of sidewall. It can be firstly, because higher surface energy at the edge of the sidewall makes it more active for catalytic reduction of Pt^{4+} reduction, and secondly, because the edge of the sidewall feels more electric fields. One the other hand, 4mM of H_2PtCl_6 precursor in 10% MeOH aqueous solution was used for Pt deposition on Si/TiO_2 core/shell nanowires where MeOH was a hole scavenger.[43] Pt can be reduced on the TiO_2 surface without bias potential. Figure 4c and 4d shows the SEM images of the Si nanowire and Si/TiO_2 nanowire with 0.5 % Atomic of Pt decoration respectively, and the bright spots are corresponding to Pt particles, 5~50 nm.

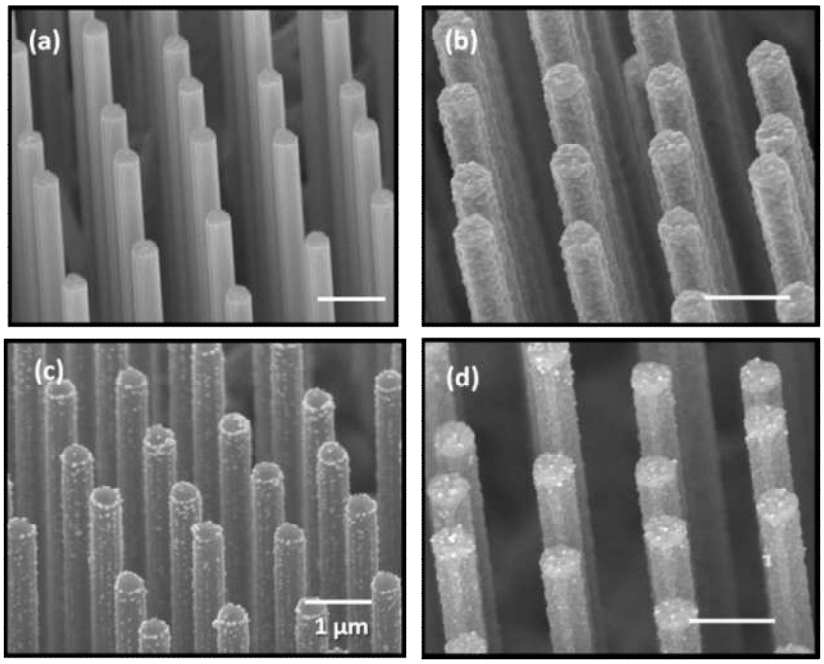

Figure 6.8. The tilted SEM images of (a) Si nanowire (pSi NW), (b) Si/TiO_2 nanowire (pSi/TiO_2 NW), (c) Si nanowire with Pt decoration (pSi/Pt NW), and (d) Si/TiO_2 nanowire with Pt decoration (pSi/TiO_2/Pt NW).

6.3.2 Photocathodic Properties of pSi and pSi/TiO_2 Nanowire

The PEC measurements with Si nanowire photocathodes were performed in 0.5M H_2SO_4. The bare Si nanowire arrays have no photocurrent at zero bias potential vs RHE (Figure 6.9a, black line) although the CBM of the silicon locates -0.5 V vs NHE which has high enough energy to reduce hydrogen.[44] However, Si nanowire with Pt decoration (pSi/Pt NW) shows -7.2 mA/cm^2 at 0 V vs RHE, and its onset potential of the photocurrents shifts by 600 mV (0.4 V vs RHE) because Pt cocatalysts can reduce the overpotential for HER and help the charge separation at the interface.[25] Figure 6.9a also shows that the TiO_2 ALD layer shifts the onset potential of the photocurrents to 0.2 V vs RHE and the saturated photocurrent increases by 10% compared to the bare Si nanowire photocathode which is associated that IPCE of the Si/TiO_2 core/shell nanowire increases especially 500 nm ~ 800 nm. (Figure 6.9b) Under illumination, the photoexcited electron in Si can transfer to TiO_2 since the CBM of TiO_2 (- 0.2 V vs RHE) is lower than that of Si, which increases the charge separation in core/shell nanowire and thus increases the catalytic activities. The photoacthodic properties with Pt decoration on p-Si/TiO_2 NW show the same onset potential with p-Si/Pt NW but higher photocurrent at the 0 V vs RHE.

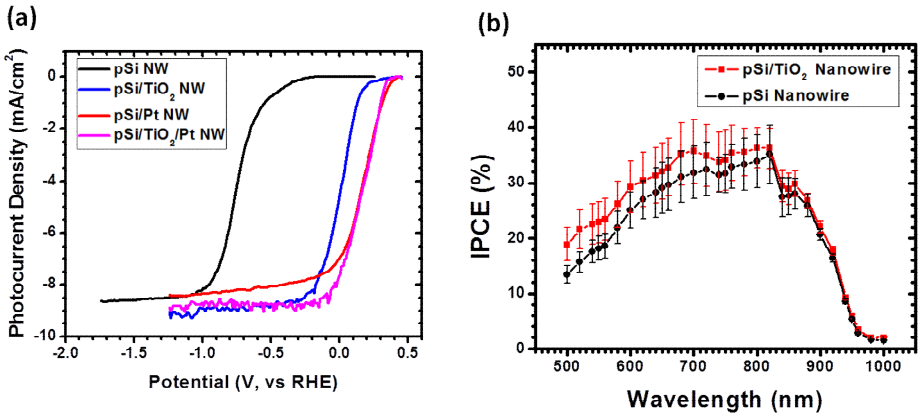

Figure 6.9. (a) Photocathodic current densities of pSi NW (black), pSi/TiO_2 NW (blue), pSi/Pt NW (red), and pSi/TiO_2/Pt NW (pink) in 0.5 M H_2SO_4. (b) IPCE of pSi NW (at -1.0 V vs RHE), and pSi/TiO_2 NW (-0.5 V vs RHE) with error bars.

6.3.3 Stability of pSi/TiO_2 Nanowire Photocathode

In addition, the stability of the Si can be enhanced with TiO_2 ALD coating. Paracchino *et al.* reported that Al doped zinc oxide and TiO_2 ALD layer could protect the unstable p-Cu_2O surface from decomposition even in mild pH.[4] Stability of silicon can be a problem for PEC application in various pH ranges due to oxidation by holes although p-type silicon is expected to be more stable cathodically under illumination in acidic condition. The downward band bending of p-Si at the interface with electrolyte causes accumulation of photogenerated electrons, while photogenerated holes move away[1] decreasing the oxidation of silicon. However, in dark, thin native oxide can be formed on Si surface in an aqueous electrolyte. We easily observed the I-V curve shifts toward more negative potential after Si surface exposed to water in dark. In a practical point of view, the electrode needs to preserve the catalytic activity during day and night. Moreover, most the PEC experiments with silicon have been done in acidic condition due to its fast etching in strong basic condition such as 1M KOH.[45] Our final goal is linking a photocathode and a photoanode in the same electrolyte for the overall water splitting. Otherwise, the chemical potential builds up over the time due to the change of the pH. Some of the photoanode materials such as Fe_2O_3 [46-47] or cocatalysts materials such as Co_3O_4 [48] prefer basic solution due to low activity and decomposition in acidic solution. Therefore, we want to develop stable Si photocathode over wide pH windows for the more practical application of the p-n PEC device. The p-n PEC activity with Si/TiO_2 NW photocathode and a photoanode in 1M KOH will be shown below while the bare Si NW was etched at the same condition. Thin coating of ALD TiO_2 over Si is advantageous for the protecting layer in several reasons. In terms of material wise, TiO_2 is one of the most stable semiconductors for PEC application in various pH solutions, and its lower CBM can provide a facile pathway for photoexcited

electrons to transport from core Si to electrolyte through TiO_2 layer. In a technique wise, ALD can deposit thin and conformal TiO_2 shell as a layer-by-layer through alternative chemical reactions even on pores of the materials. SEM and TEM images showed that less than 20 nm of TiO_2 layer could completely cover the core Si nanowire. (Figure 6.10)

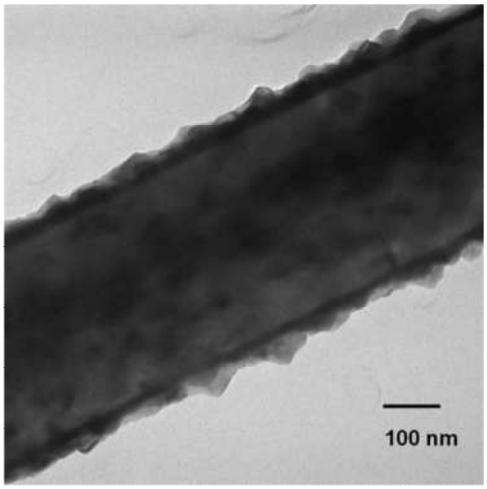

Figure 6.10. TEM image of p-Si nanowire with 15 nm TiO_2 ALD shell (p-Si/TiO_2 NW) showing conformal coating to protect the core Si from decomposition. TEM image was taken after PEC measurement in 1M KOH.

6.4 Linked photocathode and photoanode photoelectrochemical cell (p-n PEC Cell)

6.4.1 Operating photocurrent of a p-n PEC Cell

The above mentioned photocathode and photoanode electrodes are linked to measure I_{op} at zero bias potential under the simulated sunlight. Figure 6.11 shows the embedded PV cell in the photoanode electrode plays an important role to increase the overlap of the I-V curves with photocathode. Especially, when the surface of Si nanowire was modified either by Pt or ALD TiO_2, the overlap with the np Si/TiO_2 nanowire photoanode happens at the plateau of the photoanodic currents where I_{op} is determined mainly by the photoanodic activity of the TiO_2 not by the recombination rate between majority carriers. Table 6.1 shows the measured I_{op} at zero bias potential between the photocathode and the photoanode, and it is well matched with the expected I_{op} from the intersection between the I-V curves shown in Figure 6.11. I_{op} from the bare p-Si nanowire electrode linked with the n-Si/TiO_2 nanowire electrode shows less than 3 uA, which is much smaller than the maximum photocurrent either from the photocathode or the photoanode. In this case, I_{op} is limited by the small overlap between two I-V curves. This small I_{op} and positive V_{oc} (+ 0.36 V) indicates that self-driven water splitting is possible

with Si photocathode and nSi/TiO_2 core/shell photoanode combination but the efficiency is less than 0.005 %. However, STH conversion efficiency could be enhanced by 7 times with the platinized Si nanowire electrode and enhanced by another 3 times with the embedded PV cell in the npSi/TiO_2 nanowire photoanode. The embedded Si PV cell moves the potential of the band energy for the facile recombination between majority carriers so that I_{op} increases significantly in the p-n PEC configuration.

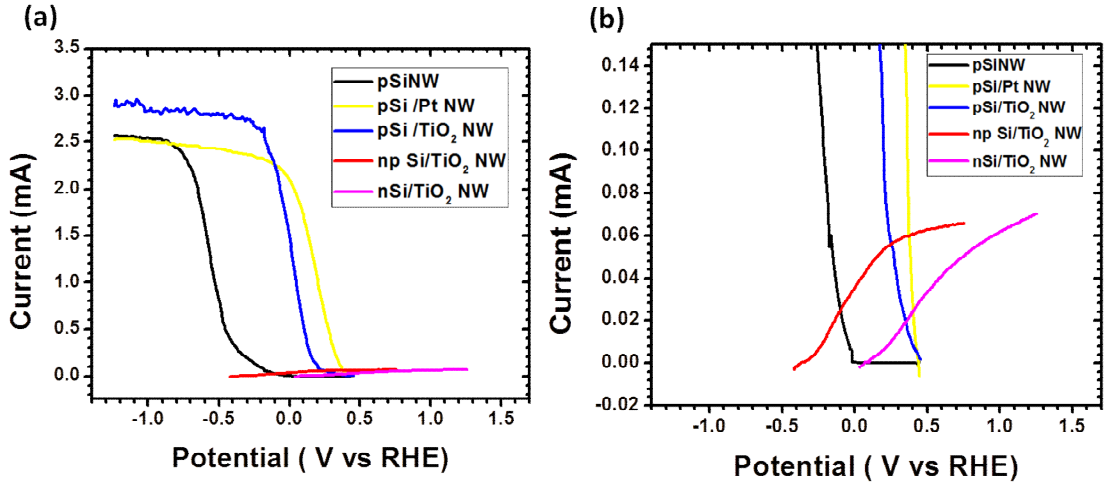

Figure 6.11. (a) Photocurrents of photocathodes and photoanodes in 0.5 M H_2SO_4 under 100 mW/cm^2 illumination with AM 1.5 filter and (b) its enlarged image.

0.5M H_2SO_4 (unit: uA)	pSiNW	pSi/TiO_2 NW	pSi/Pt NW
nSi/TiO_2 NW	< 3	16	22
npSi/TiO_2 NW	21	53	60

Table 6.1. The operating photocurrents of p-n PEC cells at zero bias potential with the various combinations of photocathode and photoanode measured in 0.5 M H_2SO_4 under 100 mW/cm^2 illuminaiton.

6.4.2 p-n PEC cells in Acidic and Basic Solution

The I_{op} of the p-n PEC cell was also monitored under the 300 W Xe lamp illumination without AM 1.5 filter (600 mW/cm^2). Figure 6.12a and b show the I-V photoresponses of photocathodes and photoanodes measured in 0.5 M H_2SO_4 and in 1M KOH, respectively, and Table 6.2 and 6.3 show the observed I_{op} in various combinations of the p-n PEC cell, and the expected I_{op} from the IV-curve overlap in parentheses. The measured I_{op} are well matched, more than 90% of the expected photocurrents. The I_{op} with the bare Si nanowire and the simple Si/TiO_2 nanowire core/shell electrode shows only 16 uA, but it is enhanced by 100 times with the best combination of photocathode and photoanode in sulfuric acid condition. Here, the I_{op} increases more due to higher light absorption of TiO_2 under high intensity of illumination. If we increase the photoanodic current by reducing the bandgap of n-type semiconductor, I_{op} will enhance further with the PV cell combination.

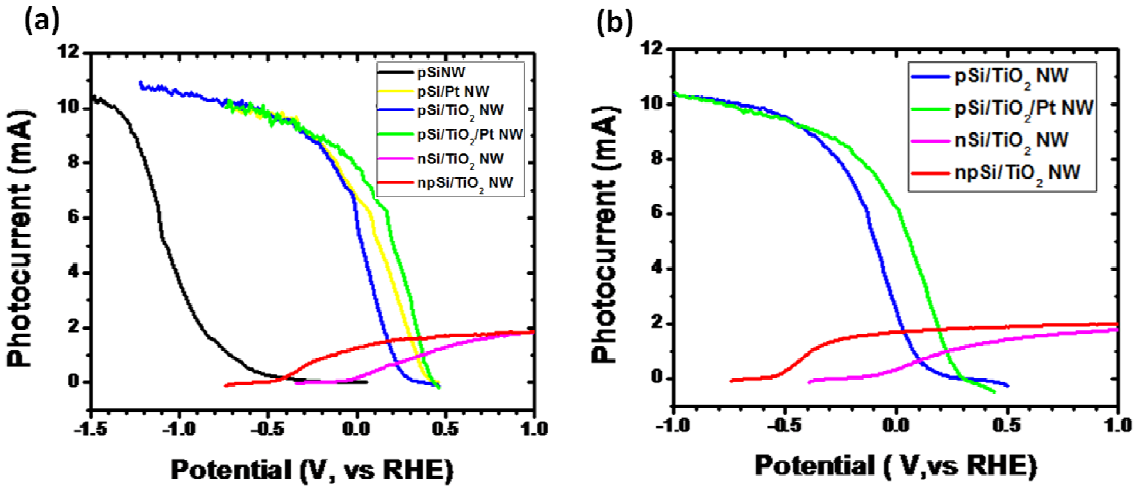

Figure 6.12. (a) Photocurrents of photocathodes and photoanodes (a) in 0.5 M H_2SO_4 and (b) 1M KOH under 300W Xe lamp illumination (600 mW/cm^2).

0.5M H_2SO_4 (unit: mA)	pSiNW	pSi/TiO_2 NW	pSi/ Pt NW	pSi/TiO_2 /Pt NW
nSi/TiO_2 NW	0.016 ±0.001 (0.02)	0.70 ± 0.02 (0.70)	0.86 ± 0.03 (0.94)	1.06 ± 0.03 (1.01)
npSi/TiO_2 NW	0.095 ± 0.008 (0.175)	1.35 ± 0.03 (1.5)	1.41 ± 0.04 (1.59)	1.60 ±0.03 (1.61)

Table 6.2. The operating photocurrents of p-n PEC cells at zero bias potential with the various combinations of a photocathode and a photoanode in 0.5 M H_2SO_4 with 300W Xe lamp illumination (600 mW/cm^2)

1M KOH (unit: mA)	pSi/TiO_2 NW	pSi/TiO_2 /Pt NW
nSi/TiO_2 NW	0.60 ±0.04 (0.680)	0.9 ±0.05 (0.996)
npSi/TiO_2 NW	1.75 ±0.03 (1.74)	1.85 ±0.06 (1.80)

Table 6.3. The operating photocurrents of p-n PEC cells at zero bias potential with the various combinations of a photocathode and a photoanode in 1 M KOH with 300W Xe lamp illumination (600 mW/cm^2).

Figure 6.13 shows that non-zero I_{op} was observed only under illumination and currents decrease to zero immediately in dark. It also demonstrates that the I_{op} under illumination was restored and stable even in 1M KOH since ALD TiO_2 coating can protect the Si photocathode. In addition, higher photocurrent was observed in 1M KOH compared to acidic electrolyte (0.5 M H_2SO_4) under the same condition due to the higher fill factor of TiO_2 photoanode which leads 0.54 % of STH efficiency.

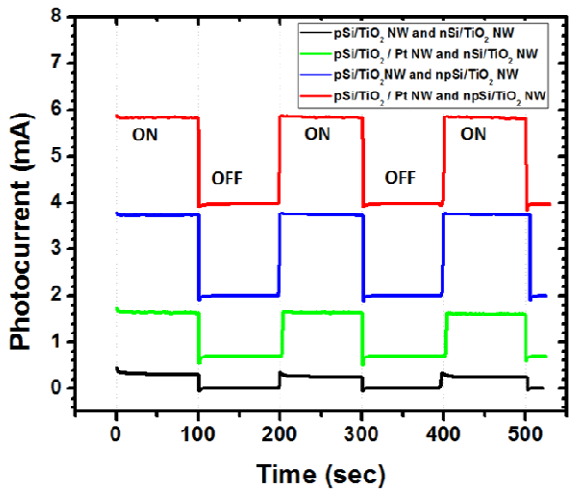

Figure 6.13. The operating photocurrents of linked cells with a photocathode and a photoanode (p-n PEC) without bias potential in 1M KOH while the illumination was on and off.

6.4.3 Gas Evolution Measurement with Self-Driven p-n PEC Water Splitting Cell

The generated hydrogen and oxygen gases from the p-n PEC cell were collected in a glassware with quartz window which was connected in a gas chromatography (Agilent Micro GC 3000). The evolved gases amounts were measured every 20 min up to 2 hr, and the pressure of the glassware was monitored to calculate the number of moles of evolved hydrogen and oxygen. The operating photocurrent was recorded during gas collection with a chronoamperometry measurement of potentiostat to calculate Faradic efficiency. We confirmed that the evolved hydrogen to oxygen gas amounts were close to 2:1 ratio (2.33$\pm$ 0.08 : 1) with gas chromatography, and their Faradic efficiencies were 91.6 $\pm$2.4 %. (Figure 6.14)

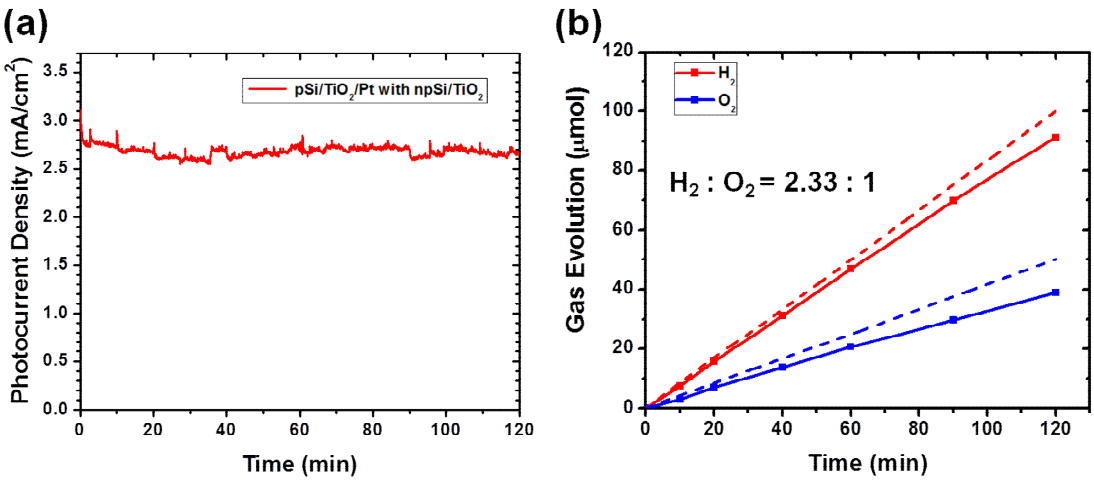

Figure 6.14. (a) Chronoamperometry measurement of the operating photocurrent with pSi/TiO_2/Pt nanowire photocathode and npSi/TiO_2 nanowire photoanode with 450 W Xe lamp. (b) The amount of hydrogen and oxygen evolution during illumination. The generated gas was measured with gas chromatography (solid line) and calculated (broken line) from the photocurrent flow in (a).

6.5 Conclusion

This chapter demonstrates that self-driven water splitting with p-n PEC cells, which consists of Si and TiO_2 nanowires, can be realized under illumination. To increase the operating photocurrent with the p-n PEC cell, Si PV cell is embedded under n-TiO_2 photoanode. Experimentally, we shows that the I-V curves of n-TiO_2 photoanode shifted by cathodically (n-Si/p-Si PV cell) or anodically (p-Si/n-Si PV cell) depending on the polarity of the embedded Si PV cell, and n-Si/p-Si PV cell increases the photoanodic activity of TiO_2 shell for water oxidation. n-Si/n-TiO_2 nanowire and npSi/n-TiO_2 nanowire

photoanodes were linked with p-Si nanowire photocathodes which were decorated with Pt or TiO_2 ALD thin film to increase the hydrogen reducing activity and stability during PEC reaction. Especially, Si photocathode coated by thin film ALD TiO_2 shows stable operating photocurrents even in 1M KOH solution. We observed that the real operating photocurrent of the p-n PEC cell can be estimated with more than 90% accuracy from the intersection point of the I-V curves for each n- and p-type semiconductor.

By utilizing the photovoltage generated by the embedded n-Si/-Si PV cell in the photoanode, the overlap of I-V curves with Si photocathode was enhanced leading higher STH conversion efficiency (0.54 %) in the p-n PEC cell. These p-n PEC devices show close to 2:1 ratio of hydrogen to oxygen evolution with 92 % of Faradic efficiency, and they can split water without extra bias potential under illumination. We suggest that STH conversion efficiency with a p-n PEC cell can be improved further by replacing TiO_2 to visible light absorbing n-type semiconductor. In addition, when we search the semiconductor candidates, the onset potential of the photocurrent and fill factors are important factor to increase the operating current of the p-n PEC cell, and a combination with the PV cell can be considered to shift the onset potential of the photocurrent for higher efficiency.

References

[1] Walter, M. G.; Warren, E. L.; Mckone, J. R.; Boettcher, S.W.; Santori, E. A.; Lewis, N. S. *Chem. Rev.* **2010,** *110*, 6446–6473.

[2] Maeda, K.; Domen, K. *Phy. Chem. Lett.* **2010,** *1*, 2655-2661.

[3] Lin, Y.; Yuan, G.; Liu, R.; Zhou, S.; Sheehan, S. W.; Wang, D. *Chem. Phys. Lett.* **2011**, 507, 209-215.

[4] Paracchino, A.; Laporte, V.; Sivula, K.; Grätzel, M.; Thimsen, E. *Nat. Mater.* **2011**, 10, 456-461.

[5] Hou, Y.; Abrams, B. L.; Vesborg, P. C.; Björketun, M. E.; Herbst, K.; Bech, L.; Setti, A. M.; Damsgaard, C. D.; Pedersen, T.; Hansen, O.; Rossmeisl, J. ; Dahl, S.; Nørskov, J. K.; Chorkendorff, I. *Nat. Mater.* **2011**, 10, 434-438.

[6] Bolton, J. R.; Strickler, S. J.; Connolly, J. S., *Nature* **1985**, *316*, 495-500.

[7] Bak, T.; Nowotny, J.; Rekas, M.; Sorrell, C. C. *Int. J. Hydrogen Energy* **2002**, *27*, 991-1022.

[8] Fukishima, A.; Honda, K. *Nature* **1972**, 238, 37-38.

[9] Gerischer, H. *Solar Energy Conversion*, Springer Berlin: Heidelberg, **1979**, p115-172.

[10] Cooper, G.; Turner, J. A.; Nozik, A. J. *J. Electrochem. Soc.* **1982**, 129, 1973-1977.

[11] Yoneyama, H.; Sakamoto, H.; Tamura, H. *Electrochimica. Acta.* **1975,** *20,* 341-345.

[12] Nozik, A. J. *Appl. Phys. Lett.* **1976,** *29,* 150-153.

[13] Ohashi, K.; Mccann, J.; Bockris, J. O'M. *Nature* **1977**, 266, 610-611.

[14] Nozik, A. J. *Appl. Phys. Lett.* **1977,** *30,* 567-569.

[15] Fornarini, L.; Nozik, A. J.; Parkinson, B. A. *J. Phys. Chem.* **1984,** *88,* 3238-3243.

[16] Mettee, H.; Otvos, J. W.; Calvin, M. *Solar Energy Mater.* **1981,** *4,* 443-453.

[17] Kainthla, R. C.; Khan, S. U. M.; Bockris, J. O'M. *Int. J. Hydrogen Energy* **1987,** *12,* 381-392.

[18] Kainthla, R. C.; Khan, S. U. M.; Bockris, J. O'M. *J. Electrochem. Soc.* **1987,** *134,* 841-845.

[19] Akikusa, J.; Khan, S. U. M. *Int. J. Hydrogen Energy* **2002,** *27,* 863-870.

[20] Wang, H.; Deutsch, T.; Turner, J. A. *J. Electrochem. Soc.* **2008,** *155,* F91-F96.

[21] Weber, M. F.; Dignam, M. J.; *J. Electrochem. Soc.,* **1984,** *131,* 1258–1265.

[22] Weber, M. F.; Dignam, M. J.; *Int. J. Hydrogen Energy,* **1986,** *11,* 225-232.

[23] Nakato, Y.; Yano, H.; Nishiura, S.; Ueda, T.; Tsubomura, H. *J. Electroanal. Chem.* **1987,** *228,* 97-108.

[24] Maier, C. U.; Specht, M.; Bilger, G. *Int. J. Hydrogen Energy* **1996,** *21,* 859-864.

[25] Boettcher, S. W.; Warren, E. L.; Putnam, M. C.; Santori, E. A.; Turner-Evans, D.; Kelzenberg, M. D.; Walter, M. G.; McKone, J. R.; Brunschwig, B. S.; Atwater, H. A.; Lewis, N. S. *J. Am. Chem. Soc*. **2011**, *133,* 1216-1219.

[26] Boettcher, S. W.; Spurgeon J.; Putnam, M. C.; Warren, E. L.; Turner-Evans, D. B.; Kelzenberg, M. D.; Maiolo, J. R.; Atwater, H. A.; Lewis, N. S. *Science* **2010,** *327,* 185-187.

[27] Morisaki, H.; Watanabe, T.; Iwase, M.; Yazawa, K. *Appl. Phys. Lett.* **1976,** *29,* 338-340.

[28] Khaselev, O.; Turner, J. A. *Science* **1998,** *280,* 425-427.

[29] Khaselev, O.; Bansal, A.; Turner, J. A. *Int. J. Hydrogen Energy* **2001,** *26,* 127-132.

[30] Miller, E.; Paluselli, D.; Marsen, B.; Rocheleau, R. *Solar Energy Mater. Solar Cells* **2005,** *88,* 131-144.

[31] Brillet, J.; Cornuz, M.; Formal, F.; Yum, J.; Gratzel, M.; Sivula, K. *J. Mater. Res.* **2010,** *25,* 17-24.

[32] Garnett, E.; Yang, P. *Nano. Lett.* **2010**, *10, 1082-1087.*

[33] Hwang, Y. J.; Boukai, A.; Yang, P. *Nano. Lett.,* **2009**, *9* , 410-415.

[34] Boukai, A.; Haney, P. ; Katzenmeyer, A.; Gallatin,G. M.; Talin, A. A.; Yang, P. *Chem. Phys. Lett.* **2011**, *501*, 153-158.

[35] Peng, K.Q.; Lee. S. T. *Adv. Mater.* **2011**, *23*, 198-215.

[36] Aarik, J.; Aidla, A.; Kiisler, A. A.; Uustare, T.; Sammelselg, V. *Thin Solid Films* **1997,** *305*, 270-273.

[37] Reichman, J. *Appl. Phys. Lett.* **1981,** *38*, 251-253.

[38] Maiolo III, J. R.; Kayes, B. M.; Filler M. A.; Putnam, M. C.; Kelzenberg, D. K.; Atwater, H. A.; Lewis, N. S. *J. Am. Chem. Soc.* **2007,** *129*, 12346-12347.

[39] Choi, S.J.; Yoo, P. J.; Baek, S. J.; Kim, T. W.; Lee, H. H. *J. Am. Chem. Soc.* **2004**, *126*, 7744-7745.

[40] Hochbaum, A. I.; He, R.; Fan, R.; Yang, P. *Nano. Lett.* **2005**, *5*, 457-460.

[41] Kendrick, C. E.; Yoon, H. P.; Yuwen, Y. A.; Barber, G. D.; Shen, H.; Mallouk, T. E.; Dickey, E. C.; Mayer, T. S.; Redwing, J. M. *Appl. Phys. Lett.* **2010,** *97*, 143108.

[42] Kawamura, Y. L.; Sakka, T.; Ogata, Y. H. *J. Electrochem. Soc.* **2005,** *152*, C701-C705.

[43] Harada, M.; Einaga, H. *Catalysis Communications.* **2004,** *5*, 63-67.

[44] Dominey, R. N.; Lewis, N. S.; Bruce, J. A.; Bookbinder, D. C.; Wrighton, M. S. *J. Am. Chem. Soc.* **1982,** *104*, 467-482.

[45] Seide, H.; Csepregi, L.; Heuberger, A.; BaumgSrtel, H. *J. Electrochem. Soc.* **1990,** *137*, 3612-3632.

[46] Ohmori, F.; Takahashi, H.; Mametsuka, H.; Suzuki, E. *Phys. Chem. Chem. Phys.* **2000,** *2*, 3519-3522.

[47] Kennedy, J. H.; Anderman, M. *J.Electrochem. Soc.* **1983,** *130*, 848-852.

[48] Da Silva, L. M.; Boodts, J. F. C.; De Faria, L. A. *Electrochemica Acta* **2001,** *46*, 1369-1375, and reference therein.

[49] Kendrick, C. E.; Yoon, H. P.; Yuwen, Y. A.; Barber, G. D.; Shen, H.; Mallouk, T. E.; Dickey, E. C.; Mayer, T. S.; Redwing, J. M. *Appl. Phys. Lett.* **2010,** *97*, 143108.

Chapter 7

Summary and Perspective

1D nanostructured materials have been demonstrated for novel photonic properties, biological applications, and energy applications including energy storages (battery), thermoelectric devices, photovoltaic devices, and photoelectrochemical (PEC) devices since their unique physical and chemical properties can provide advantages over bulk materials. Recently, photocatalytic semiconductor nanowires have been investigated for photoelectrodes in a PEC water splitting cell for clean hydrogen production due to their high surface areas and charge transport properties. However, more studies are required to understand material properties and to realize nanowire PEC cells with high performance.

The first part of this dissertation investigates PEC water splitting properties with a TiO_2 nanowire arrays photoanode by varying their length and surface properties. Due to low electron transport of rutile TiO_2, the IPCE of nanowire arrays decreases at shorter wavelengths for longer nanowires while it increases linearly vs the absorption of photon $(1-10^{-\alpha \times Length})$ particularly with near bandgap illumination. Because of these two opposite effects of the nanowire length, the photocurrent of TiO_2 nanowire photoanode approaches saturation with a length of 1.8 μm. The charge collection efficiency of the TiO_2 nanowire arrays can be enhanced with epitaxial ALD layer coating possibly due to passivation of surface states and an increase of surface area resulting higher IPCE values at short wavelengths (UV regions), and a photocurrent enhancement of 1.5 times. This study shows

that the charge collection is the process that limits the efficiency of the long nanowires, and the geometric and surface properties of nanowires have to be considered to increase the charge collection efficiency, and consequently the STH efficiency. The research strategies that are taken here can be applicable for other photocatalytic semiconductor materials. Comparing IPCE and optical measurements can provide a research direction whether we want to focus on improving charge collection processes or light absorption processes to achieve high STH efficiency.

Next, a dual bandgap configuration is demonstrated with two well-studied semiconductor materials, Si and TiO_2, for solar water splitting. By coating stable TiO_2 on the shell of Si surface, the TiO_2 layer can protect the core Si from photodecomposition leading an excellent stability of the Si/TiO_2 dual bandgap system. In the aspect of geometry, the highly dense Si EENW / TiO_2 photoanode has 2.5 times higher photocurrent density than the planar Si/TiO_2 photoanode due to lower reflectance and higher surface area. Even with the same nanowire arrays, the n-Si/n-TiO_2 nanowire arrays exhibits a larger photocurrent and open circuit voltage than p-Si/n-TiO_2 nanowire arrays since a schottky barrier at the n/n heterojunction helps the charge separation and minimize recombination within TiO_2 shell compared to the p/n heteorjunction for the photoanode application. These results show the bend banding at the interface between two semiconductors plays an important role to separate photogenerated charges.

Then, we design asymmetric Si/TiO_2 nanowires to enhance the charge separation for overall water splitting within a single nanowire. Hydrogen evolution reaction is expected to occur on the Si surface as a photocathode, while oxygen evolution reaction on the TiO_2 surface as a photoanode, the other side of the asymmetric nanowire. The light induced charge separation is monitored within a single asymmetric nanowire with KPFM by measuring the local surface potentials. The more positive surface potential on the n-TiO_2 side compared to the p-Si side indicates minority carriers of semiconductors (holes in n-TiO_2 and electrons in p-Si) are separated while majority carriers (electrons in n-TiO_2 and holes in p-Si) of semiconductors are recombined at the interface. This spatially resolved KPFM measurement shows that it is possible to observe charge separation within the single asymmetric nanowire, and the direction of the charge separation is expectable from the recombination between majority carriers. Due to the charge separation, asymmetric Si/TiO_2 nanowires increase hydrogen evolution rates compared to Si/TiO_2 core/shell nanowires. Furthermore, the overall STH efficiency with the asymmetric nanostructures can be potentially improved more by using two visible light absorbers whose carrier generation rates are matched under solar irradiation.

Three-dimensional (3D) hierarchical nanostructures are synthesized by the halide chemical vapor deposition (HCVD) of InGaN nanowires on Si wire arrays as an advanced nanostructure to increase the surface area and optical absorption. An enhancement of 5 times in photocurrent is observed for water oxidation when the surface area increases from simple InGaN nanowires on planar Si to 3D hierarchical InGaN nanowires on Si wires. Si/InGaN hierarchical nanowire arrays are stable without photodecomposition for the water oxidative photoanode applications which demonstrates the potential usages of InGaN alloy for solar water splitting application. This study also shows that 3D hierarchical nanostructures are viable high surface area geometries for PEC application. However, future works are required to use InGaN for water splitting since its quantum efficiency is still too low to have high STH efficiency. Several strategies can be examined to improve the performance of InGaN nanowire alloy. Similarly to TiO_2 nanowire, we can passivate the surface defect sites with thin layer of ALD. Modification of surface with oxidative co-catalysts such as RuO_2, IrO_2, and Co_3O_4 can be investigated to increase the photoanodic activity for water oxidation with oxide or oxynitride semiconductors. Controlling doping carrier concentration on InGaN nanowires is one of the methods to improve electrical properties such as mobility, minority carrier diffusion length, lifetime of minority carrier, and surface states which affect the charge transport and the interfacial charge transfer at semiconductor/electrolyte junction. Lastly, incorporation more indium into InGaN nanowires is required to decrease the bandgap of InGaN to 1.8~2.0 eV while keeping high water splitting performances.

The rest of this dissertation demonstrates the self-driven water splitting devices by combining a photocathode and a photoanode in the same electrolyte under illumination. n-Si/p-Si PV cell is embedded under n-TiO_2 nanowire photoanode to shift the photoanodic I-V curve toward more negative potential compared to n-Si/n-TiO_2 nanowire photoanode which increases the operating photocurrent when it linked with a p-Si nanowire photocathode. This design shows that an extra bias potential from photovoltaic cell can be provided to the shell TiO_2 when a smaller bandgap Si photovoltaic cell is embedded under a large bandgap TiO_2 which is applicable for the other semiconductors. This biasing effect induced by the jointed PV cell is more useful when the bandedges of the semiconductor do not fit the requirement of bandedge potential for water splitting. The operating photocurrent of the p-n PEC cell increases and stays stable in wide window of pH solution when p-Si nanowire surface is coated by 15 nm of ALD TiO_2 thin film since TiO_2 thin film can enhance the fill factor and PEC stability. The ALD protection layer can open up the

opportunities to use the existing unstable semiconductors, and to link them for the p-n PEC cell in various pH electrolytes in a stable fashion. These self-driven p-n PEC devices show close to 2:1 ratio of hydrogen to oxygen evolution with 92 % of Faradic efficiency. We suggest that STH conversion efficiency with a p-n PEC cell can be improved further by replacing TiO_2 to visible-light absorbing n-type semiconductor such as InGaN assuming we can improve its internal quantum efficiency. Also, when we search the semiconductor candidates for self-driven water splitting, a fill factor and an onset potential of the photocurrent are important factors to increase the operating current of the p-n PEC cell, and a combination with PV cell can be considered to achieve high STH efficiency. While these studies with model semiconductor systems such as TiO_2 and Si cannot accomplish benchmarking 10% STH efficiency, they can provide an idea to enable progress towards advanced 1D nanostructure incorporation into reliable and high-performance devices.

Appendix A

Publication List

[1] **Hwang, Y. J.**; Jeong, H. E.; Garnett, E.; Yang, P. "Design of Efficient Self-Driven Solar to Water Splitting Device: Si Nanowire Photocathode Linked with Si Photovoltage Cell Embedded TiO_2 Photoanode" *(in preparation)*

[2] Tüysüz, H.; **Hwang, Y. J.**; Yang, P. "Nanocast Co_3O_4 as a highly active anode material for the electrochemical water splitting" *(in preparation*)

[3] **Hwang, Y. J.**; Hahn, C.; Liu, B.; Yang, P. "Photoelectrochemical Water Splitting Dependence on the Length and ALD Coating with TiO_2 Nanowire Arrays" *(accepted in ACS Nano)*

[4] **Hwang, Y. J.**; Wu, C.; Hahn, C.; Jeong, H. E.; Yang, P. "Si/InGaN Core/Shell Hierarchical Nanowire Arrays for Solar Water Splitting" *Nano. Lett.* **2012**, *12*, 1678-1682. **(Research Highlights at nanotechweb.org, Mar 16, 2012)**

[5] Liu, C.; **Hwang, Y. J.; (co-first authorship)** Jeong, H. E.; Yang, P. "Light-Induced Charge Transport within a Single Asymmetric Nanowire" *Nano. Lett.* **2011**, *11*, 3755-3758.

[6] Hahn, C.; Zhang, Z.; Fu, A.; Wu, C. H.; **Hwang, Y. J.**; Gargas, D. J.; Yang, P. "Epitaxial Growth of InGaN Nanowire Arrays For Light Emitting Diode" *ACS Nano* **2011**, *5*, 3970-3976.

[7] Kim, D. H.; **Hwang, Y. J.**; Ryou, J.; Kim, S.; Hong, S. "Atomic and electronic structure of styrene on Ge (100)" *Surf. Sci.* **2011**, *605*, 1438-1444.

[8] **Hwang, Y. J.**; Boukai, A.; Yang, P. "High Density n-Si/n-TiO_2 Core/Shell Nanowire Arrays with Enhanced Photoactivity" *Nano. Lett.* **2009**, *9*, 410-415. **(Research Highlights in " *Nature Photonics* ", 2009, 3, 72-73)**

[9] **Hwang Y. J.**; Hwang, E.; Kim, D. H.; Kim, A.; Hong, S.; Kim, S. "Discrimination of Chiral Configurations : Styrene on Germanium(100)" *J. Phys. Chem. C.* **2009**, *113*, 1426-1432.

[10] Hochbaum, A. I.; Gargas, D.; **Hwang, Y. J.**; Yang, P. "Single Crystalline Mesoporous Silicon Nanowires" *Nano. Lett.* **2009**, *9*, 3550-3554.

[11] Hwang E.; Kim, D. H.; **Hwang, Y. J.**; Kim, A.; Hong, S.; Kim, S. "Bidentate structures of acetic acid on Ge(100): The role of carboxyloxygen" *J. Phys. Chem. C.* **2007**, *111*, 5941-5945.

[12] **Hwang Y. J.**; Kim, A.; Hwang, E.; Kim, S. "Chiral attachment of styrene mediated by surface dimers on Ge(100)" *J. Am. Chem. Soc.* **2005**, *127*, 5016-5017.